University of Alberta

MODELING AND CONTROL OF MAGNETICALLY-LEVITATED ROTATING SHAFTS WITH ACTIVE MAGNETIC BEARINGS AND SELF-BEARING MOTORS

by

Thomas R. Grochmal 

A thesis submitted to the Faculty of Graduate Studies and Research in partial fulfillment of the requirements for the degree of **Doctor of Philosophy**.

Department of Electrical and Computer Engineering

Edmonton, Alberta
Fall 2008

Your file Votre référence
ISBN: 978-0-494-46325-3
Our file Notre référence
ISBN: 978-0-494-46325-3

University of Alberta

Library Release Form

Name of Author: Thomas R. Grochmal

Title of Thesis: Modeling and Control of Magnetically-Levitated Rotating Shafts with Active Magnetic Bearings and Self-Bearing Motors

Degree: Doctor of Philosophy

Year this Degree Granted: 2008

_____

Thomas R. Grochmal

Date: _____

University of Alberta

Faculty of Graduate Studies and Research

The undersigned certify that they have read, and recommend to the Faculty of Graduate Studies and Research for acceptance, a thesis entitled **Modeling and Control of Magnetically-Levitated Rotating Shafts with Active Magnetic Bearings and Self-Bearing Motors** submitted by Thomas R. Grochmal in partial fulfillment of the requirements for the degree of **Doctor of Philosophy**.

_____

Dr. Alan Lynch (supervisor)

_____

Dr. Carl Knospe (external examiner)

_____

Dr. Amos Ben-Zvi

_____

Dr. Tongwen Chen

_____

Dr. Yunwei Li

_____

Dr. Horacio Marquez

Date: _____

Abstract

This thesis covers aspects of modeling, control, and design of magnetically-levitated rotating shafts. This topic is subdivided into two discrete but related problems.

In the first problem we consider trajectory tracking of a shaft that is levitated by active magnetic bearings (AMBs) and rotated by a conventional motor. Trajectory tracking involves control of the AMBs such that the rotating shaft follows a prescribed path with minimal vibration. Trajectory tracking and vibration minimization are addressed in a common control framework incorporating the ideas of differential flatness and nonlinear observers. Furthermore, the nonlinear and overactuated nature of AMBs are studied through a comparison of control approaches.

In the second problem we consider a shaft that is simultaneously levitated and rotated by a self-bearing motor (SBM). Whereas AMBs achieve levitation on the well-known basis of reluctance force, the type of SBM considered in this thesis, namely the toothless self-bearing servomotor (TSBS), creates levitation using the less common Lorentz force. The operating principle of the TSBS is studied and nonlinear expressions for levitation force and torque are derived from first principles. Insight from force and torque characterization leads to a more general dynamic model that introduces previously unused control variables. Based on our dynamic model a control system is designed which extends the physical operating range of the TSBS relative to the established control approach and resolves the conflict between the levitation and rotation subsystems in the presence of input saturation. Performance improvements are confirmed on an experimental TSBS. Finally, exploiting all control variables of the TSBS motivates redesign of the TSBS itself. A new operating principle, dynamic model, and control system are proposed and experimentally validated which reduces the device's power electronic requirements.

Keywords: magnetic levitation, active magnetic bearings, self-bearing motors, nonlinear control, nonlinear observers.

Acknowledgements

I acknowledge, above all, the grace of God and the love and support of my wife, Rachel, for seeing me through this endeavour.
I acknowledge my supervisor, Dr. Alan Lynch, for providing me with the opportunity to pursue graduate studies, for investing significant time and energy to train me, and for always holding my work to a high standard of quality.

The support of academic peers has been instrumental to the completion of my research program. I am grateful to Dr. Joachim Rudolph and his research team at the Institut für Regelungs- und Steuerungstheorie (Laboratory of Control Theory) at the Technical University of Dresden (TU-Dresden), Germany. Their research base provided a foundation for the work in this thesis. A special acknowledgement goes to TU-Dresden researcher Carsten Collon for his help with the magnetic bearing project and for his research insights over scotch. I am grateful to Dave Kastelan for his artwork contributions and to Ryan Chladny and Chris Forbrich for their collaboration on the experimental and computational aspects of the research.

To my remaining colleagues from the Applied Nonlinear Controls Lab (Martin, Cesar, Yebin, Ed, Karla, Kim and Rasoul), I say "thank you" for the lighter moments in the lab during the last five years.

Table of Contents

List of Tables

List of Figures

Chapter 1

Introduction

This thesis encompasses aspects of modeling, control, and design of electromagnetic actuators used to levitate rotating shafts. The electromagnetic actuators that we consider are active magnetic bearings (AMBs) and self-bearing motors (SBMs). Whereas the AMB provides levitation only, the SBM has an integrated drive so that it can levitate and rotate a shaft simultaneously. Since the functionality and physics of AMBs are a subset of that of the SBM, our initial study of AMBs in this thesis is an appropriate "warm up" to our latter study of the SBM. Both of these devices are discussed in greater detail in the next two sections.

Feedback control design is the chief focus in our study of AMBs and SBMs. The reason is that feedback controls have a significant impact on the performance and range of applications of these devices. The control designs in this thesis are model-based, and therefore we develop a detailed, physics-based model of each device. In the case of the SBM our modeling and control efforts lead us to develop a new operating principle. Therefore, in addition to feedback control we focus on modeling and design in this thesis.

1.1 Active magnetic bearings

A magnetic levitation system, to paraphrase the empirical definition stated in [10], provides a stable hovering state to a floating object, without any mechanical contact. An *active magnetic bearing* is a magnetic levitation system that derives its name from the fact that its function to provide contactless suspension to an object is similar to that of a bearing. In this sense all magnetic levitation systems can be regarded as AMBs. AMBs have attracted significant interest in academia and industry for almost 30 years because of their unique characteristics relative to conventional bearings and because they are a challenging application which spans the disciplines of electrical and mechanical engineering. AMBs

have been the subject of ten international symposia [1], two dedicated issues of academic journals [3],[4], and a textbook [111].

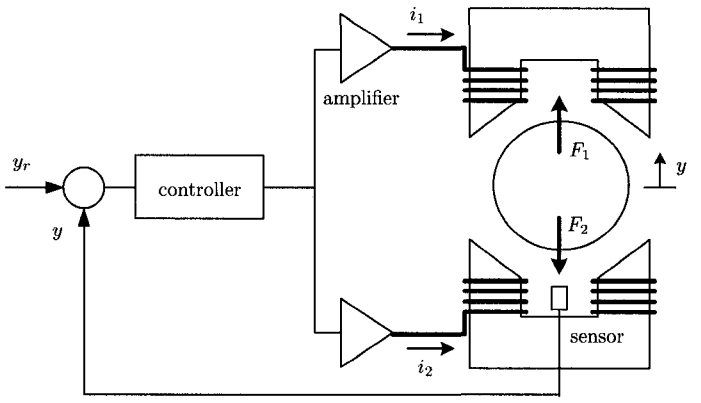

Figure 1.1: Traditional concept of a one degree-of-freedom active magnetic bearing system. F is the force generated on the ferromagnetic rotor by opposing electromagnets. The electromagnets are controlled by their coil currents i_1 and i_2. The coil currents are computed by a control law based on the desired rotor position y_r and feedback of the rotor position y.

The basic principle of the majority of AMB systems is explained by a simple one degree-of-freedom (1DOF) example as depicted in Figure 1.1. In this case a ferromagnetic object (typically, a rotor) is suspended between opposing horseshoe-shaped electromagnets. Each electromagnet can only generate an attractive force, denoted as F_1, F_2 in Figure 1.1. The electromagnets are controlled by their coil currents i_1 and i_2, which are generated by transconductance (or servo-) amplifiers. The coil currents are computed by a control law responding to feedback of the sensed position of the object, y, so as to bring it back to its reference y_r. The open-loop dynamics from i_1, i_2 to y are not stable in the bounded-input, bounded-output sense, and therefore feedback control is necessary.

The attractiveness of a ferromagnetic object to an electromagnet is explained by the Maxwell, or reluctance, force principle. The Maxwell force occurs when magnetic flux crosses the boundary between two media with differing magnetic permeability. Furthermore, the force is directed towards the medium having the lower permeability. Using the *principle of virtual work* we obtain an explicit calculation of the force F in terms of the rotor position y and the currents i_1, i_2. The force is computed from [111]

$$F = F_1 - F_2 = \frac{\Phi_1^2 - \Phi_2^2}{\mu_0 A_g}, \tag{1.1}$$

where μ_0 is the permeability of free space, A_g is the cross-sectional area of each pole piece, and Φ_1, Φ_2 are the magnetic fluxes flowing across the air gap of the upper and lower

magnetic loops, respectively. The magnetic loops are depicted in Figure 1.2. A good approximation to Φ_1, Φ_2 are obtained from magnetic circuit analysis in which we assume a uniform flux distribution across the surface of each pole piece. The fluxes are calculated as

$$\Phi_1 = \frac{Ni_1}{R_{g,1}}, \tag{1.2a}$$

$$\Phi_2 = \frac{Ni_2}{R_{g,2}}, \tag{1.2b}$$

where N is the number of winding turns for each pole piece and $R_{g,1}, R_{g,2}$ are the magnetic reluctances associated with the upper and lower air gaps, respectively. It is commonly assumed that the total reluctance of each circuit is dominated by the reluctance of the air gap since the magnetic permeability of air is three orders of magnitude less than that of iron. The reluctances $R_{g,1}, R_{g,2}$ are approximated as

$$R_{g,1}(y) = \frac{g_0 - y\cos\alpha}{\mu_0 A_p}, \tag{1.3a}$$

$$R_{g,2}(y) = \frac{g_0 + y\cos\alpha}{\mu_0 A_p}, \tag{1.3b}$$

where g_0 is the nominal air gap and α is the half-angle between the poles of the electromagnets as shown in Figure 1.2. Evaluating (1.1) from expressions (1.2)-(1.3) gives

$$F = \frac{\beta i_1^2}{(\kappa - y)^2} - \frac{\beta i_2^2}{(\kappa + y)^2}, \tag{1.4}$$

where $\beta = \mu_0 N^2 A_p / \cos\alpha$ and $\kappa = g_0 / \cos\alpha$. The force expression's quadratic dependence on coil currents and inverse quadratic dependence of rotor position are nonlinearities which explain the attractive-only nature of AMBs. Another interesting aspect of a 1DOF AMB system is that it is overactuated, i.e. there are more independently controlled forces than positional degrees of freedom, thus providing variability in how feedback control may be accomplished. These aspects of nonlinearity and overactuation are discussed in greater detail and generality in Chapters 2 and 3 for a 5DOF system.

The principle of a 1DOF AMB which was just described is the basis of operation for most AMB systems used in practice. Figure 1.3 shows typical configurations of radial and axial AMBs for the support of rotating machinery. Radial AMBs have 2DOF and consist of a stator and a journal which is mounted onto a rotating shaft. An axial AMB has 1DOF and consists of the stator and a disk mounted onto a shaft. Both of these types of AMBs are considered in this thesis.

From a technological perspective, the advantages of AMBs relative to conventional bearing systems are numerous. The greatest advantage is the elimination of mechanical

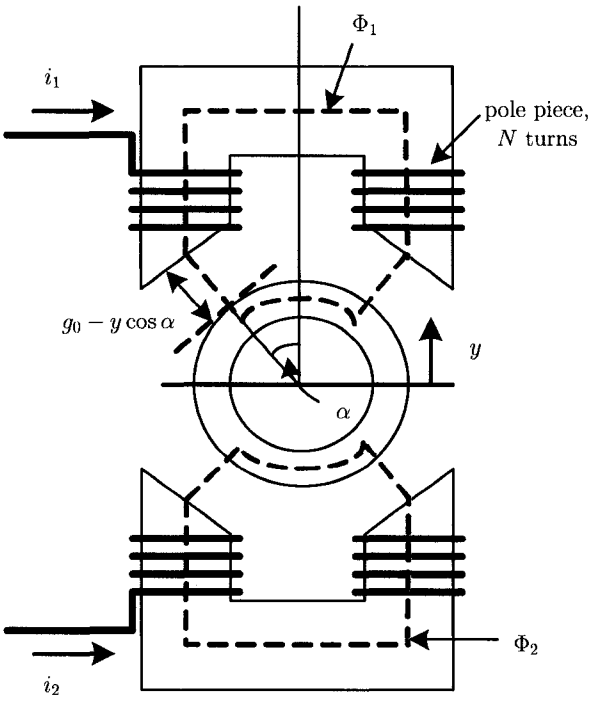

Figure 1.2: Idealization of a one degree-of-freedom active magnetic bearing for the purpose of magnetic circuit modeling. The dashed lines indicate the assumed flux paths.

friction; with this comes the elimination of material wear, particulate matter, and complex lubrication systems, the potential for higher precision positioning and higher rotational speeds, and the ability to tolerate harsher environment conditions. Active control is the next major advantage that AMBs have over their mechanical counterparts. This enables them to have variable stiffness and damping characteristics, permits vibration isolation of the rotor, and enhances system monitoring and diagnosis. AMBs also have some limitations. The specific force capacity, i.e. the ratio of the load carrying capability of a bearing to its volume, of an AMB is much lower than that of traditional bearings. Therefore AMBs are physically larger than other types of bearings for the same force capacity. Saturation of the iron of an AMB can lead to failure when its bearing capacity is exceeded, thus requiring a touchdown bearing system of the contact nature. And despite the benefits of active control, the need for sensors and electronics makes AMB installations costly.

Many situations where the advantages of AMBs significantly outweigh their disadvantages are well established and have proven their industrial feasibility [2]. Turbomolecular pumps [39], flywheel energy storage systems [5], turbo expanders, air-conditioning compressors, machining spindles [10], automated wafer-handling systems [86], and neutron

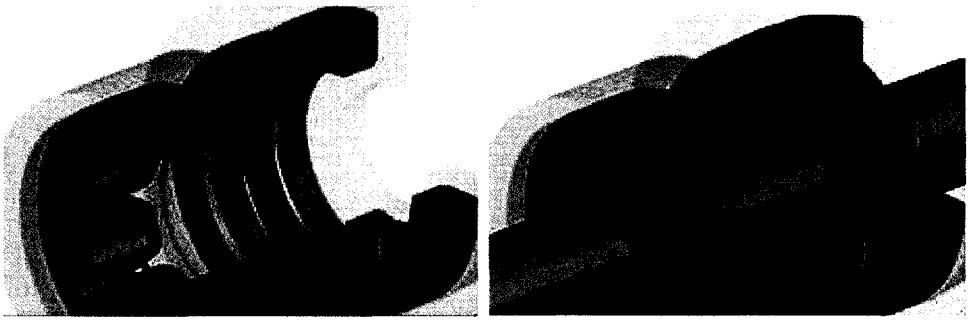

(a) without shaft and journals (b) with shaft and journals

Figure 1.3: Standard design of radial and axial active magnetic bearings. (S2M Magnetic Bearings, reproduced with permission.)

choppers [122] have all seen performance and/or productivity enhancements through the application of AMBs. The growing industry behind AMBs continues to motivate new directions of research. A great deal of this research has to do with feedback control. Although many applications of AMBs require only basic setpoint stabilization from the control system, the applicability of AMBs has increased as algorithms have become more advanced. For example, AMB-based flywheel energy storage systems require an optimal control policy which minimizes their energy consumption [5]. The application of AMBs to high-speed machining requires a model of the cutting process as a basis to suppress the onset of chatter [63]. Reactive power consumption by AMBs can be minimized through vibration control [8].

In this thesis, we consider a control problem motivated by the potential to perform non-circular boring with a magnetically-levitated spindle [83, 60, 131, 27]. The control problem is to track the path of the tool tip attached to the end of a rotating shaft. For instance, Figure 1.4 shows an automotive engine piston with a side port which was bored to be slightly elliptical so as to improve its structural properties. The control problem associated with this application is challenging in many respects. Maintaining a precise trajectory for a rotating shaft implies positioning it off the center point of the AMB and synchronizing the tool path to the speed of rotation. As a result, AMB nonlinearity becomes a potential concern in the control design. Control of vibration is also necessary to maintain the desired precision. These challenges give this particular problem an intrinsic interest from a control system viewpoint, and we address them in the next two chapters.

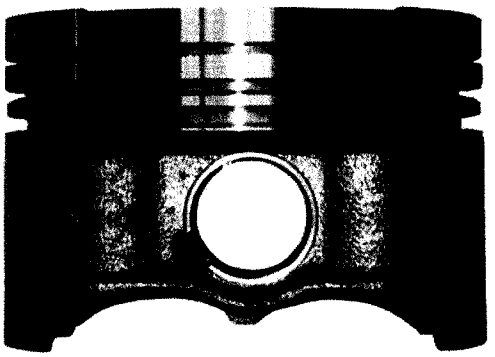

Figure 1.4: Aluminum automotive engine piston with a slightly elliptical port bored by a spindle supported by active magnetic bearings. (Reproduced with permission, S. Eckhardt, Technical University of Dresden, Germany.)

1.2 All-Lorentz self-bearing motors

Self-bearing motors (SBMs) are electric motors with the integrated function of an AMB. For this reason, SBMs are also termed *bearingless motors*. The term *self-bearing motor* is preferred for the reason that such motors are not technically bearingless, although they are in the traditional sense, but rather have a magnetically integrated bearing function. Widespread research on SBMs did not occur until the 1990s when, it is conjectured in [16], the high costs and performance limitations of digital control hardware and inverter electronics were overcome. Since the 1990s, SBMs have been extensively studied, with a survey by the end of that decade [107] reviewing over 90 articles on the subject. SBMs remain an active topic of research in the current decade, buoyed by an increase in potential industrial applications [97, 110, 93, 85]. Much of the research by 2005 was consolidated into a textbook [16].

Traditionally, magnetically-levitated rotating shafts have a separate motor which is borne by AMBs. SBMs serve to integrate both of these devices. This contrast in approaches is depicted in Figure 1.5. The primary appeal of SBMs is the possibility of developing more compact machines and thus reducing the shaft length. In principle, a decreased shaft length increases the resonant frequencies of the shaft, thus allowing for stable operation at higher speeds. In practice, this benefit has not yet been fully realized. Presently, SBMs can have an economic advantage as many configurations are driven by standard three-phase inverters. From an application perspective, the argument for SBMs has been particularly compelling in the domain of smaller motors where a cost advantage can be realized over a conventional motor combined with AMBs [109, 85].

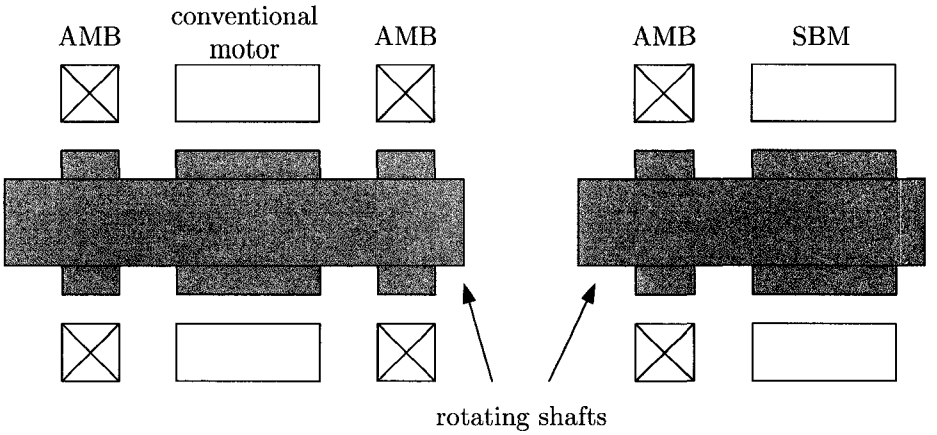

Figure 1.5: Different approaches to magnetically levitate a rotating shaft. On the left is the traditional approach using radial active magnetic bearings (AMBs) with a conventional electric motor. The approach shown on the right replaces an AMB and a conventional motor with a self-bearing motor (SBM). The desired consequences of using a SBM are better performance or lower cost.

Unlike AMBs, whose operating principle and mechanical design have reached a general consensus, the operating principles of SBMs are multiple and the resulting designs are diverse. With regards to the operating principle, induction motor, permanent magnet motors, synchronous reluctance motors and switched reluctance motors can all be redesigned to integrate self-bearing functionality. Each type has a different blend of characteristics with regards to the quality of its levitation and torque production, its cost, and complexity. Determining which SBM type is "best" depends on the application, see [6] for some examples. A comprehensive overview of each type of SBM and a comparison of their characteristics is found in [16].

In terms of their mechanical design, SBMs can be realized in a variety of structures. Most SBMs have a traditional cylindrical structure with an inner rotor that governs 3DOF, shown in Figure 1.6(a). Unconventional designs can lead to unique and advantageous characteristics. For example, an outer-rotor-type SBM is designed for a high speed miniature spindle in [57]. An axial-flux SBM consisting of dual rotor disks sandwiched around a rotor is proposed in [95] to eliminate negative stiffness (negative stiffness is described in Chapter 5). A self-bearing slice motor is shown to additionally stabilize the tilting and axial motions of the rotor by reluctance forces [6, 89]. The slice motor is shown in Figure 1.6(b).

Although SBMs are the general topic of research in the latter half of this thesis, specifically Chapters 5-7, our investigation is focused on a sub-class of SBMs, namely the all-Lorentz type. The all-Lorentz type of SBM is a permanent magnet machine unique among

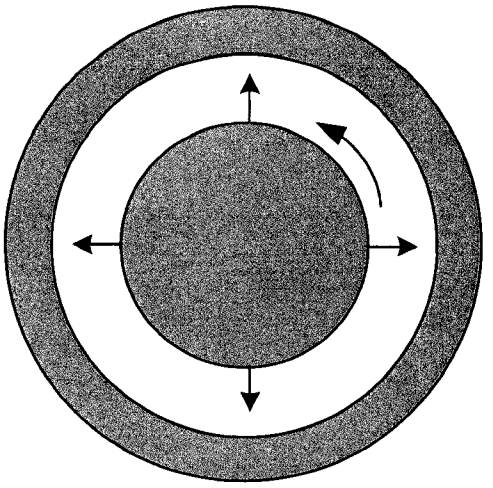

(a) typical SBM, cross section

(b) slice SBM, side view

Figure 1.6: Possible mechanical structures of a SBM. Traditionally, SBMs have a cylindrical structure with an inner rotor and can govern three positional degrees-of-freedom. This is shown in Figure 1.6(a), where the arrows indicate that radial force and torque can be applied to the rotor. Other structures can provide advantages. For example, a self-bearing slice motor, shown in Figure 1.6(b), can additionally stabilize the tilting and axial motion in a passive manner. The arrows indicate the Maxwell forces where the axial component stabilizes axial displacement and tilting. Also shown is the radial component which is overcome by active control.

all types of SBMs because it achieves levitation from the Lorentz-force. By contrast, the majority of SBMs, as shown in a survey in [107], rely on the reluctance force principle as the basis for levitation, similar to the AMB.

The term *all-Lorentz* comes from the fact that the Lorentz force is the basis for both levitation and rotation through a common principle. In fact, the Lorentz force is the basis of torque generation for most motors with the exception of reluctance motors. With regards to the Lorentz-force principle, we are specifically referring to the force on a current-carrying conductor in the presence of an external magnetic field, as given by the well-known cross-product

$$F = iL \times B. \tag{1.5}$$

Here, i is the current flowing through the conductor, L is a vector whose magnitude is the length of wire and whose direction is along the wire and aligned with the direction of

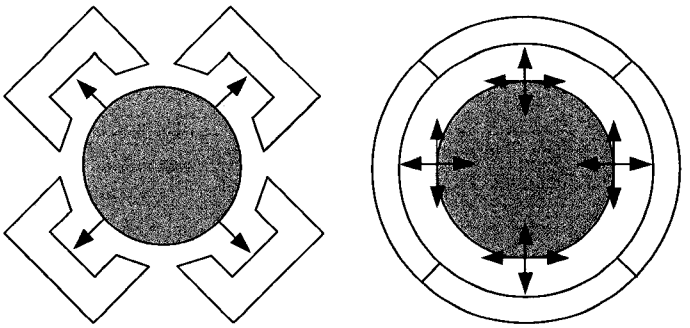

Figure 1.7: Comparison of magnetic levitation principles for a rotor. On the left, the reluctance principle permits generation of unidirectional, attractive forces and is the basis for AMBs. On the right, the Lorentz principle permits generation of bi-directional tangential and normal forces.

conventional current flow, B is the magnetic flux vector, and F is the resulting force vector. To date, all-Lorentz SBMs have been realized through the interaction of permanent magnet flux with winding currents.

The linearity between the magnetic force and the coil current in (1.5) stands in contrast to the reluctance force (1.4) which has a quadratic dependence on the current. Whereas the reluctance force is only attractive as a result of its quadratic dependence, the Lorentz force is bidirectional due to linearity. A contrast of these approaches to magnetically levitating a rotor is shown in Figure 1.7. Due to bidirectionality, the Lorentz force can be attractive or repulsive, and this property has been usefully exploited in the creation of the "inverted planar maglev", a hovering positioning platform [96]. Another interesting property of Lorentz-force-based levitation is that it does not require ferromagnetic material in its construction. "Coreless" stators, as they are called, eliminate parasitic reluctance forces, slotting effects, iron losses, and reduce coil inductance. Whereas reluctance force capacity is fundamentally limited by saturation of the ferromagnetic material, Lorentz-force capacity is limited by coil current and the associated heating.

The principle of the all-Lorentz SBM has been known for some time [9]. Many of the existing approaches use an unequal number of permanent magnet poles and individually controlled coils. For example, work in [90, 123] uses an eight-pole rotor with a four pole stator controlled by six concentrated windings. Reference [61] presents a outer-rotor slice motor consisting of four PM poles on the rotor and six concentrated windings. Improvements to the slice motor concept using Halbach magnets is shown in [89]. In these aforementioned works, one set of three-phase currents provide levitation where the direction of the levitation force is determined by the phase angle. Another set of three-phase

currents provide rotation. Reference [95] presents the design of a disk-type all-Lorentz SBM with a generalized analysis of its operating principle. It is shown that a condition for stable levitation coincides with the well-known $P \pm 2$ principle [88], which states that the stator pole number must be two greater or two less than the rotor pole number.

A new principle for an all-Lorentz SBM was proposed in [23]. Whereas previous approaches used separate sets of three-phase currents to generate levitation and torque and involved an unequal number of rotor and stator poles, the approach in [23] has neither of these characteristics. Instead, the motor circumference is segmented in four quadrants, with each quadrant representing a conventional three-phase PM motor. As demonstrated in [103] and the references therein, an individually controlled Lorentz force from each quadrant contributes to both levitation and torque production.

The "segmented" approach to the all-Lorentz SBM is an interesting alternative basis since each quadrant resembles a linear permanent magnet synchronous motor (LPMSM). Multiphase LPMSMs are known to generate both tangential and normal forces on the translating body, so as to simultaneously enable magnetic suspension and propulsion [124, 7]. Adapting the operating principle of LPMSMs to the segmented all-Lorentz SBM concept provides a great deal of design and control freedom. Figure 1.7 shows the concept of normal and tangential force generation with a segmented all-Lorentz SBM in contrast to force generation from a conventional AMB.

It is the purpose of Chapters 5-7 to study the modeling, control, and design of the segmented all-Lorentz SBM. Henceforth, it shall be referred to as the *toothless self-bearing servomotor* (TSBS). In addition to its novel operating principle, the TSBS has two salient features as implied by its name. First, the design intent of the TSBS is precision servomotoring, i.e. low-speed angular positioning of the rotor. Second, it has a toothless (or slotless) stator whose purpose is to produce smooth torque. The motivating application behind the TSBS is to replace traditional mechanical gimbals in optical tracking systems. Figure 1.8 describes an example application in detail. TSBS technology is also a potential alternative in other uses of rotary positioning platforms (RPPs). In particular, RPPs have a firm presence in semiconductor "fabs" by automating wafer handling throughout a variety of processes [86]. In these applications, yield is directly proportional to cleanliness, and traditional contact bearings are a source of particle contamination. Other applications of the TSBS are foreseeable where precise positioning of a shaft in 6DOF is required.

In summary, the study of AMBs and Lorentz-type SBMs in this thesis are complementary to one another within the broader study of modeling and control of magnetically-

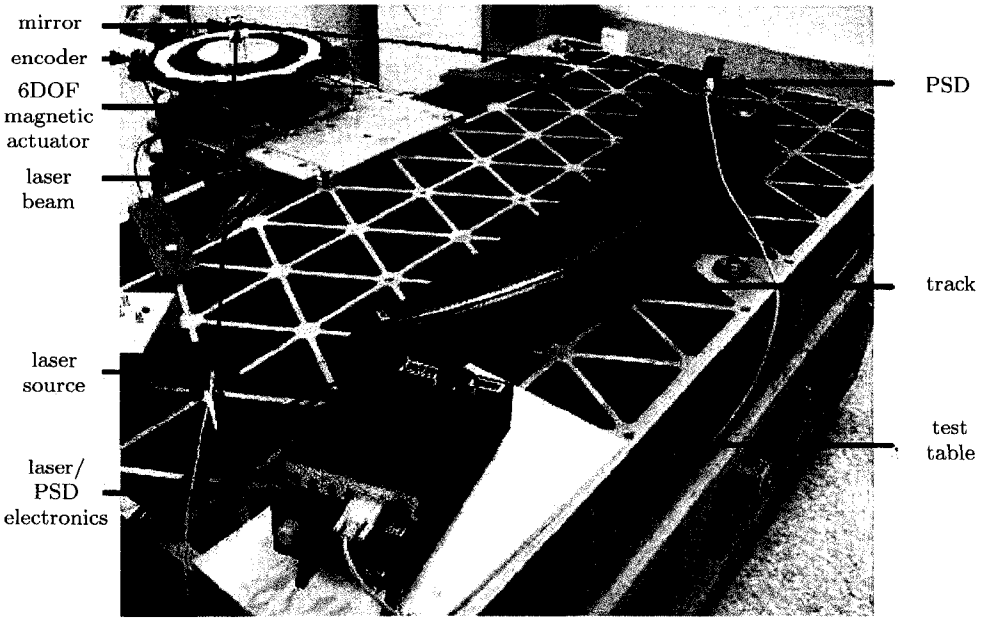

Figure 1.8: Scale setup of an inter-satellite communications cross-link using a toothless self-bearing servomotor (TSBS) in lieu of a traditional mechanical gimbal. The TSBS is part of the "6DOF magnetic actuator" in the figure. A mirror, mounted on the rotor of the TSBS, redirects the laser beam from a stationary source to a moving position sensing device (PSD). Inter-satellite communication cross-links have stringent requirements on angular positioning accuracy. This is because small angular deviations from the reference correspond to significant beam positioning errors when amplified by the large distances between transmitting and receiving stations. The TSBS potentially offers better positioning accuracy and longer life than traditional gimbals due to the absence of mechanical friction. (Reproduced with permission from [100].)

levitated rotors. In fact, studying magnetic levitation through these two devices is comprehensive from an engineering standpoint in the sense that the Lorentz-force and reluctance-force are, to date, the only bases for practical applications of magnetic levitation [10].

1.3 Research contributions

The scope of this thesis is, primarily, modeling and control of magnetically-levitated rotating shafts by means of AMBs and TSBSs. We provide innovation in the modeling, control, and design throughout the next six chapters with the goal of bettering our physical understanding of these devices and improving our control authority over them. Specifically, the research contributions are

- an experimental study of nonlinear tracking controllers for non-rotating shafts sup-

ported by AMBs [44, 46],

- synthesis and experimental validation of nonlinear tracking controllers for rotating shafts supported by AMBs [45, 48],
- a numerical study of a state estimation scheme known as *algebraic differentiation*, and its application to a 1DOF AMB [47],
- a physics-based model of the force and torque characteristics of a TSBS [41, 42],
- a dynamic model and control design of an experimental TSBS [43], and
- a simplified operating principle for a TSBS with associated control system design and experimental validation.

1.4 Thesis overview

Each of these research contributions described in the previous section constitute an individual chapter in this thesis.

Chapter 2 presents an experimental 5DOF AMB system and a detailed dynamic model. Approaches to the nonlinear tracking control problem are described with a presentation of the relevant control theory. Experiments compare the performance of the nonlinear controllers to a conventional design.

Chapter 3 considers the nonlinear tracking control problem when the levitated shaft is rotating. Rotation induces vibration, and the dynamic model is redeveloped to account for this effect. An observer scheme is designed which estimates the disturbances associated with induced vibration, and the nonlinear feedback of Chapter 2 is extended to include vibration suppression.

Chapter 4 considers an alternative state estimation scheme to that proposed in Chapter 3. This new approach is based on algebraic methods to yield successive time derivatives of a signal. The theory behind this estimation technique is described and a numerical study provides insight into the accuracy of the method and its range of application. The chapter concludes with a simulation case study on a single axis AMB.

Chapter 5 initiates an investigation into the operating principles of the TSBS. Nonlinear expressions for bearing force and torque are derived from first principle analysis. The model structure is validated by finite element analysis. The nonlinear model is compared to previous linear modeling efforts in the literature.

Chapter 6 describes an experimental realization of a TSBS. Performance drawbacks are described with respect to conventional control schemes. A dynamic model is derived as a basis for controller modifications. The new control system is based on a time varying coordinate transformation which makes an additional control variable available. We manipulate the additional control variable to achieve input current equalization through a creative use of state observers. Additionally, a dynamic input saturation scheme is established to resolve conflict between the force and torque subsystems in the presence of input saturation.

Chapter 7 explores a new design for the TSBS through manipulation of all of its available control variables. A design is proposed which reduces the number of individually controlled segments from four to two. We present a new dynamic model and control policy along with experimental validation. Our simplified design approximately reduces the power electronic requirements of the original system by a factor of two.

Chapter 8 gives a detailed summary of the research findings and provides potential future research directions.

Chapter 2

Trajectory Tracking of a Non-Rotating Shaft with Active Magnetic Bearings

Our initial study considers the motion control of a non-rotating shaft that is levitated by active magnetic bearings (AMBs). This simplified problem serves the purpose of assessing the feasibility of applying nonlinear control theory to a practical, full scale AMB system. In this chapter, we experimentally compare trajectory tracking strategies, investigating the particular aspects of nonlinearity and overactuation.

2.1 Introduction

Feedback control of AMBs most commonly employ the methods of linear systems control theory. Linear control is most effective when the AMB coils are premagnetized through the use of bias currents. Locally, bias currents yield good linearity in the force-current relationship about the bearing center and, equally important, provide a uniform force slew rate [79]. This latter point can be shown mathematically by considering the force model (1.4) for a one degree-of-freedom (1DOF) AMB. Near the bearing center, where it is safe to assume that the nominal air gap κ is much greater than the displacement y, i.e. $\kappa \gg y$, the magnetic force becomes

$$F = \frac{\beta}{\kappa^2}(i_1^2 - i_2^2),$$

where β is a positive constant and the coil currents are denoted i_1 and i_2. A common biasing technique is known as Constant Current Sum (CCS), where $i_1 = i_b + \Delta i$, $i_2 = i_b - \Delta i$ with bias current i_b and differential current Δi. Therefore we have

$$F = \frac{4\beta i_b}{\kappa^2}\Delta i,$$

which confirms linearity between the magnetic force and the control current. Furthermore, assuming negligible coil resistance, the approximate slew rate of the coil currents is governed by the saturation voltage V_s and nominal coil inductance L_0 of the electrical circuit such that

$$\left|\frac{\mathrm{d}i_k}{\mathrm{d}t}\right| \leq \frac{V_s}{L_0}, \quad 1 \leqslant k \leqslant 2. \tag{2.1}$$

Then, the approximate upper bound on force slew rate is

$$\left|\frac{\mathrm{d}F}{\mathrm{d}t}\right| \leq \frac{4\beta V_s i_b}{\kappa^2 L_0}. \tag{2.2}$$

The bound (2.2) is linearly dependent on bias current and saturation voltage, and is the primary constraint on an AMB's dynamic load capacity [79, 12]. In practice, the saturation voltage is determined by the power of the amplifiers which drive the coils, and the bias current is limited by saturation of the iron.

Bias currents have the drawbacks of heating up the rotor and increasing power losses due to coil resistance, eddy currents, and hysteresis. Although AMBs operated in this manner have lower losses than conventional bearings such as the fluid film type, there remains potential for further reduction. Furthermore, expanding the application of AMBs, e.g. to energy storage flywheels and heart pumps, requires minimal power losses and minimal rotor heating [84, 108]. However, low losses and a high slew-rate limit (the slew-rate limit determines the closed-loop system bandwidth) are competing objectives. A great deal of work has been done to achieve an optimal compromise. Work in [82] investigates the trade-off between losses and slew-rate limit using constrained quadratic optimization. Work in [53] also considers an optimization problem for current allocation which minimizes losses subject to a voltage saturation constraint. An adaptive variable bias approach is studied in [106] that minimizes energy consumption for a pre-specified bearing stiffness and orbital size.

An AMB loses its linear characteristic when operated with low, or zero, bias and likewise when the shaft is displaced sufficiently far off the bearing center. Under either or all of these conditions, nonlinear control techniques become suitable [54]. For AMBs, feedback linearization can render consistent performance independent of the system's operating point. The earliest known example of this is in [73], where a static state feedback linearizing control is combined with a complementary actuation scheme to eliminate bias currents. A similar approach is taken in [67] through the Current Almost Complimentary (CAC) condition in conjunction with a flatness-based nonlinear feedback. The CAC condition uses a small time-varying bias to prevent large voltages that can arise from purely complementary

actuation schemes. Extensions to the work on feedback linearization address robustness to model error and disturbance [118, 13, 56, 71]. Experimental validation of these methods has been shown for 1DOF systems [125, 68, 71], 4DOF [67], and 5DOF [131] systems. Alternate feedback linearization-based designs are studied in [68, 69, 130]. The aim of these alternative designs is to improve the dynamic response in light of voltage saturation. For example, a Constant Flux Sum (CFS) condition is derived in [68] to obtain a constant bound on force slew rate. For a 1DOF system, the CFS controller leads to improved tracking performance relative to a control based on a CCS linear feedback and control based feedback linearization with zero bias. In [130], a flatness-based nonlinear control incorporating the CCS condition is derived. This approach was experimentally applied to a boring process using a 5DOF system. Alternative nonlinear control approaches to AMBs based on integrator backstepping [24, 116], passivity [126], and zero-bias H_∞ [117] have been considered as well.

Nonlinear control offers the potential benefits of improved operating efficiency and a larger range of control authority, however, there is a noticeable lack of experimental validation of such techniques beyond 1DOF. Extension to 5DOF system is a greater challenge because of the impact of multivariable coupling through sensor-actuator non-collocation and shaft flexibility. In this chapter we conduct an experimental study of nonlinear controllers on a commercially available 5DOF test stand. The performance of CAC- and CCS-based nonlinear tracking controllers are compared with an industry standard decentralized proportional-integral-derivative (PID) approach. The comparison is based on each controller's unbalance response and ability to guide a non-rotating shaft along a time-varying trajectory.

2.2 System description and modeling

The AMB system under consideration was manufactured by *SKF/Revolve Magnetic Bearings Inc.* (Calgary, AB) and is a pedagogical test stand. The system offers several horizontal shaft configurations, and for the following work a 305 mm ($12''$) long, 5DOF shaft assembly is chosen. Figure 2.1 shows the experimental 5DOF system describing each component. The assembly consists of a 9.5 mm ($3/8''$) diameter shaft upon which are mounted two radial bearing rotors (also known as *journals*) and a disk. The journals form part of the radial magnetic bearings, and the disk is part of the axial magnetic bearing. The journals have an outer diameter of 34.3 mm, a length of 48.0 mm, and span 178.0 mm from center to

center. The disk has an outer diameter of 66.0 mm. The journal and disk are each enclosed by a housing which consist of the stator, two-sided variable reluctance-type displacement sensors, and touchdown bearings. The touchdown bearings rest the de-levitated shaft and prevent contact between the rotors and the stators. The entire shaft assembly is coupled to a DC motor by a flexible coupling. The system has a specified shaft speed range of $2,000 - 10,000$ r/min and the motor has a maximum speed of $15,000$ r/min. Some bearing specifications are provided in Table 2.1.

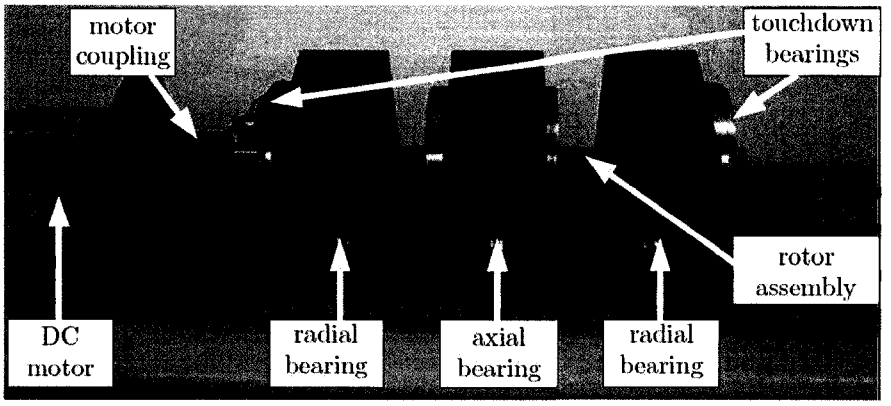

Figure 2.1: Research test stand from SKF/Revolve Magnetic Bearings. Radial and axial active magnetic bearings levitate the shaft in five degrees of freedom, and a motor coupled to the shaft provides rotation up to $15,000$ r/min. The touchdown bearings prevent contact between the rotors and stators, and rest the delevitated shaft.

Specification	radial bearing	axial bearing
static load capacity	76 N	205 N
saturation current	3.0 A	2.8 A
nominal gap	525 μm	783 μm
stator inner diameter	35.1 mm	38.6 mm
stator outer diameter	82.8 mm	71.4 mm
stator length	12.7 mm	13.5 mm
rotor outer diameter	34.3 mm	66.0 mm

Table 2.1: Magnetic bearing technical specifications for the research test stand shown in Figure 2.1

Modeling of AMBs is well-established [111] and we consider here a standard dynamic model for the shaft supported by AMBs in 5DOF. Figure 2.2 labels our chosen coordinate system and forces acting on the shaft assembly. Figure 2.3 shows a schematic of a cross-section of the system detailing its geometry. Assuming that the shaft is a perfectly rigid

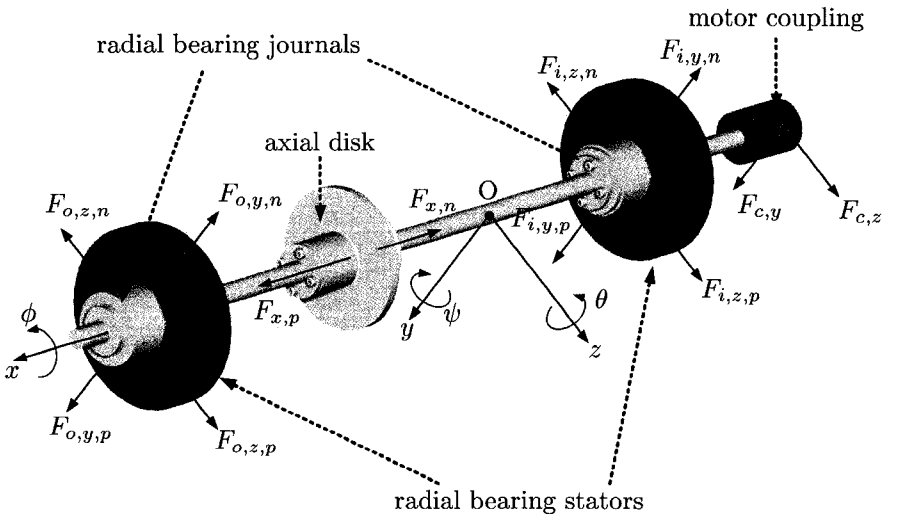

Figure 2.2: Shaft assembly, motor coupling and radial bearing stators for a five degree-of-freedom magnetic bearing system. The shaft assembly is treated as a rigid body for the purpose of modeling.

body, the dynamic equations are [81]

$$m\ddot{x} = F_x, \tag{2.3a}$$

$$m\ddot{y} = F_{o,y} + F_{i,y} + F_{c,y} + mg_y, \tag{2.3b}$$

$$m\ddot{z} = F_{o,z} + F_{i,z} + F_{c,z} + mg_z, \tag{2.3c}$$

$$J_z\ddot{\psi} = (l_{i,a} + x)F_{i,z} - (l_{o,a} - x)F_{o,z} - J_x\omega\dot{\theta} + l_cF_{c,z}, \tag{2.3d}$$

$$J_y\ddot{\theta} = (l_{o,a} - x)F_{o,y} - (l_{i,a} + x)F_{i,y} + J_x\omega\dot{\psi} - l_cF_{c,y}, \tag{2.3e}$$

where x, y, z denote the coordinates of the center of mass c_m relative to the origin O of the inertial frame. The angles ψ, θ denote the small angle rotation of the shaft with respect to the translated y and z axes. When the shaft is centered in all three bearings $(x, y, z, \psi, \theta) = 0$. The angular velocity of the shaft about the x-axis is denoted $\omega = \dot{\phi}$ and assumed to be constant. The y- and z-axis components of gravity are denoted g_y and g_z respectively, and the coordinate system is oriented such that $g_y = g_z$. The shaft has a mass m and principle moments of inertia J_x, J_y, J_z which, by the shaft's symmetry, we have $J_y = J_z = J$. Although the particular shaft assembly being considered is not very gyroscopic, we retain the terms $J_x\omega\dot{\theta}, J_x\omega\dot{\psi}$ in the interest of generality. The distances from the inboard (subscript i) and outboard (subscript o) stators to O are denoted $l_{i,a}$ and $l_{o,a}$ respectively. The motor coupling forces are denoted[1] $F_{c,y/z}$ and are modeled as linear

[1]The shorthand expression $F_{c,y/z}$ streamlines notation by referring to both $F_{c,y}$ and $F_{c,z}$

springs

$$F_{c,y} = -K(y - l_c\theta),$$

$$F_{c,z} = -K(z + l_c\psi).$$

The distance from c_m to the point at which $F_{c,y/z}$ act is l_c, and the spring constant is K. The axial bearing force is denoted F_x and the outboard and inboard radial bearing forces are denoted $F_{o/i,y/z}$. Each of these forces is the summation of positive (subscript p) and negative (subscript n) components generated by opposing coils. Based on the magnetic circuit assumption described in Chapter 1, the forces generated by the AMBs are expressed as

$$\begin{aligned} F_x &= F_{x,p} - F_{x,n} \\ &= \beta_x \left(\frac{i_{x,p}^2}{(\kappa_x - x)^2} - \frac{i_{x,n}^2}{(\kappa_x + x)^2} \right), \end{aligned} \tag{2.4a}$$

$$\begin{aligned} F_{i/o,y/z} &= F_{i/o,y/z,p} - F_{i/o,y/z,n} \\ &= \beta_{i/o,y/z} \left(\frac{i_{i/o,y/z,p}^2}{(\kappa - \xi_{i/o,y/z})^2} - \frac{i_{i/o,y/z,n}^2}{(\kappa + \xi_{i/o,y/z})^2} \right), \end{aligned} \tag{2.4b}$$

where κ (respectively κ_x) is the nominal air gap between the radial (axial) bearing rotor

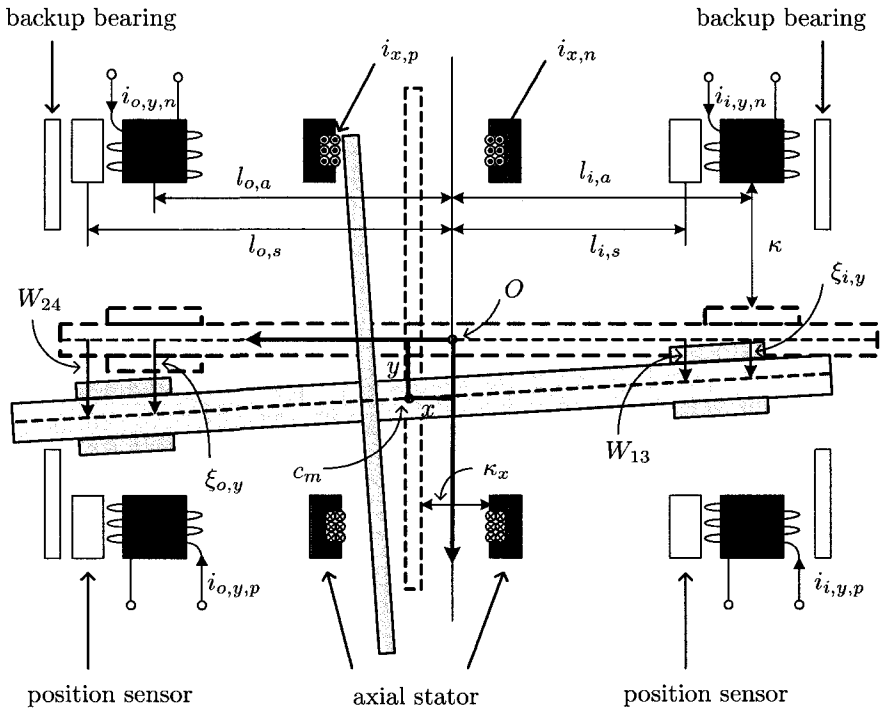

Figure 2.3: Cross section of Figure 2.2 in the $x - y$ plane. Motor coupling not shown. "Backup bearing" is synonymous with "touchdown bearing."

and stator. The bearing force constants are $\beta_x, \beta_{i/o,y/z}$, and $\xi_{i/o,y/z}$ denote the radial displacements of the shaft in the planes $x = l_{o,a}$ and $x = -l_{i,a}$. The displacements $\xi_{i/o,y/z}$ are geometrically related to the center of mass coordinates by

$$\begin{aligned}
\xi_{o,y} &= y + (l_{o,a} - x)\theta + \bar{\xi}_{o,y}, \\
\xi_{o,z} &= z - (l_{o,a} - x)\psi + \bar{\xi}_{o,z}, \\
\xi_{i,y} &= y - (l_{i,a} + x)\theta + \bar{\xi}_{i,y}, \\
\xi_{i,z} &= z + (l_{i,a} + x)\psi + \bar{\xi}_{i,z},
\end{aligned}$$

where $\bar{\xi}_{i/o,y/z}$ denote *magnetic offsets*. Magnetic offsets represent the distances between the center of the shaft and the center of the radial AMB stators when $(x, y, z, \psi, \theta) = 0$. Ideally, magnetic offsets do not exist because sensing and actuating components are supposed to be concentrically aligned. As a result they are typically excluded from AMB models. In practice, magnetic offsets do exist and lead to bias forces. Bias forces ultimately lead to static offset in closed-loop that must be compensated by integral control or disturbance estimation and cancelation.

The axial and radial bearing coils are driven by currents $i_{x,p/n}, i_{i/o,y/z,p/n}$ which are inputs for control design purposes. In fact, $i_{x,p/n}, i_{i/o,y/z,p/n}$ are actually reference currents to servoamplifiers. These reference currents are tracked by inner-loop current controllers so that sufficient time scale separation between the electrical and mechanical subsystem dynamics is achieved.

2.3 Parameter identification

We describe here a procedure to obtain a best-fit of the force constants $\beta_{i/o,y/z}$ and magnetic offsets $\bar{\xi}_{i/o,y/z}$ to experimental data. The magnetic offsets are unknown because they are effectively calibration errors. The force constants can be analytically determined from a detailed magnetic circuit analysis, but they would be poorer approximations than data fits because they cannot account for flux leakage in the air gap.

The identification procedure is simplified by decoupling the shaft from the motor and then stabilizing the axial and tilting motion of the shaft in closed-loop, with pre-existing, "working" controllers, so that $(x, \psi, \theta) = 0$ and the shaft is in equilibrium. Under these

conditions, the model (2.3) becomes

$$0 = F_x, \tag{2.5a}$$

$$0 = F_{o,y} + F_{i,y} + mg_y, \tag{2.5b}$$

$$0 = F_{o,z} + F_{i,z} + mg_y, \tag{2.5c}$$

$$0 = l_{i,a}F_{i,z} - l_{o,a}F_{o,z}, \tag{2.5d}$$

$$0 = l_{o,a}F_{o,y} - l_{i,a}F_{i,y}. \tag{2.5e}$$

Solving for the equilibrium forces in (2.5) gives

$$F_{o,y} = F_{o,z} = -mg_y\left(\frac{l_{i,a}}{l_{o,a}+l_{i,a}}\right) = -m_o g_y, \tag{2.6a}$$

$$F_{i,y} = F_{i,z} = -mg_y\left(\frac{l_{o,a}}{l_{o,a}+l_{i,a}}\right) = -m_i g_y, \tag{2.6b}$$

where effective masses $m_{i/o}$ are defined for each radial bearing. For simplicity, the remainder of the procedure is presented only in the case of the inboard y-axis. We consider the force model (2.4a), and impose on it the CCS condition

$$i_{i,y,p} = i_b + \Delta i_{i,y},$$

$$i_{i,y,n} = i_b - \Delta i_{i,y},$$

where i_b is the bias current and $\Delta i_{i,y}$ is a differential current. Since $x = \psi = \theta = 0$, then $\xi_{o,y} = y$ and the force expression becomes

$$F_{i,y} = \frac{\beta_{i,y}(i_b + \Delta i_{i,y})^2}{(\kappa - \bar{\xi}_{i,y} - y)^2} - \frac{\beta_{i,y}(i_b - \Delta i_{i,y})^2}{(\kappa + \bar{\xi}_{i,y} + y)^2}. \tag{2.7}$$

Equating (2.7) to (2.6b) we have

$$m_i g_y = \frac{\beta_{i,y}(i_b - \Delta i_{i,y})^2}{(\kappa + \bar{\xi}_{i,y} + y)^2} - \frac{\beta_{i,y}(i_b + \Delta i_{i,y})^2}{(\kappa - \bar{\xi}_{i,y} - y)^2}.$$

Data is collected over a range of y and corresponding $\Delta i_{i,y}$. Next, we define the cost function

$$\epsilon[k](\beta_{i,y}, \bar{\xi}_{i,y}) = \frac{\beta_{i,y}(i_b - \Delta i_{i,y}[k])^2}{(\kappa + \bar{\xi}_{i,y} + y[k])^2} - \frac{\beta_{i,y}(i_b + \Delta i_{i,y}[k])^2}{(\kappa - \bar{\xi}_{i,y} - y[k])^2} - m_i g_y \tag{2.8}$$

where $(\Delta i_{i,y}[k], y[k]), 1 \leqslant k \leqslant N$ denotes the data set. The nonlinear least squares problem

$$\min_{(\beta_{i,y}, \bar{\xi}_{i,y}) \in U} \sum_{k=1}^{N} \varepsilon^2[k]$$

is solved for $U = \{(\beta_{i,y}, \bar{\xi}_{i,y}) \in \mathbb{R}^2 : 0 < \beta_{i,y}, -\kappa < \bar{\xi}_{i,y} < \kappa\}$. For comparison purposes, a fit is performed with a linearized force model

$$\epsilon(K_i, K_\xi)[k] = K_i \Delta i_{i,y}[k] + K_\xi y[k] - m_i g_y. \tag{2.9}$$

The results are based on $N = 120,000$ data samples over a range of $(y, z) \in [-100, 100]$ μm$\times$ $[-100, 100]$ μm, and Table 2.2 presents the average values $\beta, \bar{\xi}$ for the inboard AMB. We notice that the nonlinear force model results in a superior fit to data. This better fit is due to both the nonlinear dependence of the force model and the introduction of magnetic offset.

Nonlinear		Linear	
β	$6.95 \cdot 10^{-7}$ N-m^2/A^2	k_i	68.5 N/A
$\bar{\xi}$	$-1.15 \cdot 10^{-4}$ m	k_x	$1.62 \cdot 10^5$ N/m
$\|\epsilon\|_2^2$	119.2 N^2	$\|\epsilon\|_2^2$	6668.9 N^2

Table 2.2: Average parameter values and error norm for linear and nonlinear AMB force models. The nonlinear force model (2.8) improves the fit-to-data relative to the linearized force model (2.9).

Table 2.3 provides the remaining model parameter values. Mass and geometry properties are obtained from the specifications of the experimental AMB system and the inertias are obtained from software analysis.

Parameter	Value	Parameter	Value
$l_{i,s}$	0.078 m	$l_{o,s}$	0.100 m
$l_{i,a}$	0.097 m	$l_{o,a}$	0.081 m
l_c	0.155 m	K	1200 N/m
J_x	$1.71 \cdot 10^{-4}$ kg-m^2	J_y	$5.84 \cdot 10^{-3}$ kg-m^2
m	0.98 kg	β_x	$5.0 \cdot 10^{-6}$ N-m^2/A^2
κ	$5.25 \cdot 10^{-4}$ m	κ_x	$7.83 \cdot 10^{-4}$ m

Table 2.3: Model parameters of the experimental 5 degree-of-freedom AMB system. The system is described in detail in Chapter 2, Section 5.

2.4 Control

In this section, nonlinear state feedback is formulated to track the motion of a non-rotating shaft. The synthesis of a nonlinear controller for an AMB system can be viewed as a two step procedure. In the first step, we consider the design of a tracking control law assuming that the forces $F_{x,p/n}, F_{i/o,y/z,p/n}$ are inputs to (2.3). In the second step, we invert the force expressions (2.4) to obtain the control currents as function of the control forces. This inversion is non-unique because magnetic force is quadratic in coil current and because the

number of independently controlled coils (ten) exceeds the number of force components generated (five). Two approaches are considered here to obtain a unique force-to-current map. Finally, we design a conventional decentralized PID controller for comparison purposes.

2.4.1 Flatness-based trajectory tracking

Since its introduction in the middle of the 1990s [32, 33], differential flatness has been applied to industrially relevant problems such as heating processes [59], vehicle drive-by-wire [129], power systems [38], magnetic bearings [67] and automotive solenoid valves [19]. In this section we give a practical definition of flatness and then show how it can be applied to the 5DOF AMB system.

Consider a state-space system of the form

$$\dot{x} = f(x, u) \tag{2.10}$$

for input $u \in \mathbb{R}^m$ and state $x \in \mathbb{R}^n$. Such a system is called *differentially flat* if there exists an "output" $y \in \mathbb{R}^m$ such that

$$y = h(x, u, \dot{u}, \ldots, u^{(q)}),$$

where $u^{(q)} = \mathrm{d}^q u / \mathrm{d}t^q$ denotes the q^{th} derivative with respect to time, satisfying two properties:

1. All components of the state x and input u can be expressed in terms of y and a finite number of its time derivatives. Mathematically, this requires the existence of locally defined functions $\mathcal{A}, \mathcal{B}$ such that

$$x = \mathcal{A}(y_1, \dot{y}_1, \ldots, y_1^{(r_1)}, \ldots, y_m, \dot{y}_m, \ldots, y_m^{(r_m)}), \tag{2.11a}$$

$$u = \mathcal{B}(y_1, \dot{y}_1, \ldots, y_1^{(r_1+1)}, \ldots, y_m, \dot{y}_m, \ldots, y_m^{(r_m+1)}), \tag{2.11b}$$

   for positive integers r_i, $1 \leq i \leq m$.

2. The components of y are functionally independent, i.e. they are not related by any differential equation of the form

$$P(y, \dot{y}, \ldots, y^{(s)}) = 0.$$

The function y, called a *flat output*, freely parameterizes the system variables x and u. It is a special type of parameterization in that Property 1 implies all state and input trajectories can

be uniquely determined from y without integrating the system equations (2.10). Presently, there does not exist a general characterization of flat systems, and as a consequence, one may have to resort to finding a flat output by a combination of inspection and physical reasoning.

The motion planning problem for a flat system is simplified if the trajectories are designed in the flat output coordinates. Given a feasible trajectory $y(t)$ for the flat output, the corresponding trajectories for the state and open-loop control can be readily computed from the static relations (2.11a)-(2.11b). Alternatively, to transfer the state of a flat system from x_1 at time $t = t_1$ to x_2 at time $t = t_2$, the flat output trajectory must satisfy

$$x_k = \mathcal{A}\big(y(t_k), \dot{y}(t_k), \ldots, y^{(r)}(t_k)\big), \quad 1 \leq k \leq 2. \tag{2.12}$$

Conditions (2.12) impose constraints on the derivatives of $y(t)$ up to order r at the endpoints $t = t_1$ and $t = t_2$. Once we design a trajectory for the flat output satisfying (2.12), we use (2.11b) to obtain the nominal open-loop control steering the system from x_1 to x_2.

To maintain the system's state on its reference trajectory in the face of modeling errors and disturbances, we can design a closed-loop control for a flat system in a manner that is closely related to feedback linearization. A flat system can be transformed, using (2.11b) into a linear, controllable system of the form

$$y_i^{(r_i+1)} = v_i, \qquad 1 \leq i \leq m. \tag{2.13}$$

This transformation, via *endogenous feedback*, is more general than equivalence via diffeomorphism and static state feedback [76] since the dimension $r = \sum_i^m (r_i + 1)$ of the transformed system (2.13) satisfies $r \geq n$ [67]. For example, the kinematic car is a flat system that is not static state feedback linearizable since $r \geq n$ [127]. For such systems, endogenous feedback may be interpreted as a special type of dynamic feedback linearization [14].

The auxiliary inputs v_i can be designed to yield exponential convergence of the flat outputs y_i onto their reference trajectories $y_{i,r}$ by the feedback

$$v_i = y_{i,r}^{(r_i+1)} + \sum_{j=0}^{r_i} K_{i,j}(y_i^{(j)} - y_{i,r}^{(j)}), \qquad 1 \leq i \leq m.$$

The gains $K_{i,j}$ can be designed to place the poles of tracking error dynamics in the open left-half complex plane for each of the m independent subsystems. By appropriate design of the reference trajectories, possible singularities in $\mathcal{A}$ and $\mathcal{B}$ can be avoided [78]. In addition,

constraints on state or input variables can be obeyed by trajectory optimization using, for example, nonlinear programming techniques [19].

We demonstrate the idea of flatness-based trajectory tracking through endogenous force feedback on the system (2.3). We choose the flat output as the center of mass coordinates x, y, z, ψ, θ and treat the forces $F_x, F_{i/o,y/z}$ as virtual inputs. Note that if the currents $i_{x,p/n}, i_{i/o,y/z,p/n}$ are taken as the system inputs for the flatness-based design, then we would require a flat output of higher dimension. A flatness-based design assuming current control is considered in [67], but the end result is the same as having assumed a flatness-based force control followed by force-to-current inversion. The latter route, described here, simplifies the presentation.

Taking the state of the system as $x, y, z, \psi, \theta, \dot{x}, \dot{y}, \dot{z}, \dot{\psi}, \dot{\theta}$ it is readily seen there exists $\mathcal{A}$ which satisfies (2.11a). The existence of $\mathcal{B}$ satisfying (2.11b) follows from

$$F_x(\ddot{x}) = m\ddot{x}, \tag{2.14a}$$

$$F_{i,y}(x, y, \theta, \dot{\psi}, \ddot{y}, \ddot{\theta}) = \frac{m(l_{o,a} - x)(\ddot{y} - g_y) + J_x\omega\dot{\psi} - J\ddot{\theta} - (l_{o,a} - x + l_c)(-K(y - l_c\theta))}{l_{o,a} + l_{i,a}}, \tag{2.14b}$$

$$F_{o,y}(x, y, \theta, \dot{\psi}, \ddot{y}, \ddot{\theta}) = \frac{m(l_{i,a} + x)(\ddot{y} - g_y) - J_x\omega\dot{\psi} + J\ddot{\theta} - (l_{i,a} + x - l_c)(-K(y - l_c\theta))}{l_{o,a} + l_{i,a}}, \tag{2.14c}$$

$$F_{i,z}(x, z, \psi, \dot{\theta}, \ddot{z}, \ddot{\psi}) = \frac{m(l_{o,a} - x)(\ddot{z} - g_y) + J_x\omega\dot{\theta} + J\ddot{\psi} - (l_{o,a} - x + l_c)(-K(z + l_c\psi))}{l_{o,a} + l_{i,a}}, \tag{2.14d}$$

$$F_{o,z}(x, z, \psi, \dot{\theta}, \ddot{z}, \ddot{\psi}) = \frac{m(l_{i,a} + x)(\ddot{z} - g_y) - J_x\omega\dot{\theta} - J\ddot{\psi} - (l_{i,a} + x - l_c)(-K(z + l_c\psi))}{l_{o,a} + l_{i,a}}, \tag{2.14e}$$

which are globally defined maps. The endogenous force feedback is simply (2.14) where

$$\ddot{x} = v_x, \tag{2.15a}$$

$$\ddot{y} = v_y, \tag{2.15b}$$

$$\ddot{z} = v_z, \tag{2.15c}$$

$$\ddot{\psi} = v_\psi, \tag{2.15d}$$

$$\ddot{\theta} = v_\theta, \tag{2.15e}$$

and $v_x, v_y, v_z, v_\psi, v_\theta$ represent auxiliary inputs. Individual chains of integrators result from the feedback (2.14)-(2.15). Standard linear feedback control methodology can be applied

to design the auxiliary inputs. For instance, in the axial direction we choose

$$v_x = \ddot{x}_r - k_2(\dot{x} - \dot{x}_r) - k_1(x - x_r) - k_0 \int_0^t (x(\tau) - x_r(\tau))\mathrm{d}\tau, \tag{2.16}$$

where x_r denotes a reference trajectory that is at least a twice differentiable with respect to time. This resulting tracking error dynamics are

$$\ddot{e}_x + k_2\dot{e}_x + k_1 e_x + k_0 \int_0^t e_x(\tau)\mathrm{d}\tau = 0.$$

The controller gains k_0, k_1, k_2 are chosen to ensure the tracking error $e_x = x - x_r$ converges to zero exponentially. The integral in (2.16) compensates static offset resulting from magnetic offset and static loading [36]. Similar expressions to (2.16) for $v_y, v_z, v_\psi, v_\theta$ are used to stabilize the tracking errors in y, z, ψ, θ.

The tracking control law assumes knowledge of x, y, z, ψ, θ, their derivatives, and their integrals. The axial displacement x is directly measured and y, z, ψ, θ are obtained indirectly from the radial shaft displacements in the sensor planes at $x = l_{o,s}$ and $x = -l_{i,s}$, see Figure 2.3. The inboard measurements are denoted V_{13}, W_{13} and the outboard measurements are denoted V_{24}, W_{24}. The coordinates x, y, z, ψ, θ are geometrically related to $V_{13}, W_{13}, V_{24}, W_{24}$ by the expressions

$$W_{24} = y + (l_{o,s} - x)\theta, \tag{2.17a}$$

$$V_{24} = z - (l_{o,s} - x)\psi, \tag{2.17b}$$

$$W_{13} = y - (l_{i,s} + x)\theta, \tag{2.17c}$$

$$V_{13} = z + (l_{i,s} + x)\psi. \tag{2.17d}$$

Solving (2.17) for y, z, ψ, θ yields

$$\begin{aligned}
\theta &= \frac{(W_{24} - W_{13})}{l_{o,s} + l_{i,s}}, \\
\psi &= \frac{(V_{13} - V_{24})}{l_{o,s} + l_{i,s}}, \\
y &= W_{13} + (l_{i,s} + x)\theta, \\
z &= V_{24} + (l_{o,s} - x)\psi.
\end{aligned}$$

2.4.2 Force-to-current inversion

Having synthesized force feedback that renders asymptotic trajectory tracking, we consider now how to map the forces $F_x, F_{i/o,y/z}$ to the coil currents $i_{x,p/n}, i_{i/o,y/z,p/n}$. We recall the general force model

$$F = \beta_x \left(\frac{i_p^2}{(\kappa - \xi)^2} - \frac{i_n^2}{(\kappa + \xi)^2} \right), \tag{2.18}$$

remark that the force F is overspecified in terms of the control currents i_p, i_n. Therefore force-to-current inversion is non-unique. Inversion based on performance and power efficiency criteria have been extensively studied [82]. The most common approach, as stated in the introduction to this Chapter, is the use of bias currents and CCS such that, for example $i_p = i_b + \Delta i$ and $i_n = i_b - \Delta i$. Application of CCS is usually accompanied by linearization of the force model about an operating point $(\bar{\Delta i}, \bar{\xi})$ so as to render the local approximation

$$F \approx K_i(\Delta i - \bar{\Delta i}) + K_\xi(\xi - \bar{\xi}). \tag{2.19}$$

The coefficients K_i, K_ξ are a function of the operating point and the approximation (2.19) loses accuracy as the deviations $\Delta i - \bar{\Delta i}$ and $\xi - \bar{\xi}$ grow.

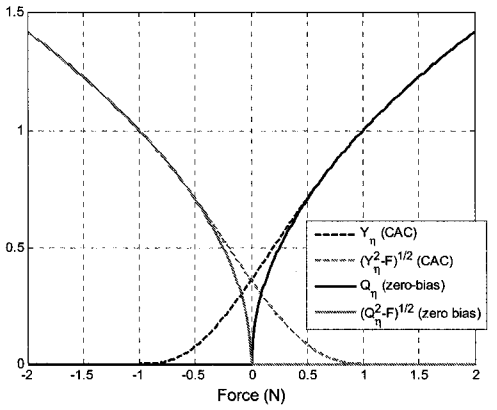

Figure 2.4: Comparison of the complementary and almost complementary functions [67]. In this example, $\eta = 1$ N.

An alternative force-to-current inversion scheme is that which avoids bias currents. Zero-bias operation is a nonlinear control scheme because it employs a hard switching condition among opposing coils. Specifically, only one coil is energized at a time to supply the desired force. Zero-bias inversion can be expressed as

$$i_p = \frac{\kappa - \xi}{\sqrt{\beta}} Q_\eta(F), \tag{2.20a}$$

$$i_n = \frac{\kappa + \xi}{\sqrt{\beta}} \sqrt{Q_\eta^2(F) - F}, \tag{2.20b}$$

where Q_η is the *complementary function* [67]

$$Q_\eta(F) = \begin{cases} \sqrt{F} & F \geq 0, \\ 0 & F < 0. \end{cases} \tag{2.21}$$

Although (2.20) is implementable from a practical viewpoint, the expressions for i_p and i_n are, theoretically, not continuously differentiable in F. For instance, when $F > 0$, we have $i_p = (\kappa - \xi)\sqrt{\frac{F}{\beta}}$ and the rate-of-change of force for a fixed shaft position is given by

$$\frac{\mathrm{d}F}{\mathrm{d}t} = \frac{2\sqrt{F/\beta}}{\kappa - \xi}\frac{\mathrm{d}i_p}{\mathrm{d}t},$$

which is a function of the force applied. The implication is that crossing the zero-force point in (2.20) requires an infinite rate-of-change of current which cannot be realized in practice by servoamplifiers.

We can avoid the control singularity associated with zero-bias inversion by employing soft switching, introduced in [67] as the current almost complementary (CAC) inversion. The CAC inversion is expressed as

$$i_p = \frac{\kappa - \xi}{\sqrt{\beta}} Y_\eta(F), \tag{2.22a}$$

$$i_n = \frac{\kappa + \xi}{\sqrt{\beta}} \sqrt{Y_\eta^2(F) - F}, \tag{2.22b}$$

where Y_η is the *almost complementary function*

$$Y_\eta(F) = \begin{cases} \sqrt{F} & F \geq \eta, \\ P_\eta(F) & -\eta \leq F < \eta, \\ 0 & F < -\eta. \end{cases} \tag{2.23}$$

A polynomial function of force P_η replaces the zero-bias condition on the interval $-\eta \leqslant F \leqslant \eta$ where η is a small force that we choose. To ensure a bounded rate-of-change of both voltage and current, we require P_η to be at least twice differentiable. Therefore, P_η must satisfy the contact conditions

$$\begin{aligned} P_\eta(-\eta) = \frac{\mathrm{d}P}{\mathrm{d}F}(-\eta) = \frac{\mathrm{d}^2P}{\mathrm{d}F^2}(-\eta) &= 0, \\ P_\eta(\eta) &= \sqrt{\eta}, \\ \frac{\mathrm{d}P}{\mathrm{d}F}(\eta) &= \frac{1}{2\sqrt{\eta}}, \\ \frac{\mathrm{d}^2P}{\mathrm{d}F^2}(\eta) &= -\frac{1}{4\sqrt{\eta^3}}, \end{aligned}$$

which is true for the function

$$P_\eta = \frac{15}{16}\eta^{-\frac{5}{2}}(F+\eta)^3 - \frac{13}{16}\eta^{-\frac{7}{2}}(F+\eta)^4 + \frac{17}{64}\eta^{-\frac{9}{2}}(F+\eta)^5 - \frac{1}{32}\eta^{-\frac{11}{2}}(F+\eta)^6.$$

The CAC inversion (2.22) implies that for larger forces, i.e. $|F| \geqslant \eta$, only the coil corresponding to the direction of the desired force is energized while the other is shut off.

For smaller forces, i.e. $|F| < \eta$, both coils are energized and there is a small bias current. A comparison of the complementary and almost complementary functions is shown in Figure 2.4 for $\eta = 1$ N. Although the CAC inversion circumvents the singularity associated with the zero force point $F = 0$, it will still have an inferior dynamic response to that obtained using the traditional approach of CCS because the force slew-rate using CAC remains non-uniform.

Finally, we now consider inversion of the force relation under the CCS assumption. This is simply the traditional approach of biasing the coils with the exception that we do not linearize the resulting force relation. The advantage in this approach is in accounting for the inverse quadratic dependence of the force relation with respect to position, thus making this nonlinear inversion suitable for a wider range of shaft positioning. Its advantage over zero- and low-bias schemes is that it achieves a more uniform force slew rate, and ultimately an improved dynamic response. The force expression subject to CCS is

$$F = \frac{\beta(i_b + \Delta i)^2}{(\kappa - \xi)^2} - \frac{\beta(i_b - \Delta i)^2}{(\kappa + \xi)^2}. \tag{2.24}$$

Inverting (2.24) gives the control law

$$\Delta i = \begin{cases} \frac{-\beta(\xi^2+\kappa^2)i_b - \beta(\xi^2-\kappa^2)\sqrt{F\xi\kappa/\beta + i_b^2}}{2\xi\beta\kappa} & \xi \neq 0, \\ F\kappa^2/(4\beta i_b) & \xi = 0. \end{cases} \tag{2.25}$$

The case for $\xi = 0$ is determined by applying l'Hôpital's rule. To ensure a non-negative discriminant in (2.25), it is sufficient to impose the limits

$$|F| \leq \frac{4\beta i_b^2}{(\kappa - \xi)^2}$$

which are obtained by

$$|\Delta i| \leq i_b.$$

In practice each coil is limited to a maximum current of I_s. Setting $i_b = I_s/2$ enables the full operating range of $i_{p/n}$ and provides the maximum force slew rate, as as approximately determined by (2.2).

2.4.3 Decentralized PID

Decentralized PID control, which is the most commonly applied control scheme for AMBs, is included here as a basis for comparison to the nonlinear tracking controllers. The PID design considered is based on the commercial controller *MB350* included with the experimental test stand from *SKF/Revolve Magnetic Bearings* (Calgary, AB). It utilizes CCS

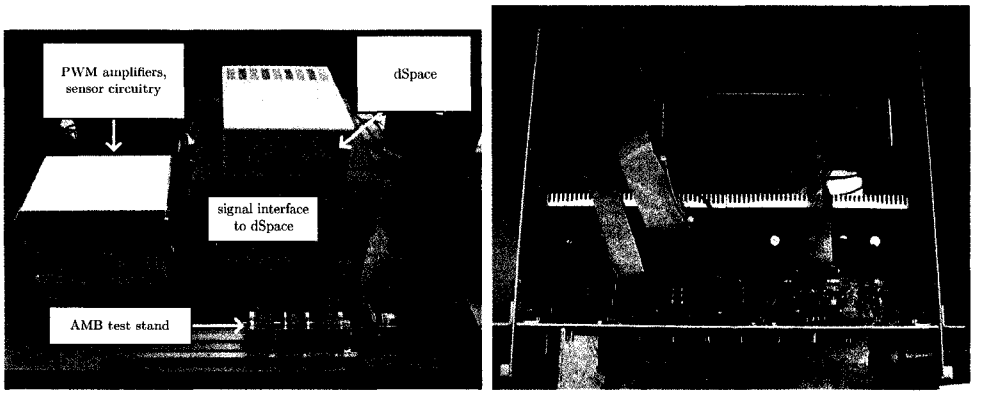

(a) overall testbench (b) AMB drive circuitry

Figure 2.5: The University of Alberta magnetic bearing test bench. It consists of an AMB test stand from *SKF Magnetic Bearings*, real-time control via a dSpace digital signal processor, and custom-built PWM drive circuitry. The drive circuitry was built in collaboration with Bazooka Electronics (Edmonton, AB).

biasing and is termed *decentralized* because the four radial axes as well as the thrust axis are individually controlled by five single-input, single-output loops. The control laws are

$$\Delta i_x = k_p\, e_x + k_i \int_0^t e_x(\tau)\mathrm{d}\tau + k_d \frac{\mathrm{d}e_x}{\mathrm{d}t},$$
$$\Delta i_{i/o,y} = k_p\, e_{V_{i/o}} + k_i \int_0^t e_{V_{i/o}}(\tau)\mathrm{d}\tau + k_d \frac{\mathrm{d}e_{V_{i/o}}}{\mathrm{d}t},$$
$$\Delta i_{i/o,z} = k_p\, e_{W_{i/o}} + k_i \int_0^t e_{W_{i/o}}(\tau)\mathrm{d}\tau + k_d \frac{\mathrm{d}e_{W_{i/o}}}{\mathrm{d}t},$$

for error signals $(e_x, e_{V_{i/o}}, e_{W_{i/o}}) = (x_r - x, V_{13/24_r} - V_{13/24}, W_{13/24_r} - W_{13/24})$ and setpoints $(x_r, V_{13/24_r}, W_{13/24_r})$. By construction, decentralized PID is a setpoint stabilizing controller. This is in contrast to the flatness-based designs which permit asymptotic tracking of time-varying reference trajectories.

2.5 Experimental implementation

The *MBRotor* test stand is integrated into a laboratory setup consisting of custom-built drive circuitry and real-time digital control hardware. The control laws as well as inner-loop current tracking are managed by dSpace digital control hardware. The dSpace system is modular with a PowerPC board performing real-time computations at 10 kHz. Three high-speed ADC boards sample ten coil currents and five rotor displacements. An encoder board measures shaft speed via a Hall-Effect sensor. A digital waveform output board generates pulse width modulation (PWM) voltage waveforms for the drive circuitry.

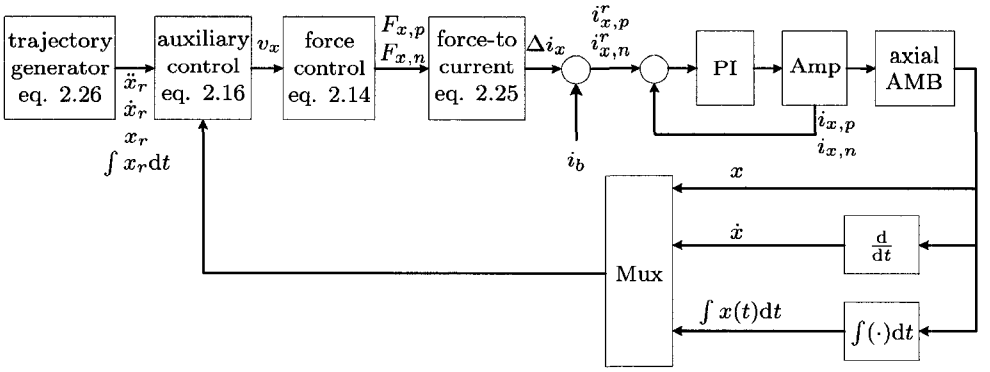

Figure 2.6: Block diagram of the closed-loop axial subsystem employing the constant-current-sum-based nonlinear tracking controller.

Each AMB coil is driven by an H-bridge delivering a maximum of 3 A output current at 48 V. The switching frequency of the PWM amplifiers is 10 kHz. The electronics integrate LEM Hall-Effect sensors for current feedback and tunable analog filters to provide signal anti-aliasing [20]. The electronics are pictured in Figure 2.5(b). Current control is implemented by means of proportional-integral (PI) feedback to obtain a current tracking bandwidth of approximately 400 Hz. This value is over two times lower than the bandwidth of typical servoamplifiers which drive the AMBs and is due to the relatively low PWM switching frequency.

The software development platform utilizes the Matlab/Simulink environment and has the ability to generate real-time code for the dSpace target. The control laws are discretized using an Euler approximation and coded into an S-function using the C programming language. Differentiation (to obtain velocities) and integration were performed numerically, with differentiation being lowpass filtered.

Figure 2.6 is a block diagram of the AMB under closed-loop control using the CCS-based nonlinear design. Note that in Figure 2.6 the reference currents $i^r_{x,p}, i^r_{x,n}$ are introduced as inputs to the inner PI loop.

2.6 Experimental results

2.6.1 Unbalance response

Although this Chapter's primary focus is on control of a non-rotating shaft, we momentarily diverge to consider rotational aspects in this section. The reason is that, in addition to motion tracking, the nonlinear control laws need to be robust to disturbances. Evaluating

the *unbalance response*, i.e. the rotational stabilization performance over a range of shaft speeds, is a practical assessment of each control system's robustness to the periodic disturbance induced by rotation of the shaft. The decentralized PID control law is a natural basis for comparison in this regard.

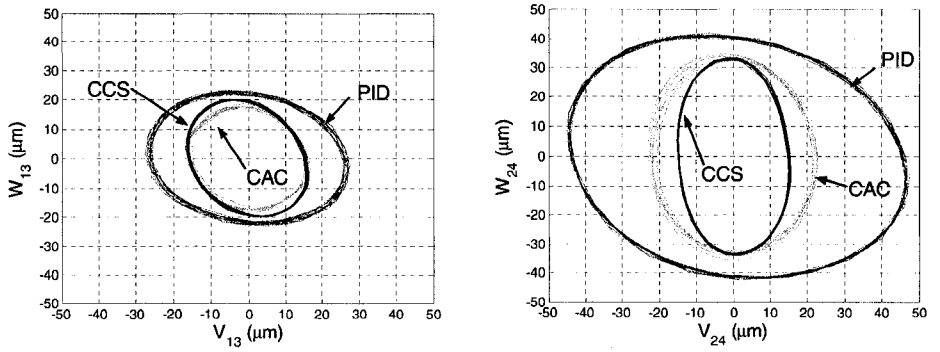

(a) inboard orbital

(b) outboard orbital

Figure 2.7: Unbalance response of three control laws (decentralized PID, flatness with CCS, flatness with CAC) with the shaft rotating at 14,000 r/min.

Figure 2.7 plots the orbits of the shaft as seen from the inboard and outboard measurement planes. The speed of rotation is $\omega/(2\pi) = 233$ Hz (approximately 14,000 r/min). For all three control laws, the feedback gains are tuned to achieve comparable performance. From experimentation, the existence of two shaft resonances was apparent. The resonance frequencies were approximately 650 Hz and 1240 Hz and required the addition of notch filters to the control law.

When evaluating the unbalance response of each control over a wide range of shaft speeds, gain selection has a strong bearing on performance. In all cases, the gains are synthesized using the pole-placement method. Since three poles are required to be placed for each control law, it is assumed that one pole lies on the negative real axis, and is small in magnitude (< 1) to avoid excessive integral gains (k_3 and k_i). Placement of the remaining two poles is based on achieving a sufficiently high stiffness (via k_1 and k_p) and damping (via k_2 and k_d) without introducing excessive noise into the feedback loop. Tuning plays a significant role here since the feasible pole locations are much more limited in practice than in theory. The reason for this is that excessive damping gains excite resonances to the point that they cannot be damped by the notch filters. At the same time, we wish to maximize the damping gains because they are most influential with respect to reducing the magnitude of the shaft's lateral vibrations.

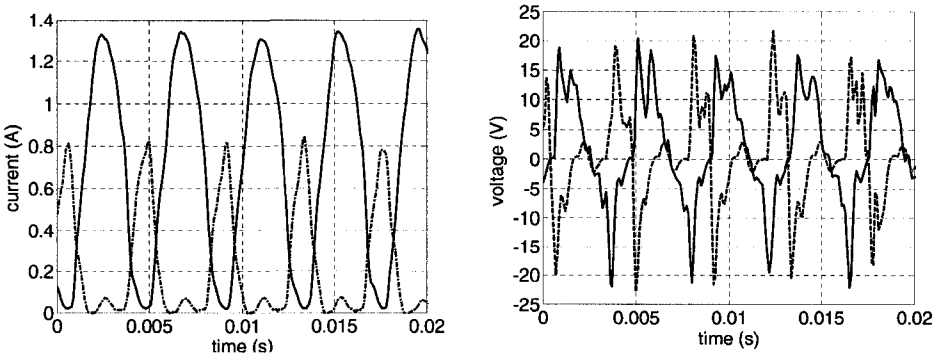

(a) flatness with CAC, currents

(b) flatness with CAC, voltages

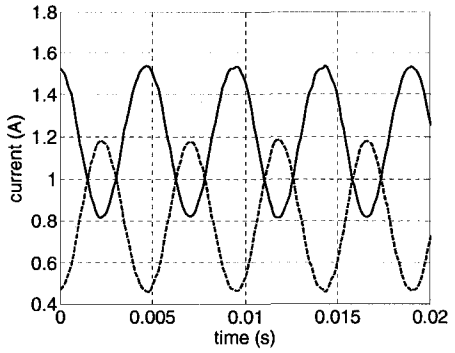

(c) flatness with CCS, currents

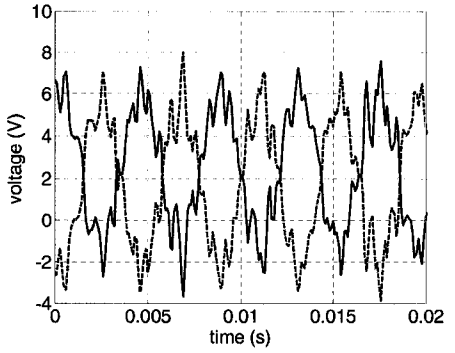

(d) flatness with CCS, voltages

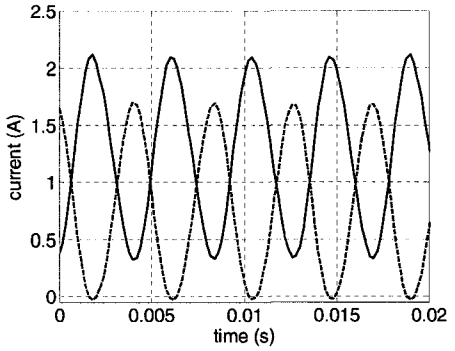

(e) decentralized PID, currents

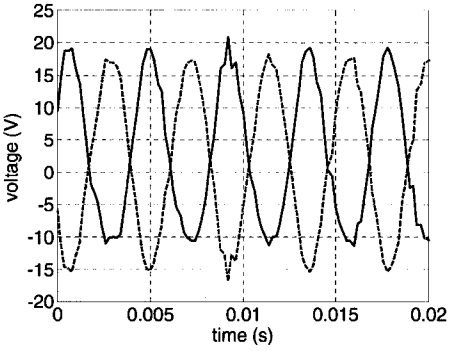

(f) decentralized PID, voltages

Figure 2.8: Outboard z-axis currents $i_{o,z,p}$ (dashed line) , $i_{o,z,n}$ (solid line) and voltages $u_{o,z,p}$ (dashed line), $u_{o,z,n}$ (solid line) associated with the unbalance response shown in Figure 2.7.

All three controllers can be tuned so that they can stabilize the rotation of the shaft beyond the system's specified range of rotational speed. This is not surprising for the decentralized PID control approach since it has been widely implemented [11]. However, the results in Figure 2.7 are encouraging because they show that the design of tracking controllers, and in particular the low-bias design, can also satisfy the basic stabilization requirement. The gains are presented in Table 2.4 for reference along with the values for i_b and η.

	k_2 [s^{-1}]	k_1 [s^{-2}]	k_0 [s^{-3}]	η [N]
nonlinear, CAC	250	$1.5 \cdot 10^5$	10^5	0.1
	k_2 [s^{-1}]	k_1 [s^{-2}]	k_0 [s^{-3}]	i_b [A]
nonlinear, CCS	300	$1.5 \cdot 10^5$	10^5	1.0
	k_p [A/m]	k_i [A-s/m]	k_d [A/(m-s)]	i_b [A]
linear, PID	$8 \cdot 10^3$	10^4	13	1.0

Table 2.4: feedback gains and bias parameters for each of the three controllers under comparison. CAC is "current almost complementary", CCS is "constant current sum", and PID is "proportional-plus-integral-plus-derivative."

Figure 2.8 shows representative current and voltage data of each controller at $14,000$ r/min. We remark that when performance variation from repeated experimentation is taken into account, none of the three control designs performs significantly better than the others in terms of the maximum obtainable shaft speed. Obtaining higher shaft speeds depends largely on improved balancing of the rotor assembly. For the experiments, no off-line techniques are applied to precision balance the shaft assembly. Doing so would result in smaller shaft orbitals and reduced control effort.

The CAC control currents shown in Figure 2.8(a) validate the feasibility of low-bias operation which leads to reduced ohmic losses and rotor heating. This is in contrast to the control currents associated with the other control laws, shown in Figure 2.8(c) and Figure 2.8(e), which operate about a 1 A bias. The soft switching condition associated with the CAC inversion does, however, place higher demands on the servoamplifiers. For example, it is evident that increasing shaft speeds lead to noticeable degradation in the inner-loop current tracking. As observed from Figure 2.8(a), $i_{o,z,n}$ does not decay to 0 A during its off cycle. The requirements for higher bandwidth current tracking from the inner-loops translates into an increase in the peak voltage requirements, as is shown by comparing Figure 2.8(b) to Figure 2.8(d). In fact, the voltage saturation level is potentially the limiting factor in the achievable performance of the CAC design. We demonstrate this in an

experimental scenario where the voltage saturation level is set to 12 V instead of 48 V. Figure 2.9 shows the unbalance response of the CAC controller as the shaft speed approaches 5,000 r/min. Although Figures 2.9(d)-2.9(e) make it clear that some voltage saturation can be tolerated, Figure 2.8(f) ultimately shows that instability arises due to current, and hence force, slew-rate limiting.

2.6.2 Motion tracking of a non-rotating shaft

Figures 2.10 and 2.11 show the tracking performance of the nonlinear and PID controllers for a time-varying reference trajectory. A 10 Hz elliptical reference trajectory is chosen for the shaft, that is

$$y_r(t) = 50\sin(20\pi t)\ \mu\text{m}, \tag{2.26a}$$

$$z_r(t) = 80\cos(20\pi t)\ \mu\text{m}, \tag{2.26b}$$

$$x_r(t) = \theta_r(t) = \psi_r(t) = 0\ \mu\text{m}. \tag{2.26c}$$

The constraints on motion planning for the shaft involve avoiding the singularity in the force relation (2.4) at $\xi = \pm\kappa$ and ensuring the reference currents are within the saturation bounds of 0 A (lower) and 2 A (upper). It can be easily verified that (2.26) satisfy these constraints.

Figure 2.10 shows the tracking performance of the CCS-based nonlinear control law. This result is almost identical to that of the CAC-based control law and so only a representative set of results is shown. The tracking error in x, y, z is ± 3 μm and the angles ψ, θ are stabilized to within ± 45 μrads. Design of the gains associated with the error dynamics does impact the tracking performance, both in the convergence rate of the tracking error as well as robustness to modeling error. As discussed in the previous section, gain selection is primarily limited by noise considerations which is an unmodeled effect, so a model-based gain synthesis procedure, e.g. based on tracking performance as measured by some cost function, does not appear to be particularly helpful here.

We remark that tracking performance of the flatness-based controllers is independent of the choice of actuator condition, i.e. CCS or CAC, provided sufficient voltage head room exists. Figure 2.12 shows the different control currents associated with each nonlinear control law. Interestingly, in the absence of disturbances the CAC controller only requires the upper radial bearing coils to be energized.

The tracking performance of the PID controller is presented in Figure 2.11. Decentralized reference trajectories are generated using transformation (2.17). The results confirm

in practice that a setpoint-stabilizing control law leads to inferior tracking of sufficiently fast-varying trajectories. The shaft overshoots its y- and z-coordinate reference trajectories resulting in tracking errors in excess of 20 μm. Physical contact with the touchdown bearings is also a result. This contact accounts for the distortion of ψ and θ. A significant performance improvement cannot be obtained from tuning the PID gains.

2.7 Conclusion

This chapter has presented an experimental study of nonlinear tracking control with and without bias currents. Both nonlinear designs are shown to be sufficient to stabilize a rotating shaft over its specified range of speed as well as accurately track time-varying reference trajectories. Avoiding coil premagnetization, through either a hard or soft switching condition, is shown to place higher demands on the servoamplifers.

The next chapter combines our previous study of stabilizing a rotating shaft and tracking the trajectory of a non-rotating shaft. That is, we consider trajectory tracking of a rotating shaft which introduces an addition modeling and control challenge associated with the induced harmonic disturbances associated with mass unbalance.

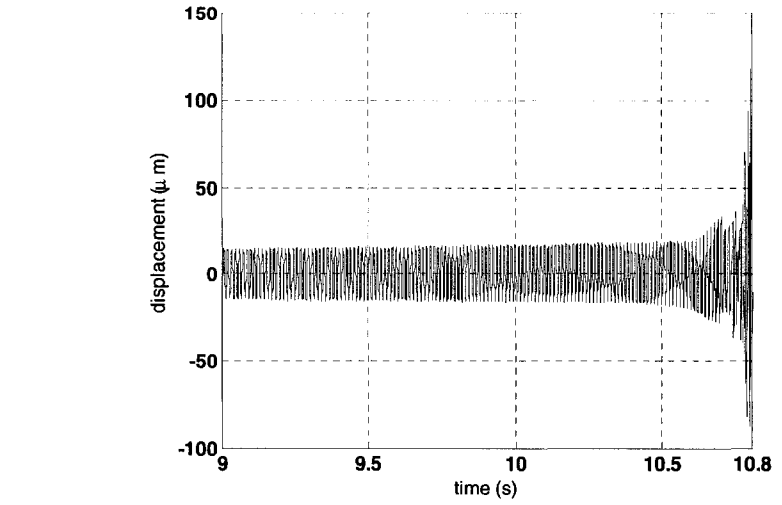

(a) y

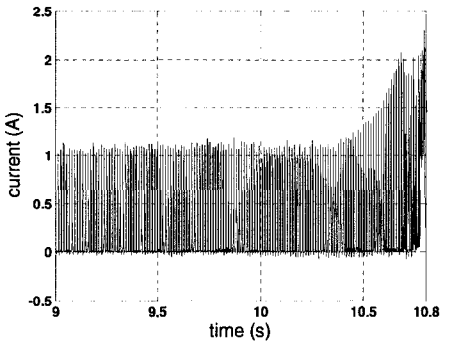

(b) $i_{o,y,p}$

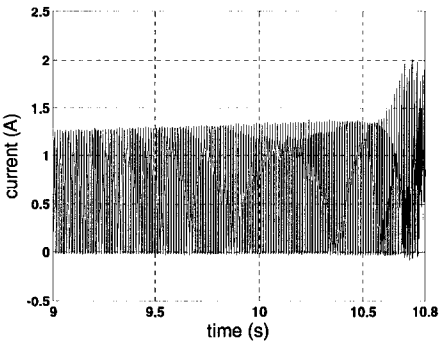

(c) $i_{o,y,n}$

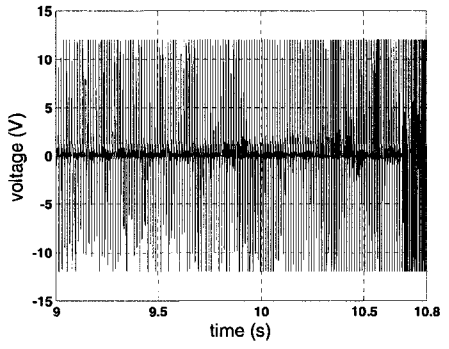

(d) $u_{o,y,p}$

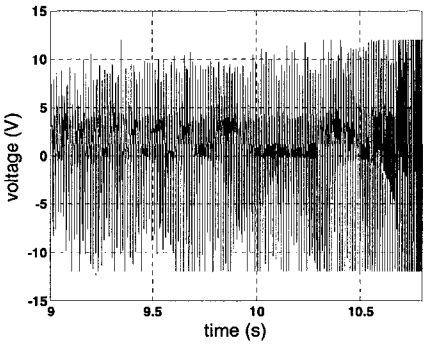

(e) $u_{o,y,n}$

Figure 2.9: Destabilization of the AMB system (as indicated by divergence of y in (a)) as the shaft speed is increased to $5,000$ r/min using the CAC controller with saturating voltage of 12 V.

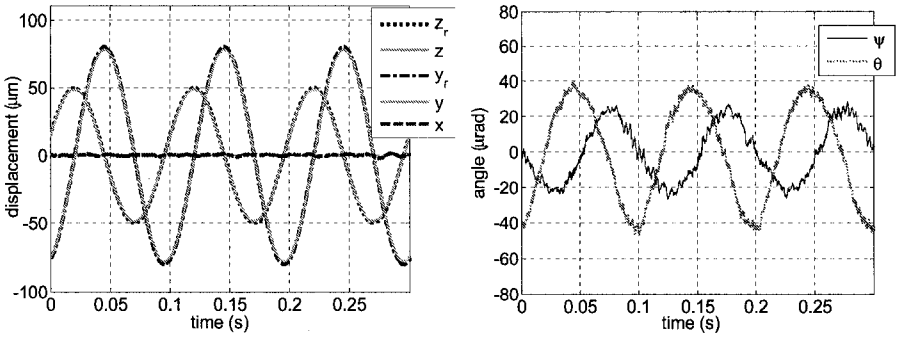

(a) x, y, z (b) ψ, θ

Figure 2.10: Trajectory tracking performance for the CCS-based nonlinear controller.

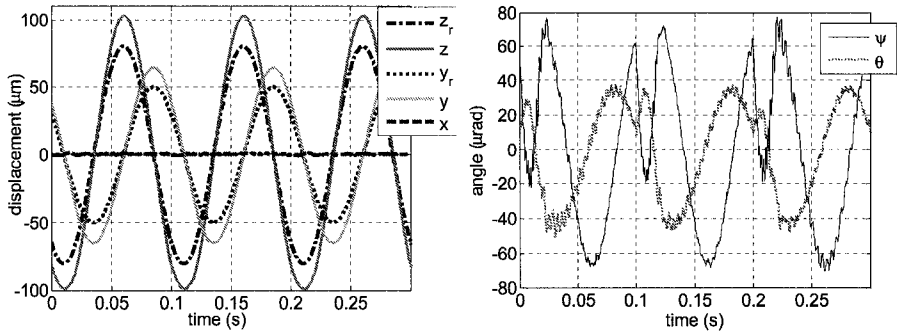

(a) x, y, z (b) ψ, θ

Figure 2.11: Trajectory tracking performance for the decentralized PID controller.

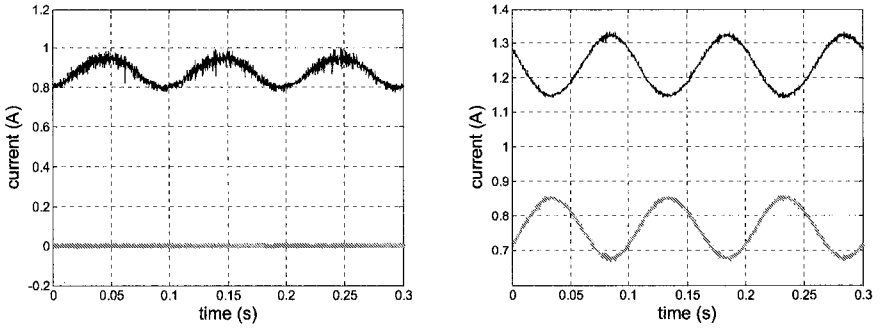

(a) flatness-based CAC (b) flatness-based CCS

Figure 2.12: Inboard y-axis currents $i_{i,y,p}$ (grey line) and $i_{i,y,n}$ (black line) for each nonlinear controller associated with the trajectory tracking shown in Figure 2.10. Whereas the CCS-based controller has opposing electromagnets energized, the CAC-based controller only requires the upper electromagnets to be energized.

Chapter 3

Trajectory Tracking of a Rotating Shaft with Active Magnetic Bearings

We extend the work in the previous chapter to consider trajectory tracking of a rotating shaft. The key challenge raised by a rotating shaft is that of synchronous vibration suppression. We explore state estimation techniques as the basis for a solution.

3.1 Introduction

Many applications of active magnetic bearings (AMBs) require only setpoint stabilization through the use of linear, decentralized control techniques. Advanced control strategies, however, can extend the precision, efficiency and range of operation of AMBs thereby increasing their industrial acceptance and range of application. Perhaps the most impacting control technology for AMBs has been that which suppresses synchronous vibration associated with the rotating shaft. Vibration control has the ability to reduce reactive power consumption, thus improving efficiency, and isolates rotor vibration from the support structure [8]. Another interesting avenue that has been explored with AMBs is the possibility of the rotating shaft tracking a prescribed orbit over the air gap. This idea is motivated by the potential of a machining spindle to perform non-circular boring [131, 27, 28], refer back to Figure 1.4 for an example. Moreover, the problem of trajectory tracking is a fundamentally interesting one because system nonlinearity becomes a matter of concern and synchronous vibration control is needed to obtain sufficient accuracy. Building on the results from Chapter 2, we develop a control strategy in this chapter for trajectory tracking of a rotating shaft.

Synchronous vibration results from rotation of an unbalanced shaft. That is, centrifugal forces synchronous with the speed of rotation act on the shaft due to misalignment of iner-

tial and geometric axes. A mechanically well-balanced shaft can minimize, but not eliminate, synchronous vibration from the outset. As a result, active vibration control (AVC) through AMBs has been an established area of research and two outcomes are possible. One outcome of AVC leads to the shaft rotating about its inertial axis. *Synchronous current reduction*, as it is called, isolates the shaft's vibration from the support structure (i.e. the AMB stators). The other possible outcome of AVC is forced rotation about the geometric axis, known as *synchronous position reduction*. This outcome minimizes the rotor vibration by superimposing synchronous bearing forces to cancel the unbalance forces. Existing approaches to AVC using AMBs include notch filtering [51], disturbance observer-based compensation [52, 105], adaptive feedback [74], and adaptive feedforward [112, 8]. A survey of AVC is in [134].

Trajectory tracking requires synchronous position reduction because we are concerned with the accuracy with which we can position the shaft's geometric axis. In an application context, the tool geometry is designed with respect to the geometric axis of the machining spindle and so it is unacceptable to allow rotation about its inertial axis. As such, it is the goal of this chapter to integrate synchronous position reduction into the flatness-based control developed in Chapter 2. Within our framework of nonlinear state feedback, the natural AVC approach is disturbance estimation and cancelation. We treat synchronous vibration as a harmonic disturbance and design a state observer to estimate it. The resulting disturbance observer is model-based, and therefore it can easily incorporate system nonlinearity and does not rely on any sort of "learning" process such as methods based on influence coefficients [64]. An additional advantage of a disturbance observer is that multiple types of disturbances can be simultaneously estimated. Of particular importance is constant disturbance estimation, which we show to be an effective alternative to integral control to counteract steady state positioning error.

Disturbance observers have been considered previously and incorporated into a number of AMB controllers. For instance, work in [52] incorporates harmonic disturbance estimation and cancelation through linear, estimated state feedback and applied it to a 4DOF system. A sliding mode observer in [104] estimates harmonic disturbances based on a linearized vertical shaft system. Work in [135] considered harmonic disturbance estimation in the time-varying rotor speed case, leading to a linear time-varying observer design. Constant and harmonic disturbances are estimated in a nonlinear observer in [131]. The nonlinear observer is part of a trajectory tracking controller and is shown to be effective on a five degree-of-freedom (5DOF) system.

Disturbance observers tend to be limiting in two respects. First, the order of AMB state observers that incorporate disturbance estimation can become very high, for example ranging from fifth- to tenth-order in [131]. In such cases, selection of the observer gains may become non-obvious, and scheduling of the gains may be necessary to account for rotor-speed dependence. The second limitation is the assumption of constant rotor speed in the disturbance observer model. Practical AMB systems operate in stages where constant speed is not the case, e.g. between start-up levitation and the operating speed, and harmonic disturbance cancelation is sensitive in that it can only be applied once disturbance estimates have been converged at the desired operating speed. This fact suggest a modular approach to disturbance estimation and compensation. As such, the innovation in our design lies in a hierarchical scheme involving a reduced-order disturbance observer which assumes position and velocity are available. Then we design an inner-loop velocity observer with error dynamics that converge at a sufficiently faster rate than those of the disturbance observer. The justification behind this approach is based on a high-gain argument [58, 37]. Lower-dimension state observers result, where gain selection can be related to pole locations in a straightforward manner. Completely modular AVC is the other result, making our approach practical.

We emphasize experimental validation of the proposed control design. Although disturbance estimation-based synchronous position reduction has been studied for quite some time, efforts to assess the feasibility of this method on practical systems and at realistic shaft speeds are limited. Previous results are either limited to simulation [80, 104, 135] or are demonstrated experimentally at (relatively) low shaft speeds [52]. Integration of the method into a trajectory tracking control design has only been previously considered in [131].

Our approach to disturbance-observer-based synchronous position reduction is shown to be effective over the full range of shaft speed of our 5DOF test stand. Furthermore, constant disturbance estimation and cancelation is shown to be an effective alternative to integral control. By canceling these disturbances, we show that trajectory tracking is possible over a wider range of the available gap. The latter result is demonstrated at the maximum specified shaft speed of the test stand supporting a shaft with significant unbalance.

3.2 Mathematical model

Maintaining a rigid body assumption on the shaft assembly, we now consider the dynamic model

$$m\ddot{x} = F_x, \tag{3.1a}$$

$$m\ddot{y} = F_{o,y} + F_{i,y} + F_{c,y} + mg_y + D_{c,y} + D_{h,y}, \tag{3.1b}$$

$$m\ddot{z} = F_{o,z} + F_{i,z} + F_{c,z} + mg_z + D_{c,z} + D_{h,z}, \tag{3.1c}$$

$$J\ddot{\psi} = -(l_{o,a} - x)F_{o,z} + (l_{i,a} + x)F_{i,z} - J_x\omega\dot{\theta} + l_cF_{c,z} + \tau_{c,\psi} + \tau_{h,\psi}, \tag{3.1d}$$

$$J\ddot{\theta} = (l_{o,a} - x)F_{o,y} - (l_{i,a} + x)F_{i,y} + J_x\omega\dot{\psi} - l_cF_{c,y} + \tau_{c,\theta} + \tau_{h,\theta}, \tag{3.1e}$$

and recall the spring forces given by

$$F_{c,y} = -K(y - l_c\theta),$$

$$F_{c,z} = -K(z + l_c\psi),$$

and AMB forces given by

$$\begin{aligned} F_x &= F_{x,p} - F_{x,n} \\ &= \frac{\beta_x i_{x,p}^2}{(\kappa_x - x)^2} - \frac{\beta_x i_{x,n}^2}{(\kappa_x + x)^2}, \end{aligned} \tag{3.2a}$$

$$\begin{aligned} F_{i/o,y/z} &= F_{i/o,y/z,p} - F_{i/o,y/z,n} \\ &= \frac{\beta i_{i/o,y/z,p}^2}{(\kappa - \xi_{i/o,y/z})^2} - \frac{\beta i_{i/o,y/z,n}^2}{(\kappa + \xi_{i/o,y/z})^2}. \end{aligned} \tag{3.2b}$$

Model (3.1) results from augmenting the model (2.3) from Chapter 2 to account for mass unbalance which results from shaft rotation. For a rigid rotor, the principle of mass unbalance and unbalance force generation can be understood with the help of Figure 3.1. Figure 3.1 shows a planar rotor in a stationary $x - y$ frame. The rotor has a static mass unbalance represented by a point mass m_p at a radius of ν. The point mass is rotating at the angular speed of the shaft ω. The radial unbalance forces along the x and y axes are given by

$$F_x = m_p\nu\omega^2\cos(\omega t), \tag{3.3a}$$

$$F_y = m_p\nu\omega^2\sin(\omega t). \tag{3.3b}$$

The unbalance forces (3.3) are synchronized to the shaft rotation and lead to synchronous vibration. In the three-dimensional rigid rotor case, dynamic unbalance results which means that the rotor's principle axis (going through its center of mass) is misaligned with the

rotor's geometric axis. Reference [74] provides a graphical description of a dynamically unbalanced rotor.

Because mass unbalance generates sinusoidal forces, we can model these forces as an exogenous, harmonic disturbance in each degree of freedom. The harmonic disturbances are denoted as forces $D_{h,y/z}$ in the y and z coordinates, and as torques $\tau_{h,\psi/\theta}$ in the ψ and θ coordinates. Mass unbalance is assumed to have a negligible impact along the x-axis. The disturbances are modeled by

$$\ddot{D}_{h,y/z} = -\omega^2 D_{h,y/z},$$
$$\ddot{\tau}_{h,\psi/\theta} = -\omega^2 \tau_{h,\psi/\theta},$$

which have imaginary eigenvalues at the synchronous speed. In addition, constant disturbance forces $D_{c,y/z}$ and torques $\tau_{c,\psi/\theta}$ are added to the model with the trivial dynamics

$$\dot{D}_{c,y/z} = 0,$$
$$\dot{\tau}_{c,\psi/\theta} = 0,$$

to account for potential constant disturbances and model bias.

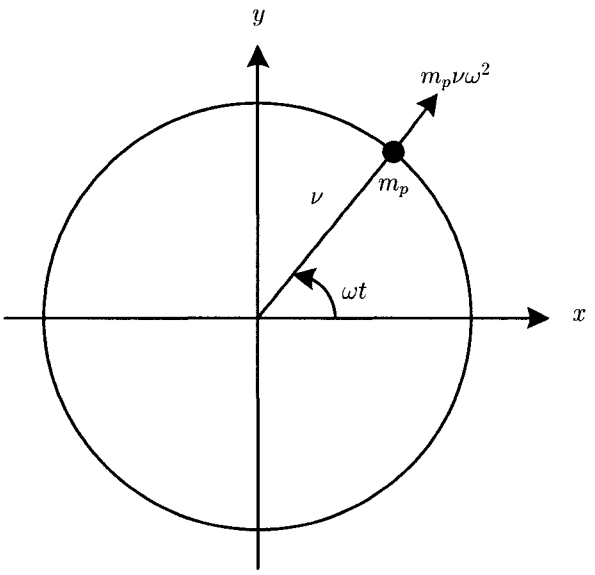

Figure 3.1: Mass unbalance of a planar rotor. A point mass m_p at a radius ν from the center of the rotor has a spin rate of ω. The arrow is the unbalance force vector.

3.3 Flatness-based trajectory tracking

With the addition of disturbance forces and torques, the model (3.1) remains differentially flat so that an asymptotic trajectory tracking control can be designed. For the flat output x, y, z, ψ, θ and input forces $F_x, F_{i/o,y/z}$, the feedback

$$F_x = m\eta_x, \tag{3.4a}$$

$$F_{i/o,y} = \frac{m(l_{o/i,a} \mp x)(\eta_y - g_y) \pm J_x\omega\dot{\psi} \mp J\eta_\theta - (l_{o/i,a} \mp x \pm l_c)F_{c,y}}{l_{o,a} + l_{i,a}} + F^{\text{dist}}_{i/o,y}, \tag{3.4b}$$

$$F_{i/o,z} = \frac{m(l_{o/i,a} \mp x)(\eta_z - g_z) \pm J_x\omega\dot{\theta} \pm J\eta_\psi - (l_{o/i,a} \mp x \pm l_c)F_{c,z}}{l_{o,a} + l_{i,a}} + F^{\text{dist}}_{i/o,z}, \tag{3.4c}$$

where $F^{\text{dist}}_{i/o,y}, F^{\text{dist}}_{i/o,z}$ are the disturbance compensating forces

$$F^{\text{dist}}_{i/o,y} = \frac{-(l_{o/i,a} \mp x)(D_{c,y} + D_{h,y}) \pm (\tau_{c,\theta} + \tau_{h,\theta})}{l_{i,a} + l_{o,a}},$$

$$F^{\text{dist}}_{i/o,z} = \frac{-(l_{o/i,a} \mp x)(D_{c,z} + D_{h,z}) \mp (\tau_{c,\psi} + \tau_{h,\psi})}{l_{i,a} + l_{o,a}},$$

once again give five linear controllable systems $\ddot{x} = \eta_x, \ddot{y} = \eta_y, \ddot{z} = \eta_z, \ddot{\psi} = \eta_\psi, \ddot{\theta} = \eta_\theta$, with $\eta_x, \eta_y, \eta_z, \eta_\psi, \eta_\theta$ representing auxiliary control variables. Auxiliary control laws similar to (2.16) (without the error integration term) are used to exponentially stabilize the tracking error dynamics.

The control currents are obtained from the force feedback (3.4) from inversion of the force model (3.2). Inversion is accomplished via CCS through (2.25), as explained in Chapter 2, Section 4.2. This approach provides acceptable dynamic performance while capturing the nonlinear position dependence in the force relation, increasing the control law's suitability over a wide range of shaft positioning.

3.4 Observer design

In Chapter 2, the flatness-based control laws are implemented such that velocity is estimated by lowpass-filtered differentiation and error integration is employed to eliminate steady state positioning error. In this section, we instead consider the use of state observers to estimate velocity as well as disturbances.

Local observability of the model (3.1) can be easily confirmed. When (3.1) is unforced and gravity is merged with the constant disturbance, then the dynamic equations become linear time-invariant. A straightforward application of the observability test of the 20^{th} order system (excluding the x-axis subsystem) shows that all state variables are observable

from measurement of the center of mass y, z, ψ, θ. To demonstrate observability via a slightly simplified analysis, consider the model (3.1) without spring force coupling. When the system is unforced, the y coordinate subsystem becomes uncoupled (this is effectively the 1DOF system equivalent) and is expressed by

$$\begin{bmatrix} \dot{y} \\ \ddot{y} \\ \dot{D}_{c,y} \\ \dot{D}_{h,y} \\ \ddot{D}_{h,y} \end{bmatrix} = \begin{bmatrix} 0 & 1 & 0 & 0 & 0 \\ 0 & 0 & \frac{1}{m} & \frac{1}{m} & 0 \\ 0 & 0 & 0 & 0 & 0 \\ 0 & 0 & 0 & 0 & 1 \\ 0 & 0 & 0 & -\omega^2 & 0 \end{bmatrix} \begin{bmatrix} y \\ \dot{y} \\ D_{c,y} \\ D_{h,y} \\ \dot{D}_{h,y} \end{bmatrix}. \tag{3.5}$$

Assuming that the output is y, the observability matrix associated with (3.5) is

$$\begin{bmatrix} 1 & 0 & 0 & 0 & 0 \\ 0 & 1 & 0 & 0 & 0 \\ 0 & 0 & \frac{1}{m} & \frac{1}{m} & 0 \\ 0 & 0 & 0 & 0 & \frac{1}{m} \\ 0 & 0 & 0 & -\frac{\omega^2}{m} & 0 \end{bmatrix}$$

which has full rank for $m, \omega \neq 0$. This simplified analysis, easily generalized to the 5DOF model, ensures that a full-order observer can be designed to estimate all state variables [131]. Nonlinear observers, specifically those with exact error linearization [66], for the model (3.1) would be fifth-order for each of the y and z coordinate subsystems, and tenth-order for the (ψ, θ) subsystem [130]. Alternatively, we propose reduced-order disturbance observers based on the availability of an additional state (velocity). Velocity is estimated by an inner-loop observer having a faster convergence rate. This hierarchical approach estimates the states of the fifth-order translational subsystems (y and z) with second and third-order observers. Likewise, the states of the tenth-order rotational subsystem (ψ, θ) are estimated with one fourth-order observer and two third-order observers.

3.4.1 Velocity observer

For the translational coordinates, we present the observer design only for the y-axis since the design for the x- and z-axes is completely analogous.

The simplified dynamics $m\ddot{y} = F_{o,y} + F_{i,y} + F_{c,y} + mg_y$ are the model basis for estimating the time derivative of y. We purposely ignore the existence of constant and harmonic disturbances and consider the implications after the fact. We define the acceleration $a_y(\Delta i_{i/o,y}, x, y, \theta) = (F_{o,y} + F_{i,y} + F_{c,y})/m + g_y$, which includes the nonlinearity of the bearing force relation and is completely a function of known quantities, i.e. input and output. The estimated displacement $\hat{y}$ and velocity $\hat{v}_y$ are obtained with the observer

$$\begin{bmatrix} \dot{\hat{y}} \\ \dot{\hat{v}}_y \end{bmatrix} = \begin{bmatrix} 0 & 1 \\ 0 & 0 \end{bmatrix} \begin{bmatrix} \hat{y} \\ \hat{v}_y \end{bmatrix} + \begin{bmatrix} 0 \\ 1 \end{bmatrix} a_y + \begin{bmatrix} \ell_1 \\ \ell_2 \end{bmatrix} (y - \hat{y}) \tag{3.6}$$

for output injection gains $\ell_1, \ell_2 > 0$. Following high-gain arguments [58, 37] we show that a sufficiently accurate estimate in the presence of bounded disturbances can be obtained. We define the estimation error vector as $\zeta = (y - \hat{y}, \dot{y} - \hat{v}_y)^T$ and the associated error dynamics are

$$\dot{\zeta} = \underbrace{\begin{bmatrix} -\ell_1 & 1 \\ -\ell_2 & 0 \end{bmatrix}}_{\bar{A}} \zeta + \underbrace{\begin{bmatrix} 0 \\ \frac{1}{m} \end{bmatrix}}_{\bar{B}} D_y, \tag{3.7}$$

where $D_y = D_{c,y} + D_{h,y}$ is the total disturbance, assumed to not exceed the force capacity of the AMBs. From the solution of (3.7) we have

$$\begin{aligned} \zeta(t) &= e^{\bar{A}t}\zeta(0) + \int_0^t e^{\bar{A}(t-\tau)}\bar{B}D_y(\tau)d\tau \\ &= V^{-1}(\lambda)e^{\Lambda t}V(\lambda)\zeta(0) + \int_0^t V^{-1}(\lambda)e^{\Lambda(t-\tau)}V(\lambda)\bar{B}D_y(\tau)d\tau \end{aligned} \tag{3.8}$$

In (3.8), $\bar{A}$ has been diagonalized by the *Vandermonde* matrix

$$V(\lambda) = \begin{bmatrix} \lambda_1 & 1 \\ \lambda_2 & 1 \end{bmatrix}$$

and $\Lambda = \text{diag}[\lambda_1, \lambda_2]$ where $\lambda_2 < \lambda_1 < 0$ are the freely assigned eigenvalues of $\bar{A}$. Taking the norm and computing an upper bound gives

$$\begin{aligned} \|\zeta(t)\| &\leqslant \|V^{-1}(\lambda)e^{\Lambda t}V(\lambda)\zeta(0)\| + \int_0^t \|V^{-1}(\lambda)e^{\Lambda(t-\tau)}V(\lambda)BD_y(\tau)\|d\tau \\ &\leqslant \|V^{-1}(\lambda)\| \left[e^{\lambda_1 t}\|V(\lambda)\zeta(0)\| + \frac{\sqrt{2}D_{\max}}{m|\lambda_1|}(1 - e^{\lambda_1 t}) \right]. \end{aligned}$$

We take the limit to obtain the bound on the asymptotic error

$$\lim_{t\to\infty} \|\zeta(t)\| \leqslant \frac{\sqrt{2}D_{\max}}{m|\lambda_1|}\|V^{-1}(\lambda)\|. \tag{3.9}$$

The error bound (3.9) can made arbitrarily small through through the choice of λ_1, λ_2. For example, $\lambda_1 = -w, \lambda_2 = -w^2, w > 0$ results in

$$\lim_{w\to\infty} \frac{\|V^{-1}(-w, -w^2)\|}{|-w|} = 0.$$

Turning our attention now to the angular coordinates, we consider the simplified dynamic model without disturbance,

$$\begin{aligned} J\ddot{\psi} &= (l_{i,a} + x)F_{i,z} - (l_{o,a} - x)F_{o,z} - J_x\omega\dot{\theta} + l_cF_{c,z}, \\ J\ddot{\theta} &= (l_{o,a} - x)F_{o,y} - (l_{i,a} + x)F_{i,y} + J_x\omega\dot{\psi} - l_cF_{c,y}. \end{aligned}$$

We define the angular accelerations

$$\alpha_\psi(\Delta i_{i/o,z}, x, z, \psi) = [(l_{i,a} + x)F_{i,z} - (l_{o,a} - x)F_{o,z} + l_c F_{c,z}]/J,$$
$$\alpha_\theta(\Delta i_{i/o,y}, x, y, \theta) = [(l_{o,a} - x)F_{o,y} - (l_{i,a} + x)F_{i,y} - l_c F_{c,y}]/J,$$

and estimate of the angles $\hat{\psi}, \hat{\theta}$ and angular velocities $\hat{v}_\psi, \hat{v}_\theta$ from the observer

$$\begin{bmatrix} \dot{\hat{\psi}} \\ \dot{\hat{v}}_\psi \\ \dot{\hat{\theta}} \\ \dot{\hat{v}}_\theta \end{bmatrix} = \begin{bmatrix} 0 & 1 & 0 & 0 \\ 0 & 0 & 0 & -\omega J_x/J \\ 0 & 0 & 0 & 1 \\ 0 & \omega J_x/J & 0 & 0 \end{bmatrix} \begin{bmatrix} \hat{\psi} \\ \hat{v}_\psi \\ \hat{\theta} \\ \hat{v}_\theta \end{bmatrix} + \begin{bmatrix} 0 \\ \alpha_\psi(\Delta i_{i/o,z}, x, z, \psi) \\ 0 \\ \alpha_\theta(\Delta i_{i/o,y}, x, y, \theta) \end{bmatrix} + \begin{bmatrix} \ell_{11} & \ell_{12} \\ \ell_{21} & \ell_{22} \\ \ell_{31} & \ell_{32} \\ \ell_{41} & \ell_{42} \end{bmatrix} \begin{bmatrix} \psi - \hat{\psi} \\ \theta - \hat{\theta} \end{bmatrix}. \tag{3.10}$$

The gains $\ell_{ij}, 1 \leqslant i \leqslant 4, 1 \leqslant j \leqslant 2$ can be chosen to place the eigenvalues of the error system in the open left-half complex plane. It can be shown, in a similar manner to that previously described, that the asymptotic estimation error can be made arbitrarily small in the presence of bounded disturbances. To demonstrate the effectiveness of the observer (3.6), Figure 3.2 compares the observed velocity $\hat{v}_y$ to a numerical differentiation of y at a shaft speed of $8,000$ r/min. Sufficient disturbance suppression is obtained from a very high observer gain by placing the poles of the error dynamics far into the left-half plane. In this example, the poles are -3500 and -4500. Nevertheless, it can be seen in Figure 3.2 that the observer readily filters out high frequency noise. These clean velocity estimates are important as excessive noise can excite resonant modes of the shaft assembly.

3.4.2 Disturbance observer

A reduced-order observer is constructed to obtain constant and harmonic disturbance estimates based on position and the estimate of velocity. For the y subsystem the observer is

$$\begin{bmatrix} \dot{\hat{D}}_{c,y} \\ \dot{\hat{D}}_{h,y} \\ \dot{\hat{D}}_{v,y} \end{bmatrix} = \begin{bmatrix} 0 & 0 & 0 \\ 0 & 0 & 1 \\ 0 & -\omega^2 & 0 \end{bmatrix} \begin{bmatrix} \hat{D}_{c,y} \\ \hat{D}_{h,y} \\ \hat{D}_{v,y} \end{bmatrix} + \begin{bmatrix} h_1 \\ h_2 \\ h_3 \end{bmatrix} (m\dot{\hat{v}}_y - ma_y(\Delta i_{i/o,y}, x, y, \theta) - \hat{D}_{c,y} - \hat{D}_{h,y}) \tag{3.11}$$

where $D_{v,y} = \dot{D}_{h,y}$ and $h_i, 1 \leqslant i \leqslant 3$ are observer gains. From the coordinate transformation

$$\begin{bmatrix} z_1 \\ z_2 \\ z_3 \end{bmatrix} = \begin{bmatrix} \hat{D}_{c,y} \\ \hat{D}_{h,y} \\ \hat{D}_{v,y} \end{bmatrix} - \begin{bmatrix} h_1 \\ h_2 \\ h_3 \end{bmatrix} m\hat{v}_y \tag{3.12}$$

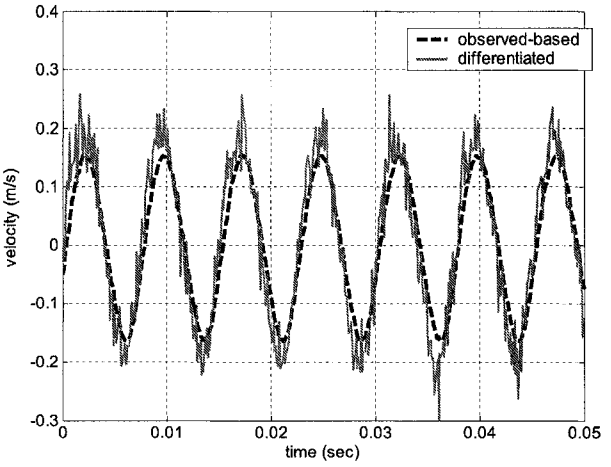

Figure 3.2: Comparison of observer-based and numerically differentiated estimates of velocity in the y-coordinate. Despite the observer's use of a high gain to suppress unmodeled disturbances, it still readily filters high frequency noise.

we obtained the reduced-order observer

$$\begin{aligned}
\begin{bmatrix} \dot{z}_1 \\ \dot{z}_2 \\ \dot{z}_3 \end{bmatrix} &= \begin{bmatrix} -h_1 & -h_1 & 0 \\ -h_2 & -h_2 & 1 \\ -h_3 & -(h_3+\omega^2) & 0 \end{bmatrix} \begin{bmatrix} z_1 \\ z_2 \\ z_3 \end{bmatrix} \\
&\quad - \begin{bmatrix} h_1^2 + h_1 h_2 & h_1 \\ h_1 h_2 + h_2^2 - h_3 & h_2 \\ h_1 h_3 + h_2(h_3+\omega^2) & h_3 \end{bmatrix} \begin{bmatrix} m\hat{v}_y \\ ma_y(\Delta i_{i/o,y}, x, y, \theta) \end{bmatrix}, \qquad (3.13) \\
\begin{bmatrix} \hat{D}_{c,y} \\ \hat{D}_{h,y} \end{bmatrix} &= \begin{bmatrix} z_1 \\ z_2 \end{bmatrix} + \begin{bmatrix} h_1 \\ h_2 \end{bmatrix} m\hat{v}_y.
\end{aligned}$$

Defining the estimation error vector as $(\tilde{D}_{c,y}, \tilde{D}_{h,y}, \tilde{D}_{v,y})^T = (D_{c,y} - \hat{D}_{c,y}, D_{h,y} - \hat{D}_{h,y}, D_{v,y} - \hat{D}_{v,y})^T$, the error dynamics are

$$\begin{bmatrix} \dot{\tilde{D}}_{c,y} \\ \dot{\tilde{D}}_{h,y} \\ \dot{\tilde{D}}_{v,y} \end{bmatrix} = \begin{bmatrix} 0 & 0 & 0 \\ 0 & 0 & 1 \\ 0 & -\omega^2 & 0 \end{bmatrix} \begin{bmatrix} \tilde{D}_{c,y} \\ \tilde{D}_{h,y} \\ \tilde{D}_{v,y} \end{bmatrix} - \begin{bmatrix} h_1 \\ h_2 \\ h_3 \end{bmatrix} (m\dot{\hat{v}}_y - ma_y(\Delta i_{i/o,y}, x, y, \theta) - \hat{D}_{c,y} - \hat{D}_{h,y}). \qquad (3.14)$$

Recognizing that $\dot{\hat{v}}_y = \dot{v}_y - \dot{\tilde{v}}_y$ and $m\dot{v}_y = ma_y + D_{c,y} + D_{h,y}$, (3.14) becomes

$$\begin{bmatrix} \dot{\tilde{D}}_{c,y} \\ \dot{\tilde{D}}_{h,y} \\ \dot{\tilde{D}}_{v,y} \end{bmatrix} = \begin{bmatrix} -h_1 & -h_1 & 0 \\ -h_2 & -h_2 & 1 \\ -h_3 & -(h_3+\omega^2) & 0 \end{bmatrix} \begin{bmatrix} \tilde{D}_{c,y} \\ \tilde{D}_{h,y} \\ \tilde{D}_{v,y} \end{bmatrix} + \begin{bmatrix} h_1 \\ h_2 \\ h_3 \end{bmatrix} m\dot{\tilde{v}}_y. \qquad (3.15)$$

From (3.15) it is apparent that the velocity estimation error $\tilde{v}_y$ enters the disturbance error system as a force $m\dot{\tilde{v}}_y$. To see the effect this has on disturbance estimates, we know from (3.7) that $\tilde{v}_y$, upon convergence, is a signal with a constant and harmonic component. We state it as $\tilde{v}_y(t) = \tilde{v}_{dc} + \tilde{v}_{ac}\sin(\omega t)$, where $\tilde{v}_{dc}$ is the DC component of the error and $\tilde{v}_{ac}$ is the amplitude of the AC component of the error. Hence $\dot{\tilde{v}}_y(t) = \omega\tilde{v}_{ac}\cos(\omega t)$. Next, consider the transfer matrix G with input $m\dot{\tilde{v}}_y$ and output $(\tilde{D}_{c,y}, \tilde{D}_{h,y})$. Calculating the magnitude of $G(s)$ at the synchronous frequency $s = j\omega$ gives $|G(j\omega)| = [0\ 1]^{\mathrm{T}}$, implying that $\lim_{t\to\infty}|\tilde{D}_{c,y}(t)| = 0$ and $\lim_{t\to\infty}|\tilde{D}_{h,y}(t)| \leqslant |m\omega\tilde{v}_{ac}|$. In other words, the estimation error of the constant disturbance converges to zero error whereas the estimation error of the harmonic disturbance has a bounded error. The error bound $|\tilde{D}_{h,y}(t)|$, being a function of $\tilde{v}_{ac}$, can be made arbitrarily small by the choice of eigenvalues for the velocity observer. However, this error degrades for higher values of ω and is a limiting factor in our design.

The disturbance observer structure is the same for all coordinates. For example, in the θ coordinate we replace $\hat{D}_{c,y}, \hat{D}_{h,y}, m\hat{v}_y, ma_y$ with $\hat{\tau}_{c,\psi}, \hat{\tau}_{h,\psi}, J\hat{v}_\theta, J\alpha_\theta + J_x\omega\hat{v}_\psi$ respectively in (3.13). Hence, disturbance estimates are decoupled for each coordinate. When the shaft speed changes, the observer gains can be efficiently re-computed. For a given ω and a desired characteristic polynomial $s^3 + \lambda_2 s^2 + \lambda_1 s + \lambda_0 = 0$ for the error dynamics (3.15), the gains are given by

$$h_1 = \frac{\lambda_0}{\omega^2}, \qquad h_2 = \lambda_2 - \frac{\lambda_0}{\omega^2}, \qquad h_3 = \lambda_1 - \omega^2, \qquad \omega \neq 0.$$

The hierarchical design of the velocity and disturbance observers is shown in the block diagram of the closed-loop system, Figure 3.3. The intended consequence is the modularity of disturbance estimation and compensation. That is, it is necessary that the velocity observer functions continuously to ensure stable levitation while the disturbance observer is intended only for constant-speed operation. This modularity avoids potentially complex calculations for observer gains as a function of rotor speed or the possible need to schedule the observer gain.

3.5 Experimental results

Experiments were performed to evaluate the performance of the proposed control scheme on a rotating shaft. We note that shaft unbalance is significant for these experiments since the shaft is manually assembled and no mechanical balancing has been performed.

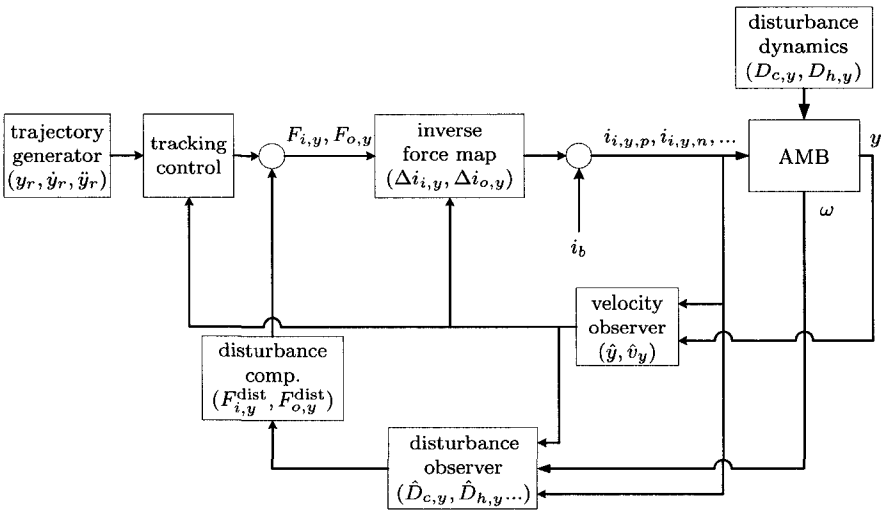

Figure 3.3: Schematic of the closed-loop system for the y coordinate.

Eigenvalues of the tracking error dynamics are placed at $-200 \pm 400i$. The eigenvalues of the disturbance observer are -55 and $-250 \pm 850i$. The placement of eigenvalues is done on an empirical basis, so as to avoid excessive actuator saturation and excessive noise.

The initial experimental results test the controller's ability to reject disturbances, and therefore reference trajectories are set to the system origin. Figure 3.4 shows coil currents and rotor displacements in the measurement planes during engagement of disturbance compensation for $\omega/(2\pi) = 167$ Hz (10,000 r/min). In less than 0.15 s of closing the loop, orbits of the radial bearing rotors show a major reduction in offset and vibration. In steady state the rotor measurements $V_{13}, V_{24}, W_{13}, W_{24}$ are each constrained to an envelope of ± 1 μm about the origin. From Figures 3.4(e)-3.4(f) we observer spikes in the differential coil currents $\Delta i_{i/o,y/z}$, indicating the high initial forces necessary to compensate the harmonic disturbances. Following the transient, more efficient operation is apparent due to the reduction in the amplitude of the synchronous component of the coil currents.

Interestingly, the amount of harmonic disturbance attenuation does not necessarily worsen with increasing shaft speed. At the shaft speeds being considered in our experimentation, the shaft is undergoing bending (not considered in our model) and this leads to some unpredictability in the attenuation level. This is demonstrated in Figure 3.5(a) which provides outboard rotor vibration amplitudes over the system's range of shaft speed. A comparison of the synchronous vibration amplitude (i.e. peak displacement) is made with and without disturbance compensation. We see from these results that in the worst case there is greater than 90% reduction in synchronous vibration and at best greater than 95% reduction. Our

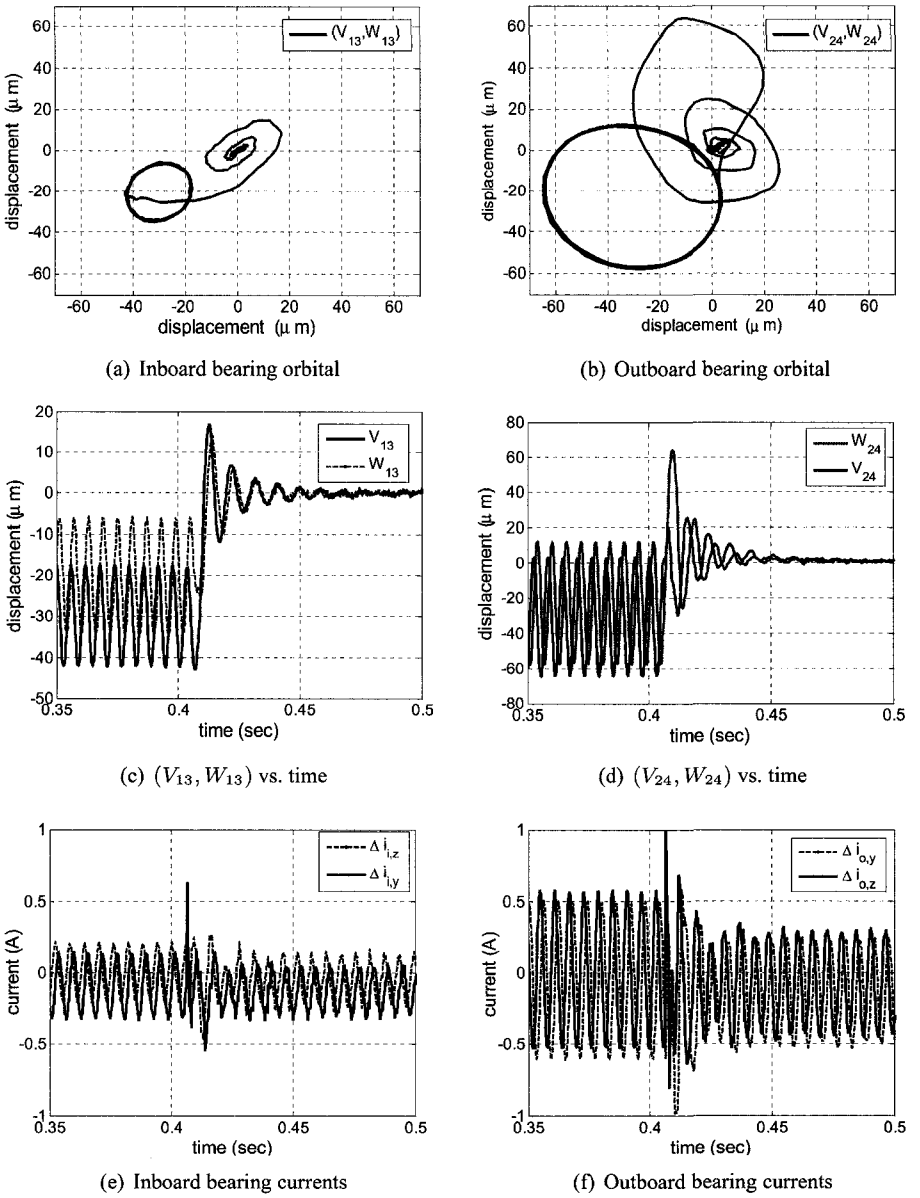

Figure 3.4: Constant and harmonic disturbance compensation at 10, 000 r/min. Asymptotic rejection of static offset occurs, as does significant attenuation of synchronous vibration. Attenuation of synchronous vibration is accompanied by a reduction in the synchronous component of the control currents.

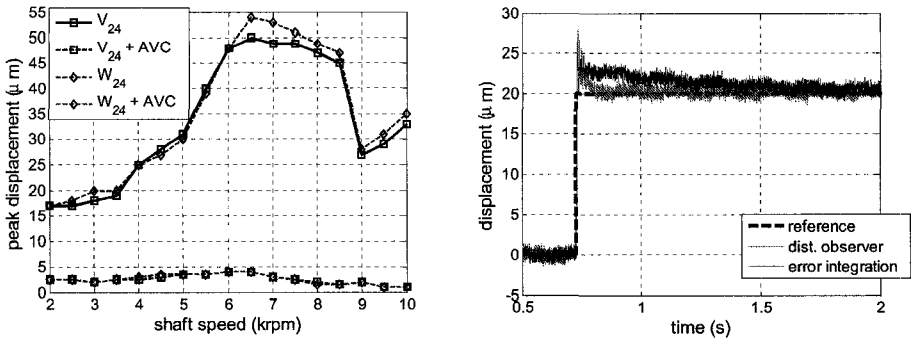

(a) Shaft speed vs. vibration amplitude

(b) V_{24} step response

Figure 3.5: Disturbance rejection performance in the outboard radial bearing.

observer-based synchronous position reduction scheme significantly improves our accuracy in positioning the shaft, and increases the bearing clearances within which to track trajectories.

We verify asymptotic constant disturbance rejection by comparison to the more common approach of integral control. Integral control can be implemented by utilizing the auxiliary control (2.15), i.e. $\eta_y = \ddot{y}_r - k_2(\dot{y} - \dot{y}_r) - k_1(y - y_r) - k_0 \int_0^t (y(\tau) - y_r(\tau))d\tau$. The comparison is based on step response data given in Figure 3.5(b). For this experiment, the shaft is rotating at 10,000 r/min with harmonic disturbance suppression and is commanded to track a 20 μm step along the z-axis. The integrator gain k_0 is obtained by placing the third pole of the tracking error dynamics at -0.015. The comparison in Figure 3.5(b) shows that percent overshoot, rise time, and peak time are similar for both tracking error integration and constant disturbance suppression. In fact, the settling time obtained by constant disturbance suppression (approximately 90 ms) is less than that obtained by error integration (greater than 1 s), although to say definitively whether one approach is better than another would require further investigation.

Trajectory tracking is demonstrated by transferring the center of mass c_m from the origin onto a 2 Hz elliptical orbit in 1 s. The corresponding trajectory is

$$y_r(t) = 90(r(t) - r(t-1))\sin(4\pi t)\ \mu\text{m}, \tag{3.16a}$$

$$z_r(t) = 40(r(t) - r(t-1))\cos(4\pi t)\ \mu\text{m}, \tag{3.16b}$$

$$x_r(t) = \theta_r(t) = \psi_r(t) = 0\ \mu\text{m}, \tag{3.16c}$$

where $r(t)$ is the unit ramp function. The tracking performance is shown in Figure 3.6 in the outboard measurement plane at 10,000 r/min. The orbital in Figure 3.6(a) as well as the

time series plot of V_{24} and W_{24} in Figure 3.6(b) show sufficiently good disturbance rejection to move the rotor over a large fraction of the available air gap (almost up to the system's positioning limits of 100 μm). The tracking error shown in Figure 3.6(c) is within ± 2.5 μm. The tracking error is mainly affect by how well the shaft angular displacements ψ, θ can be stabilized. The motor coupling is problematic in this regard, despite our attempt to cancel out its effect. The coupling's tendency is to tilt the shaft because it physically constrains the inboard end of the shaft. The result is that the shaft has a tendency to trace a cone instead of a cylinder, with a cylinder being commanded by the reference trajectories (3.16). Therefore, trajectory tracking at the synchronous speed, as is required by the particular application motivating this work, was not achieved with the same accuracy as shown in Figure 3.6. An AMB system with an inline motor, which is the configuration of industrial-grade 5DOF systems and shown in Figure 1.5, eliminates the need for a motor coupling and improved tracking accuracy would be expected.

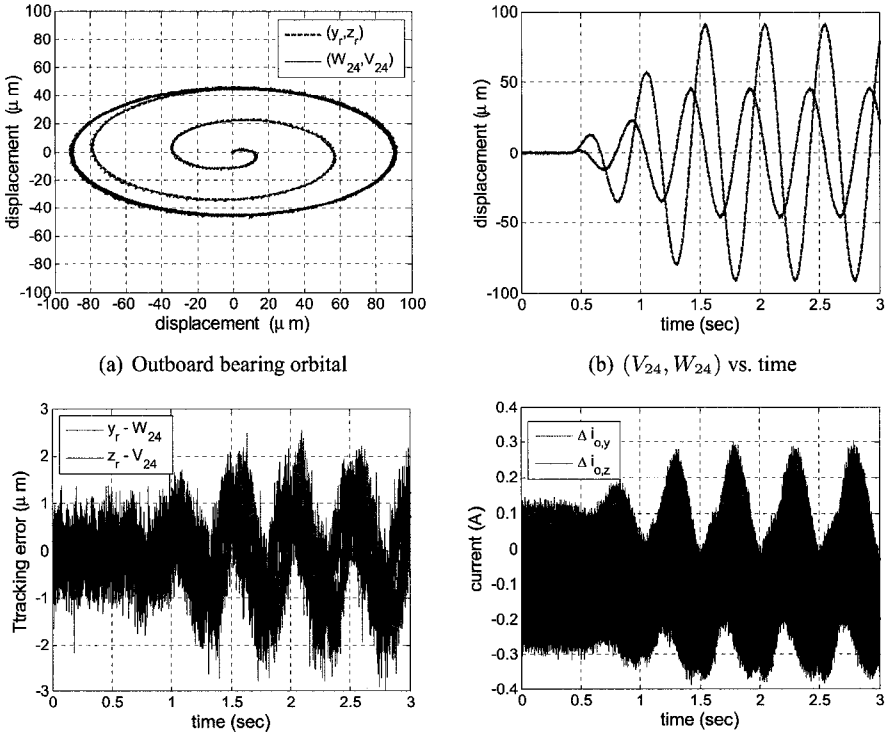

(a) Outboard bearing orbital

(b) (V_{24}, W_{24}) vs. time

(c) Tracking error

(d) Outboard bearing currents

Figure 3.6: Trajectory tracking at 10,000 r/min. The shaft's center of mass is tracking a 2 Hz ellipse.

A further difficulty with respect to the proposed motion tracking scheme is the assump-

tion of a rigid rotor. For sufficiently stiff shafts rotating at low enough speeds, a rigid body can be a good enough modeling assumption to achieve the control objectives, see [131] for tracking results for a shaft rotating at 4800 r/min. Bending of the shaft does occur at higher rotational speeds and this degrades our model accuracy. Extending trajectory tracking methodology to a model incorporating shaft flexibility poses new challenges and is a worthwhile future direction of research. A flexible shaft is a distributed parameter, i.e. infinitely dimensional, system that is typically approximated by a linear, lumped-parameter model of sufficiently high order. Obtaining such a model is a challenging task [111] and is beyond the scope of our modeling efforts in this thesis. From a force input, however, an AMB-supported flexible shaft is a linear controllable system and as such remains amenable to trajectory tracking. A particularly interesting example is in [71] which feedback linearizes a 1DOF AMB based on a rigid body model. Beam dynamics are incorporated as a transfer function in series with the resulting triple-integrator, i.e. feedback linearized, plant. Then, linear techniques are suitable to address the control objectives.

3.6 Conclusions

A nonlinear estimated state feedback control law is proposed in this chapter. The control strategy allows AMBs to guide a rotating shaft along a desired time-varying trajectory. The key ingredient in the design is a state observer scheme that estimates constant and harmonic disturbances. The observer scheme, due to its hierarchical construction, simplifies its implementation and remains effective at suppressing vibration and steady state error over a wide range of shaft speeds.

In the next chapter we consider an alternative state estimation scheme, specifically one that estimates velocity with a model-free algebraic approach instead of with an observer.

Chapter 4

Numerical Analysis of the Algebraic Derivative Method with Application to Active Magnetic Bearings

In this chapter we study an alternative to state estimation based on a signal differentiation method. We demonstrate its application to an active magnetic bearing (AMB), highlighting potential advantages over observer-based state estimation.

4.1 Introduction

Time derivative estimation of a measured signal has considerable importance in the area of control theory and practice. As an obvious example from the last two chapters, estimating velocity from position measurement is often necessary to implement state feedback. In Chapter 2 velocity was estimated by low-pass filtered differentiation whereas in Chapter 3 velocity was estimated by a simple nonlinear observer. Generally speaking, signal differentiation has the benefit of not requiring a model whereas an observer usually does. It is well-known, however, that signal differentiation techniques amplify noise which can be problematic in closed-loop, e.g. reduced precision and resonance excitation. In the general context of state estimation for nonlinear systems, much work has been done to merge the two approaches. For example, Diop et al. [26] introduce a new notion of observability for systems whose state x can be expressed as a function of input u, output y and a finite number of their time derivatives. Thus, nonlinear observer design amounts to determining the derivatives of y and u from available measurements in order to obtain a state estimate. References [26, 25] examine various numerical differentiation algorithms to realize such nonlinear observers from sampled data measurements. An interesting recent application to a sensorless motor drive can be found in [70]. In this work, speed is estimated through an

algebraic expression of stator voltages and currents and their successive derivatives with the derivatives obtained by numerical differentiation techniques. Recently in [128], a model-free, high-gain observer is proposed as a differentiator and the tradeoff between accuracy and noise amplification is examined. A least-squares polynomial approximation is another viable approach to derivative estimation which continues to receive attention [75].

For differentially flat nonlinear systems, previously discussed in Chapter 2, the state variables can be expressed algebraically in terms of a flat output and a finite number of its time derivatives. Therefore, estimation of successive time derivatives of the flat output leads to reconstruction of the state by algebraic formulae, thus giving these types of systems a special observability property [49]. The problem of computing successive time derivatives is addressed through the algebraic derivative (AD) method [35, 34]. The AD method is an analytic formulation yielding fast and non-asymptotic derivative estimates and avoids the requirements of knowing a system model or the statistical properties of the signal to be differentiated. Since its introduction, numerous applications and extensions of the AD method have been proposed. Work in [34] and [115] utilize AD to formulate nonlinear output feedback for tracking control of a DC motor pendulum and a synchronous generator, respectively. The effectiveness of the AD method with respect to noisy data, signal compression and detecting abrupt changes are treated in [30, 31]. The method's robustness to noise is formalized in [29]. A significant extension of the AD method is in unknown parameter identification and fault detection and isolation, see [55] and references therein.

The difficulty in applying the AD method is that it cannot provide continuously accurate estimates. The reason is that the method is based on a truncated Taylor series approximation of the signal to be differentiated. Hence, the approximation loses validity over time and a periodic resetting of the calculations is necessary. Various calculation resetting policies are studied in detail in [99] and an overlapping estimator algorithm is proposed in [98] to better preserve accuracy. In this chapter, we present a numerical analysis of the overlapping estimator implementation of the AD method. For our analysis, we restrict our attention to estimating a single time derivative.

As a case study, we integrate the AD method into the nonlinear control scheme of Chapter 3 and apply it to a 1DOF AMB. This is an interesting case study for two reasons. First, we can replace the high-gain velocity observer in our hierarchical scheme, explained in Chapter 3, Section 4, with derivative estimation via the AD method. Potentially, better performance can be realized by reducing our reliance on a simplified model. Second, the closed-loop bandwidth of AMB systems, as defined in a linear time invariant systems con-

text, is considerably higher than that of previous systems to which the AD method has been applied. Previous studied applications of the AD method include the unicycle, pendulum [34], synchronous generator [115], three-tank process [55] and chaotic systems [99, 98].

4.2 Algebraic differentiation

Our derivation of the AD method here follows that of [115] and [21]. We assume that an analytic signal $y(t)$ can be sufficiently approximated by its truncated Taylor series expansion about an initial time instant t_0, that is

$$\hat{y}(t) = \sum_{j=1}^{K} \frac{1}{(j-1)!} y^{(j-1)}(t_0)(t-t_0)^{j-1} 1(t-t_0) \tag{4.1}$$

where $1(t)$ is the unit step and positive integer K denotes the order of the truncation that determines the accuracy of the signal approximation. In the Laplace domain, (4.1) becomes

$$\left(s^K \hat{Y}(s) - \sum_{j=1}^{K} s^{K-j} y^{(j-1)}(t_0) \right) e^{-st_0} = 0, \tag{4.2}$$

where $\hat{Y}(s) = \mathcal{L}\{\hat{y}(t)\}$ is the Laplace transform of $\hat{y}(t)$. More formally, an Operational Calculus framework can be used [99]. Independent of unknown initial conditions, it is implied from (4.2) that

$$\frac{d^K}{ds^K}(s^K \hat{Y}(s)) = 0. \tag{4.3}$$

Applying Leibniz's rule for derivatives, i.e. the generalization of the product rule,

$$(fg)^{(K)} = \sum_{j=0}^{K} \binom{K}{j} f^{(K-j)} g^{(j)},$$

where f and g are K-times differentiable functions, we can re-express (4.3) as

$$\frac{d^K}{ds^K}(s^K \hat{Y}(s)) = \sum_{j=0}^{K} \frac{(K!)^2}{(j!)^2(K-j)!} s^j \frac{d^j}{ds^j} \hat{Y}(s).$$

Next, we consider the expression $s^{-(K-1)} \frac{d^K}{ds^K}(s^K \hat{Y}(s))$, which yields

$$\begin{aligned} 0 = & \left(\sum_{j=0}^{K-2} \frac{(K!)^2}{(j!)^2(K-j)!} s^{j-K+1} \frac{d^j}{ds^j} \hat{Y}(s) \right) + \frac{(K!)^2}{((K-1)!)^2} \frac{d^{K-1}}{ds^{K-1}} \hat{Y}(s) \\ & + s \frac{d^K}{ds^K} \hat{Y}(s). \end{aligned} \tag{4.4}$$

By applying the inverse Laplace transformation

$$\mathcal{L}^{-1}\left\{ \frac{1}{s^k} \left(\frac{d^j}{ds^j} \hat{Y}(s) \right) \right\} = \int^{(k)} (-t)^j y,$$

where we define the iterative integral

$$\int^{(k)}(-t)^j y = \int_0^t \int_0^{\sigma_1} \cdots \int_0^{\sigma_{k-1}} \sigma_k^j y(\sigma_k) d\sigma_k \ldots d\sigma_1,$$

equation (4.4) can be transformed back into the time domain. The result is

$$\begin{aligned} 0 = &\left(\sum_{j=0}^{K-2} \frac{(K!)^2}{(j!)^2(K-j)!} \int^{(K-j-1)}(-t)^j y \right) \\ &+ y\left(\frac{(K!)^2}{((K-1)!)^2}(-t)^{K-1} - K(-t)^{K-1} \right) + (-t)^K \frac{d}{dt} y. \end{aligned} \tag{4.5}$$

Thus, an estimate for the first time derivative $\dot{y}_e$ can be obtained by rearranging (4.5) to get

$$\begin{aligned} \dot{y}_e = &-\frac{1}{(-t)^K}\left(\sum_{j=0}^{K-2} \frac{(K!)^2}{(j!)^2(K-j)!} \int^{(K-j-1)}(-t)^j y \right) \\ &- \frac{y}{(-t)^K}\left(\frac{(K!)^2}{((K-1)!)^2}(-t)^{K-1} - K(-t)^{K-1} \right). \end{aligned} \tag{4.6}$$

In general, the equations $0 = s^{(-\alpha)} \frac{d^K}{ds^K}(s^K y(s))$, for $\alpha \leqslant K-1$ are the basis for computing derivatives of successive order. As such, (4.5) can be generalized to

$$\begin{aligned} 0 = &\left(\sum_{j=0}^{\alpha-1} \frac{(K!)^2}{(j!)^2(K-j)!} \int^{(K-j-1)}(-t)^j y \right) + \frac{(K!)^2}{(\alpha!)^2(K-\alpha)!}(-t)^\alpha y \\ &+ \left(\sum_{j=\alpha+1}^{K} \frac{(K!)^2}{(j!)^2(K-j)!} \left(\sum_{q=0}^{j-\alpha} \binom{j-\alpha}{q} (-1)^{j-\alpha-q}(-t)^{\alpha+q} \frac{j!}{(\alpha+q)!} y^{(q)} \right) \right). \end{aligned} \tag{4.7}$$

Rearranging terms for the derivatives in (4.7) gives

$$\begin{aligned} 0 = &\left(\sum_{j=0}^{\alpha-1} \frac{(K!)^2}{(j!)^2(K-j)!} \int^{(K-j-1)}(-t)^j y \right) + \frac{(K!)^2}{(\alpha!)^2(K-\alpha)!}(-t)^\alpha y \\ &+ \left(\sum_{q=0}^{K-\alpha} (-t)^{\alpha+q} y^{(q)} \left(\sum_{j=\alpha+1}^{K} \frac{(K!)^2}{(j!)(K-j)!(\alpha+q)!} \binom{j-\alpha}{q} (-1)^{j-\alpha-q} \right) \right) \end{aligned} \tag{4.8}$$

Rewriting (4.8) in the form

$$0 = \left(\sum_{n=0}^{\alpha-1} a_n \int^{(K-n-1)}(-t)^n y \right) + a_\alpha(-t)^\alpha y + \sum_{n=\alpha+1}^{K} a_n(-t)^n y^{(n-\alpha)}, \tag{4.9}$$

where

$$a_p = \begin{cases} \frac{(K!)^2}{(p!)^2(K-p)!}, & 0 \leqslant p \leqslant \alpha - 1 \\ \sum_{n=\alpha+q}^{K} \frac{(K!)^2}{n!(K-n)!(\alpha+q)!} \binom{n-\alpha}{q} (-1)^{n-\alpha-q}, & \alpha \leqslant p \leqslant K, \quad q = p - \alpha \end{cases} \tag{4.10}$$

we obtain expressions for successive time derivatives. For $\alpha = K-1$, we have from (4.9) the expression for the first derivative,

$$(-t)^K \dot{y}_e = -\left(\sum_{n=0}^{K-2} a_n \int^{(K-n-1)} (-t)^n y\right) + a_{K-1}(-t)^{K-1} y. \tag{4.11}$$

For $\alpha = K-2$ we get the expression for the second order time derivative

$$(-t)^K \ddot{y}_e = -\left(\sum_{n=0}^{K-3} a_n \int^{(K-n-1)} (-t)^n y\right) + a_{K-2}(-t)^{K-2} y + a_{K-1}(-t)^{K-1} \dot{y}, \tag{4.12}$$

which depends on the evaluation of the first order time derivative. Derivatives of third order and higher are similarly obtained by further decrementing α.

The resulting expressions admit a linear, time-varying filter with state equations

$$\dot{\eta} = \begin{bmatrix} 0 & 1 & 0 & \dots & 0 \\ 0 & 0 & 1 & \dots & 0 \\ \vdots & \vdots & \vdots & \ddots & \vdots \\ 0 & 0 & 0 & \dots & 1 \\ 0 & 0 & 0 & \dots & 0 \end{bmatrix} \eta + \begin{bmatrix} a_{1,K-2}(-t)^{K-2} \\ a_{1,K-3}(-t)^{K-3} \\ \vdots \\ a_{1,1}(-t) \\ a_{1,0} \end{bmatrix} y(t) \tag{4.13}$$

where $\eta \in {}^{K-1}$ are the state variables. The output equations are given by

$$\begin{aligned} -\begin{bmatrix} (-t)^K & 0 & 0 & \dots & 0 \\ (-t)^{K-1} a_{2,K-1} & (-t)^K & 0 & \dots & 0 \\ (-t)^{K-2} a_{3,K-2} & (-t)^{K-1} a_{3,K-1} & (-t)^K & \dots & 0 \\ \vdots & \vdots & & \ddots & \vdots \\ (-t)^{K-r+1} a_{r,K-r+1} & (-t)^{K-r+2} a_{r,K-r+2} & \dots & \dots & (-t)^K \end{bmatrix} \begin{bmatrix} \dot{y}_e \\ \ddot{y}_e \\ \vdots \\ y_e^{(r)} \end{bmatrix} \\ = \begin{bmatrix} a_{1,K-1}(-t)^{K-1} \\ a_{2,K-2}(-t)^{K-2} \\ \vdots \\ a_{r,K-r}(-t)^{K-r} \end{bmatrix} y(t) + \begin{bmatrix} \eta_1 \\ \eta_2 \\ \vdots \\ \eta_r \end{bmatrix} \end{aligned} \tag{4.14}$$

where $a_{r,p}$ corresponds to a_p with $\alpha = K-r$ for $r \leqslant K-1$. Therefore, we re-express (4.10) as

$$a_{r,p} = \begin{cases} \frac{(K!)^2}{(p!)^2(K-p)!}, & 0 \leqslant p \leqslant K-r-1 \\ \sum_{n=p}^{K} \frac{(K!)^2(n-K+r)!}{n!(K-n)!p!(p-K+r)!(n-p)!}, & K-r \leqslant p \leqslant K. \end{cases} \tag{4.15}$$

Due to the Taylor series approximation, the derivative estimate is only accurate over a finite time interval and loses validity as t becomes sufficiently larger than t_0. Therefore, at some later point in time t_r a resetting of the calculations is necessary whereby the filter calculations (4.13)-(4.14) become a function of the relative time $t - t_r$. An additional difficulty

with the AD method is that a calculation indetermination immediately follows a reset. As a result, there is a period $[t_r, t_r + \epsilon)$ of convergence during which the derivative estimate is inaccurate and temporary values must be adopted. Hence, we may assume a valid derivative estimate in the interval $t \in [t_r + \epsilon, t_r + t^*)$ where t^* denotes the interval length between resets. In summary, to preserve the estimation accuracy on a continual basis requires a reset policy as well as an extrapolation policy to temporarily estimate the derivative during the interim periods of convergence. We address each of these issues separately in the following sections.

4.2.1 Reset policy

It is perhaps most intuitive to reset the calculations at equidistant time intervals. This approach is taken in [34, 115]. Generally speaking, for a fixed truncation order K a reduction in the interval length t^* is necessary to accurately estimate signals of increasing bandwidth. However, no constructive method exists for choosing t^*, so one may have to resort to offline trial-and-error. Alternatively, a dynamic reset policy could be employed where the next reset time occurs when a cost function exceeds a prescribed threshold. Typically the cost function is based on the error between the actual and estimated signal, e.g. $e(t) = y(t) - \tilde{y}(t)$ where

$$\tilde{y}(t) = y(t_r^-) + \int_{t_r}^{t} \dot{y}_e(\tau)\mathrm{d}\tau.$$

Different cost functions, such as the absolute and integrated error, are studied and implemented in [99]. For a fixed threshold value, however, an absolute error criterion is non-robust to high-frequency perturbation and the integrated error criterion provides inconsistent performance for signals with significant bandwidth and amplitude variation. For instance, if we consider two identical signals with the exception of their scaling, their derivatives will be estimated with equal accuracy due to the linearity of the AD filter. However, the respective integrated errors would be different.

4.2.2 Extrapolation policy

The calculation indetermination immediately following a reset requires an extrapolation mechanism to estimate the derivative during the initial period of convergence. Assuming that the value of ϵ is small relative to t^*, a simple approach is to just hold the previously computed value $\dot{y}_e(t_r^-)$ for $t_r \leqslant t < t_r + \epsilon$ [34, 115]. Alternatively, one may opt for a polynomial extrapolation. For example, a straight line extrapolation is given by

$$\dot{y}_e(t) = \dot{y}_e(t_r^-) + (t - t_r)\ddot{y}_e(t_r^-), \quad t \in [t_r, t_r + \epsilon). \tag{4.16}$$

Depending on when the reset occurs, a straight line approximation can produce worse results than constant approximation. In any case, the existence of the ϵ-delay is a clear limitation of the AD method. This is because, for signals of increasing bandwidth, the necessary reduction of t^* (assuming a fixed K) implies that ϵ becomes larger in proportion to t^*. By a certain bandwidth an intolerable proportion of of the derivative estimate is based on extrapolation. This limitation motivates the notion of overlapping estimation.

4.2.3 Overlapping estimation

A natural solution to eliminate the need for an extrapolating mechanism is to employ dual, time-shifted estimators. That is, when one estimator is approaching reset, the output could be switched to the other estimator which has begun to produce accurate estimates, and vice-versa. The additional advantage of this approach is the reduction in design parameters since we can conveniently set $t^* = 2\epsilon$ while guaranteeing that one filter is always producing accurate estimates, provided the estimators are offset in time by ϵ. Figure 4.1 illustrates this idea. Time-shifted estimation can be implemented by the following formula

$$\dot{y}_e(t) = \begin{cases} \dot{y}_{e_1}(t_1), & t_2 < t_1 \\ \dot{y}_{e_2}(t_2), & t_2 \geqslant t_1 \end{cases} \tag{4.17}$$

where $\dot{y}_{e_1}(t_1), \dot{y}_{e_2}(t_2)$ are the estimates of two filters with staggered, periodic resets such that $t_1 = \text{mod}(t, t^*)$ and $t_2 = \text{mod}(t+\epsilon, t^*)$. The combined result is a piecewise continuous estimate of a signal's time derivative for which ϵ can be chosen sufficiently small to obtain the desired accuracy. A new kind of limitation exists with the overlapping-estimator approach, however, and that is noise induced by filter switching. In particular, overly-frequent filter switching degrades the derivative estimate of low frequency signals. As such, practical limits exist as to how high and how low ϵ can be chosen for a particular choice of truncation order. A simulation study was conducted to quantify these limits. In this study, we determine the frequency range over which derivative estimates of a prescribed accuracy can be obtained. The study is repeated over various combinations of the two design parameters, K and ϵ. For each combination we apply a sine sweep and measure the error between the actual and estimated derivatives at each discrete frequency. Error is measured in root-mean-square (RMS) and plotted as a percentage of the RMS value of the true derivative. This is expressed as

$$\%\text{error} = \frac{\sqrt{\frac{1}{N}\sum_{k=0}^{N-1}(\dot{y}_e(kT) - \dot{y}(kT))^2}}{\sqrt{\frac{1}{N}\sum_{k=0}^{N-1}(\dot{y}(kT))^2}} \times 100$$

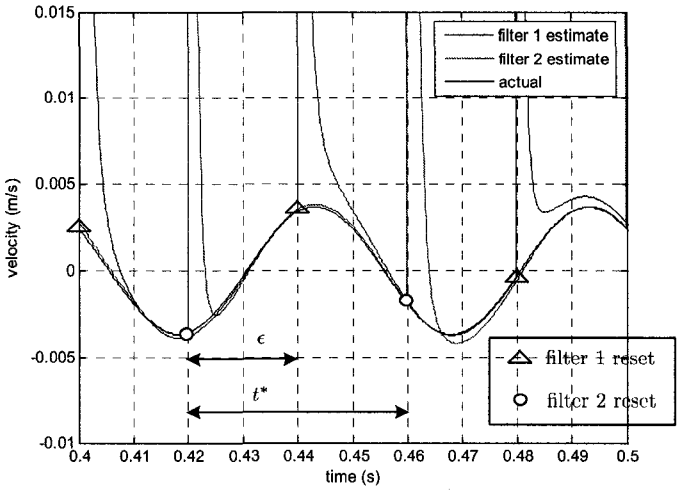

Figure 4.1: The idea of overlapping estimation is that two time shifted estimators produce a piecewise continuous estimate. The period between resets of an individual estimator ("filter") is denoted t^*, and the time needed after reset before an estimator obtains convergent estimates is denoted ϵ.

for N samples over one period of the sinusoid at the chosen frequency, with the sampling period $T = 0.1$ ms. Figure 4.2 plots the derivative error versus frequency over a grid of K and ϵ. As a measure of accuracy, a "± 3 dB boundary" is superimposed on the plots, indicating when the estimation error measures $\pm(1-1/\sqrt{2})$. For each value of K, it is evident that decreasing ϵ improves the derivative estimation accuracy for higher frequency sinusoids but degrades the derivative estimation accuracy for lower frequency sinusoids. Increasing the truncation order correlates to a widening of the frequency band under the ± 3 dB boundary. It appears, however, that there is a hard limit on the overall algorithm. Over the grid of parameter values considered in this study, only consistent accuracy from DC to about 90 Hz is achievable for our implementation. Accuracy beyond 90 Hz is accompanied by intolerable degradation to the derivative estimation of sinusoids near DC.

4.3 Case study: nonlinear control of an AMB

As a practical example, we revisit AMBs and consider the 1DOF case for simplicity. A dynamic model representative of the 5DOF dynamics studied in Chapter 3 is given by

$$m\ddot{y} = F_y + F_c + F_h, \tag{4.18a}$$

$$\dot{F}_c = 0, \tag{4.18b}$$

$$\ddot{F}_h = -\omega^2 F_h, \tag{4.18c}$$

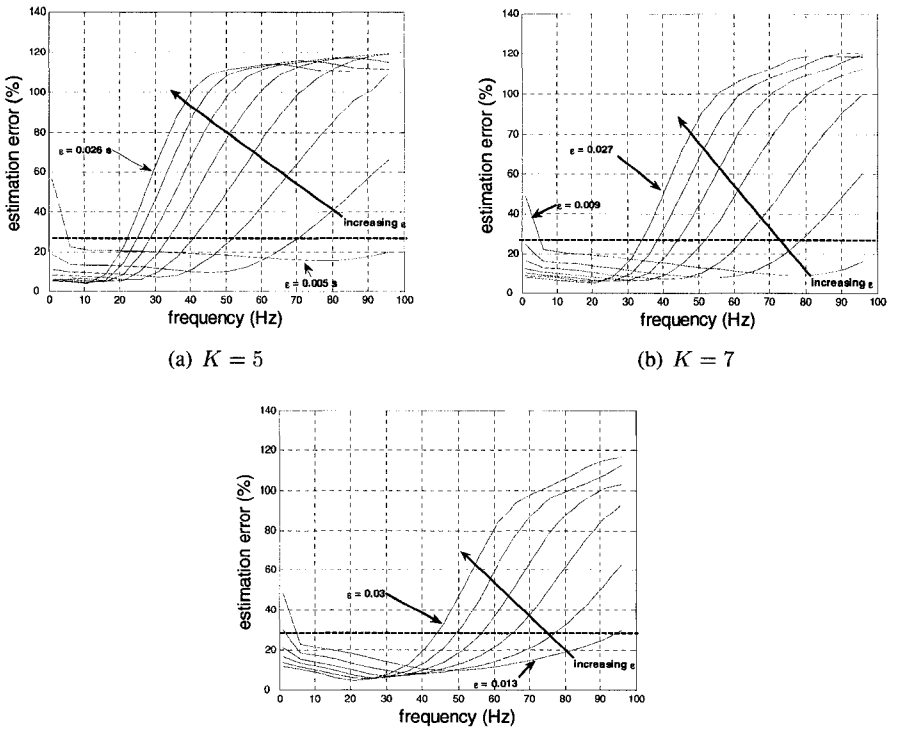

(a) $K = 5$

(b) $K = 7$

(c) $K = 9$

Figure 4.2: Derivative estimation error of a harmonic signal as a function of frequency. Each curve corresponds to an increment of 3 ms for ϵ.

where y is the rotor displacement from the center of the AMB and m denotes the rotor mass. F_y is the net magnetic force due the bearing given by the standard model

$$F_y = \frac{\beta i_p^2}{(\kappa - y)^2} - \frac{\beta i_n^2}{(\kappa + y)^2} \tag{4.19}$$

for input coil currents i_p, i_n, nominal air gap κ and force constant β. F_c is the constant disturbance force and F_h is the harmonic disturbance force with a frequency of ω.

We consider the 1DOF equivalent of the nonlinear control law described in Chapter 3, Section 3. The force feedback

$$F_y = -F_c - F_h + m(\ddot{y}_r - k_v(\dot{y} - \dot{y}_r) - k_p(y - y_r)) \tag{4.20}$$

yields the stable tracking error dynamics $\ddot{e} + k_v\dot{e} + k_p e = 0$ for gains $k_p, k_v > 0$, tracking error $e = y - y_r$, and a twice differentiable reference trajectory y_r. The control currents i_p, i_n are calculated from inversion of the force relation (4.19) via CCS as given by (2.25). We compare state estimation approaches. First, we consider a fifth-order nonlinear observer

having linear error dynamics [131]. This observer is given by

$$\dot{\hat{y}} = \hat{v}_y \qquad +\ell_1(y-\hat{y}), \tag{4.21a}$$

$$\dot{\hat{v}}_y = (F_y(\Delta i, y) + \hat{F}_c + \hat{F}_h)/m \qquad +\ell_2(y-\hat{y}), \tag{4.21b}$$

$$\dot{\hat{F}}_c = \qquad \ell_3(y-\hat{y}), \tag{4.21c}$$

$$\dot{\hat{F}}_h = \hat{F}_v \qquad +\ell_4(y-\hat{y}), \tag{4.21d}$$

$$\dot{\hat{F}}_v = -\omega^2\hat{F}_h \qquad +\ell_5(y-\hat{y}), \tag{4.21e}$$

where $v_y = \dot{y}$, $F_v = \dot{F}_h$ and ℓ_i are the observer gains. Second, we reconsider the equivalent reduced-order nonlinear observer from Chapter 3, Section 3, where velocity is made available by the AD method. The reduced-order observer is

$$\begin{aligned}\begin{bmatrix}\dot{z}_1\\ \dot{z}_2\\ \dot{z}_3\end{bmatrix} &= \begin{bmatrix}-h_1 & -h_1 & 0\\ -h_2 & -h_2 & 1\\ -h_3 & -(h_3+\omega^2) & 0\end{bmatrix}\begin{bmatrix}z_1\\ z_2\\ z_3\end{bmatrix}\\ &\quad - \begin{bmatrix}h_1^2+h_1h_2 & h_1\\ h_1h_2+h_2^2-h_3 & h_2\\ h_1h_3+h_2(h_3+\omega^2) & h_3\end{bmatrix}\begin{bmatrix}m\dot{y}_e\\ F_y(\Delta i, y)\end{bmatrix},\end{aligned} \tag{4.22a}$$

$$\begin{bmatrix}\hat{F}_c\\ \hat{F}_h\end{bmatrix} = \begin{bmatrix}z_1\\ z_2\end{bmatrix} + \begin{bmatrix}h_1\\ h_2\end{bmatrix} m\dot{y}_e, \tag{4.22b}$$

where h_i are the reduced-order observer gains. For a given truncation order K, the combined order of the overlapping velocity estimator and reduced-order disturbance observer is $2(K-1)+3$.

Ideally, computing an additional derivative would allow us to estimate the disturbance forces simply by rearranging (4.18a). The simulation study shows, however, that the accuracy of the second order derivative via overlapping estimation is more limited in terms of bandwidth and noise susceptibility. An accurate second derivative estimate could not be obtained for a sufficiently wide enough range of frequencies to be applicable to the problem of AMB disturbance estimation.

4.4 Simulations

The following simulations present transient performance of the AMB subject to a 40 Hz (2400 r/min) harmonic disturbance force to simulate mass unbalance.In the first simulation the rotor is levitated from its initial position at $y(0) = 100$ μm without disturbance compensation. At $t = 0.5$ s, disturbance compensation is engaged to bring the rotor to the origin.

Since the AD method is formulated in continuous time, discretization is carried out by the Euler method with a step size of 0.1 ms. All other simulation parameters are provided in Table 4.1. The overlapping estimator in this example is 7^{th} order ($K = 7$). Since a single derivative is being estimated, we only need the following coefficients, as determined by (4.15): $a_{1,0} = 5040, a_{1,1} = 35280, a_{1,2} = 52920, a_{1,3} = 29400, a_{1,4} = 7350, a_{1,5} = 882, a_{1,6} = 42$. Figures 4.3 and 4.4 compare two implementations of the AD method for velocity estimation. Figure 4.3 utilizes a single estimator with constant extrapolation, given by the formula

$$\dot{y}_e(t) = \begin{cases} \dot{y}_e(t_r^-), & t \in [t_r, t_r + \epsilon) \\ -\frac{\eta_1 + a_{K-1}(t_r - t)^{K-1} y(t)}{(t_r - t)^K}, & t \in [t_r + \epsilon, t_r + t^*). \end{cases} \tag{4.23}$$

The chosen parameters were $\epsilon = 4$ ms and $t^* = 40$ ms based on a numerical search for the best closed-loop performance. Although a single estimator produces acceptable performance, error in the estimated velocity due to extrapolation induces error in the disturbance estimates as well as less responsiveness in the controller.

Figure 4.4 presents the closed-loop response using overlapping estimators. Overlapping estimation is implemented by the formula (4.17) with $t^* = 2\epsilon = 24$ ms. These parameters were determined from the data in Figure 4.2 so as to achieve good accuracy from DC to approximately 80 Hz. Figure 4.4(a) indicates that closed-loop performance has been significantly improved relative to Figure 4.3(a). Figure 4.4(d) shows that $\dot{y}_e$ continually approximates $\dot{y}$ with good accuracy and demonstrates only minor degradation when disturbance compensation is engaged. The performance improvement obtained with overlapping estimation comes at the cost increased computational requirements, but it is not excessive with respect to present digital signal processor capabilities.

Parameter	Value	Parameter	Value
F_c	2.0 N	F_h	1.0 N
i_b	1.0 A	ω	80π rad/s
β	$5.0 \cdot 10^{-6}$ N-m^2/A^2	κ	$8.0 \cdot 10^{-4}$ m
m	0.4 kg		
ROO poles	$\{-5, -400, -400\}$	controller poles	$\{-50 \pm 300i\}$
FOO poles	$\{-2500, -2500, -5, -400, -400\}$		

Table 4.1: Simulation parameters. FOO denotes "full-order observer" given by (4.21), and ROO denotes "reduced-order observer" given by (4.22).

A second simulation considers whether velocity estimated by the AD method offers control performance enhancements relative to velocity estimation by an observer. We compare the overlapping estimator plus reduced-order disturbance observer to the full-order

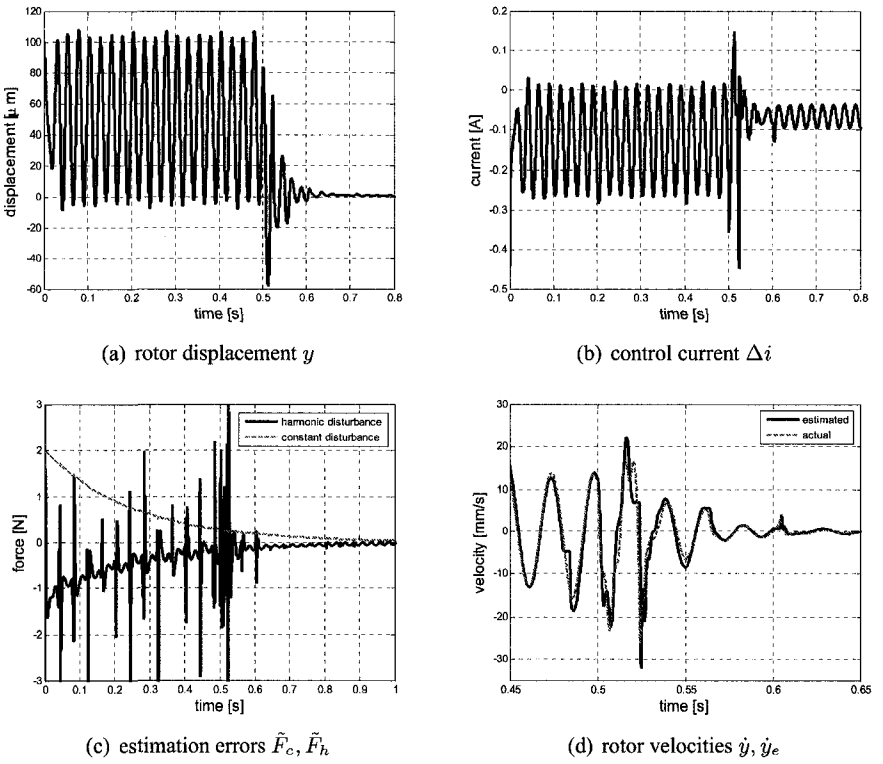

(a) rotor displacement y

(b) control current Δi

(c) estimation errors $\tilde{F}_c, \tilde{F}_h$

(d) rotor velocities $\dot{y}, \dot{y}_e$

Figure 4.3: Nonlinear control of a 1DOF magnetic bearing integrating the AD method for velocity estimation. The AD approach is this example uses constant extrapolation to estimate the derivative during reset, as given by (4.23).

observer given in (4.21a)-(4.21e). A different, although realistic, scenario is considered. At $t = 3$ s, a step load change is applied, that is, $F_c(t) = 2(1(t) + 1(t-3))$. To assess each method's robustness to high frequency perturbation, a normally-distributed white noise variable $w(t)$ is introduced in the output $y(t)$. The maximum amplitude of $w(t)$ is set to 0.4 μm to simulate measurement noise commonly encountered from an inductive AMB position sensor. We compare the natural filtering effect of each approach, hence there is no additional filtering applied.

Figure 4.5 shows the results of this comparison. Bearing in mind that both observers estimate disturbances with a similar rate of decay, Figure 4.5(a) shows that estimated state feedback using AD is more robust to the load change than the feedback based on a full-order observer. This performance discrepancy can be explained by observing each approach's velocity estimate in Figures 4.5(c)-4.5(d). The constant disturbance must be re-estimated by the full-order observer before its velocity can asymptotically converge whereas

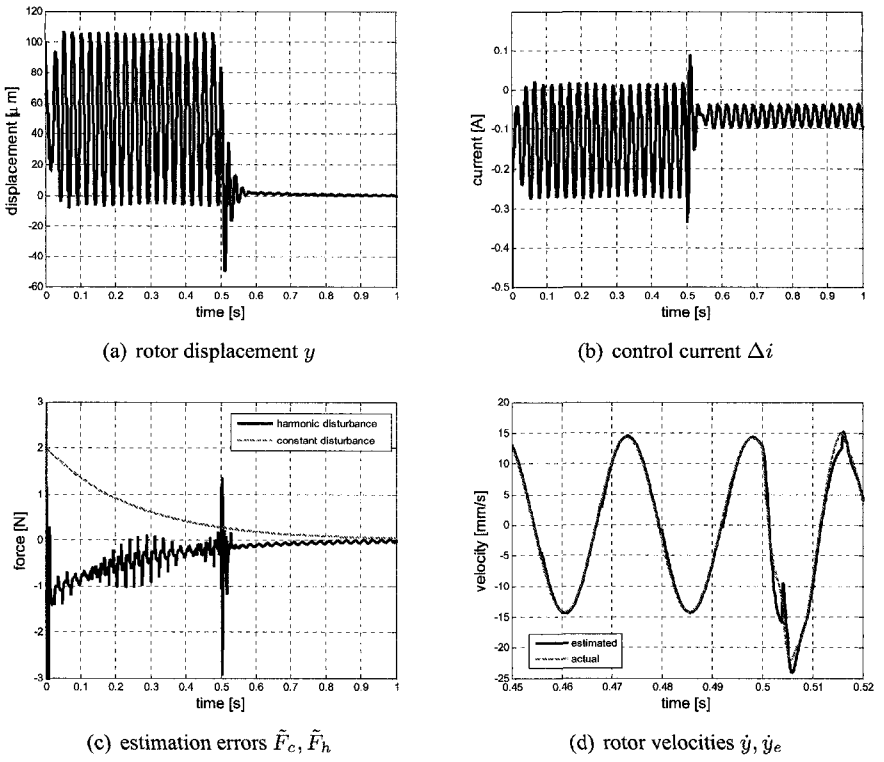

(a) rotor displacement y

(b) control current Δi

(c) estimation errors $\tilde{F}_c, \tilde{F}_h$

(d) rotor velocities $\dot{y}, \dot{y}_e$

Figure 4.4: Nonlinear control of a 1DOF magnetic bearing integrating the AD method for velocity estimation. The AD approach is this example uses the overlapping-estimator approach given by (4.17).

the model-free approximation of the AD method maintains consistent accuracy. Observing Figure 4.5(d) more closely after $t = 3$ s, it is shown that the load change yields an underestimate of the true velocity. This leads to a reduction in damping, thus degrading the closed-loop performance. Performance can be recovered somewhat by increasing the observer gains, but not without significantly amplifying the noise. Figure 4.5 presents the spectra of velocities estimated by the two approaches in the frequency range up to 1 kHz. Beyond the synchronous frequency, the AD method demonstrates better noise rejection. For either method, the spectrum at higher frequencies than those shown in Figure 4.5(b) can be shaped by additional lowpass filtering.

4.5 Conclusion

This chapter has presented a numerical study of the overlapping estimator implementation of the AD method. Application to a 1DOF AMB demonstrates the feasibility of the

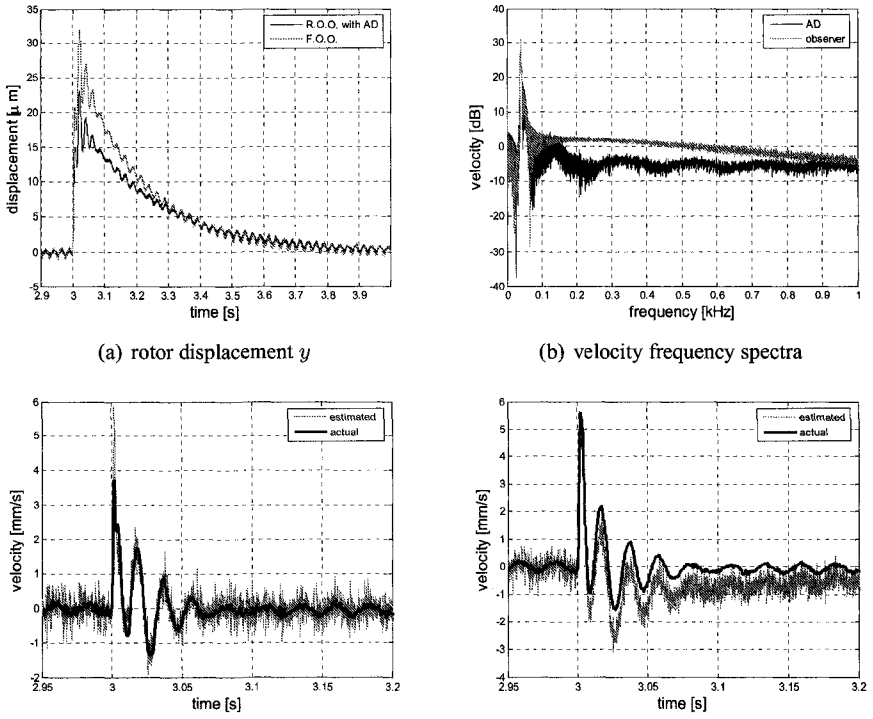

(a) rotor displacement y

(b) velocity frequency spectra

(c) actual and estimated velocities using AD

(d) actual and estimated velocities using a FOO

Figure 4.5: Closed-loop response comparison of a 1DOF AMB based on two different state estimation approaches. The first approach is a full-order nonlinear observer (FOO). The second approach is a reduced-order nonlinear observer (ROO) combined with the overlapping AD method. Since the AD method is model-free and non-asymptotic, velocity estimation is more robust to disturbances than estimation by a model-based, state observer.

method for systems of higher closed-loop bandwidth than previously studied. Improved disturbance rejection is demonstrated by integrating the AD method into estimated state feedback. Chapter 7 demonstrate real-time application of the method.

Chapter 5

Force and Torque Modeling of a Toothless Self-Bearing Servomotor

We depart from the study of active magnetic bearings (AMBs) and consider in this chapter another electromagnetic actuator, namely the self-bearing motor (SBM). In particular, we focus on a type of SBM known as the toothless self-bearing servomotor (TSBS). Our study of the TSBS begins with an analysis of its operating principle.

5.1 Introduction

SBMs, to briefly review the discussion in Chapter 1, Section 2, are electric motors with the built-in functionality of an AMB. The resulting device provides levitation and rotation simultaneously. The main advantages are an increased power density and a reduced shaft length which softens the performance limitations imposed by rotordynamics.

The theory and application of SBMs have been reported since the early 1990s. Chiba et al. [17, 18, 15, 92] made early contributions to the analysis, design, control and implementation of self-bearing permanent magnet (PM), induction, and reluctance-type motors. Their SBM designs are noted for their four-pole motor windings with additional two-pole radial force windings, and their induction motor in [17] reaches a speed of $12,000$ r/min. Reference [92] identifies an inherent force-torque trade-off in PM-type SBMs that base levitation on the Maxwell force principle. Alternatively, pioneering work by Bischel [9] proposed a Lorentz-force magnetic bearing integrated into a PM synchronous motor. The principle of this novel "all-Lorentz" SBM is confirmed by application to a 1 kW, $2,000$ r/min machine. Okada et al. [88, 91] provided a general theory for self-bearing operation and radial position control in PM synchronous and induction-type motors based on the so-called $P \pm 2$ principle, i.e. designs where the stator pole number is $P \pm 2$, P being the rotor pole number.

Reference [91] reports on a novel internal PM SBM which demonstrates an improved radial force capacity relative to surface-mounted PM SBMs.

In the current decade an increasing number of industrial applications of SBMs had been reported. Reference [97] presents extensive testing of a 30 kW canned motor pump based on a self-bearing induction motor; [93] evaluates a 11,000 r/min, 4 kW PM SBM suitable as a general-use liquid pump. Schöb et al. [110] report on the application of a slice motor to a cardiac assist device. The slice motor, shown in Figure 1.6(b), has the unique advantages of passive stabilization of the axial and tilting motions and is the basis for a host of industrial applications [109]. The cardiac assist device remains an active area of research by others [87, 133] as is the design optimization and nonlinear control of the slice motor [114, 40].

For precision pointing and slewing applications, the TSBS was introduced [23]. The TSBS is a PM synchronous machine with a toothless, or slotless, stator to minimize cogging torque. As in [9], the TSBS is an all-Lorentz machine. The advantage of all-Lorentz SBMs such as the TSBS is that force and torque can be increased simultaneously by increasing the PM size. Hence, all-Lorentz SBMs overcomes the previously examined force-torque trade-off [92]. In this chapter, we model the TSBS from first principles.The reason for doing this is because the TSBS is a nonlinear system and no explicit nonlinear model has been established. We approach modeling in a control-oriented manner such that we capture the key nonlinear characteristics of the actuator with a relatively compact model structure. The resulting model is potentially useful for the design of nonlinear compensation [92, 40], control over a wider operating regime, and providing more physical insight.

Central to TSBS modeling is bearing force and torque characterization, specifically, determining the static force-torque-current-displacement relationship within the actuator. Force and torque characterization is the specific focus of this chapter. Significant TSBS modeling efforts have already been put forth based on one-dimensional (1D) [120, 119, 121] and two-dimensional (2D) [103, 102] flux models. Previous 1D modeling provides sufficient physical insight while the 2D work yields improved accuracy. All previous TSBS modeling efforts lead to linear force and torque expressions. For work based on a 2D flux model, linearization appears to be necessary due to the complexity of the partial-differential-equation (PDE)-based solution. This chapter's approach is to revisit 1D modeling and derive nonlinear analytical expressions. Essential to obtaining a reasonably accurate, yet simple, nonlinear model is parameter identification from system data. As such, our analytical model is linearly parameterized so that linear least squares can be utilized to optimize the model fit-to-data. Ultimately, parameter identification leads to simpler non-

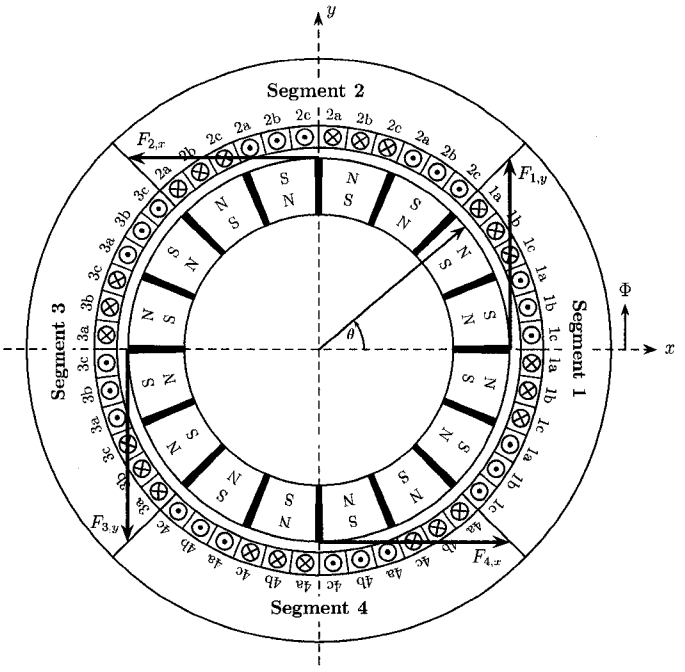

Figure 5.1: Cross-section of a 16-pole, toothless self-bearing servomotor (TSBS). The TSBS is a segmented permanent magnet synchronous machine. Each of the four segments shown is an individually controlled three-phase motor. The x and y axes denote rotor coordinates relative to the stator center, Φ is the stator angle and θ is the rotor angle. The four control forces $F_{1,y}, F_{2,x}, F_{3,y}$ and $F_{4,x}$ produce levitation and rotation simultaneously.

linear expressions than those given by the original analytic model because we can identify and discard portions of the model which insignificantly contribute to the model fit-to-data. Finite element analysis (FEA) data, representative of a laboratory TSBS, is employed for parameter identification and for validation of the analytical force and torque model structure.

5.1.1 Operating principle

Figure 5.1 presents the cross-section of an idealized sixteen-pole TSBS. The TSBS is essentially a segmented three-phase permanent magnet synchronous machine (PMSM). That is, it consists of multiple, individually controlled three-phase windings. Therefore, each segment can be thought of as a three-phase motor on its own, with the phases for segment k denoted k, a and k, b and k, c. A traditional three-phase PMSM creates torque by interaction of the flux from the surface-mounted PMs with the flux from the winding currents. Multiple segments permit radial force generation on the rotor in addition to torque. This

allows levitation of the rotor in addition to rotation. Therefore the TSBS provides three positional degrees of freedom.

In its idealized conception [119], the four segments generate the four tangential forces $F_{1,y}, F_{2,x}, F_{3,y}, F_{4,x}$. Without segmentation, all of these forces are equal and only torque is generated, resulting in conventional PMSM operation. With four segments, unbalanced forces can be generated along each axis, specifically when $F_{1,y} \neq F_{3,y}$ and $F_{2,x} \neq F_{4,x}$. In this case, net radial forces are applied to the motor in addition to torque. Each of the forces $F_{1,y}, F_{2,x}, F_{3,y}, F_{4,x}$ is proportional to the current amplitude of its respective three-phase winding.

In the absence of mechanical bearings, eccentric rotor positioning is possible. When the rotor is off-center, significant unbalance forces are induced from attraction between the rotor and the stator. As a result, the TSBS is an open-loop unstable system requiring radial position sensing and feedback control to maintain levitation. As with all synchronous machines, commutation of the three-phase currents for each segment requires knowledge of the rotor angle. This information is obtained from a rotary angle encoder.

A salient feature of the TSBS is that it has a toothless stator. The purpose of the toothless stator is to produce smoother torque by minimizing cogging torque and detent. The combination of being toothless and contactless makes the TSBS ideal for precision motion control applications. An example of this is described in Chapter 1, Figure 1.8.

5.2 Bearing force and torque modeling

We develop static, analytical functions for radial force and torque for the TSBS. We define the stationary coordinate system shown in Figure 5.1, where x and y denote radial displacement of the rotor from the center of the stator. The angle θ denotes the angle of the rotor relative to its "home" position, also depicted in Figure 5.1. The angular position along the stator is denoted by Φ and has an origin defined by the x-axis. Under the primary assumption of a 1D flux distribution, this section derives the motor's force and torque as a function of rotor position (x, y, θ) and excitation currents.

5.2.1 Current distribution

Figure 5.2 shows the winding configuration schematically and for an actual TSBS. Each segment spans $\pi/2$ mechanical radians (radM) and its circumferential location is defined

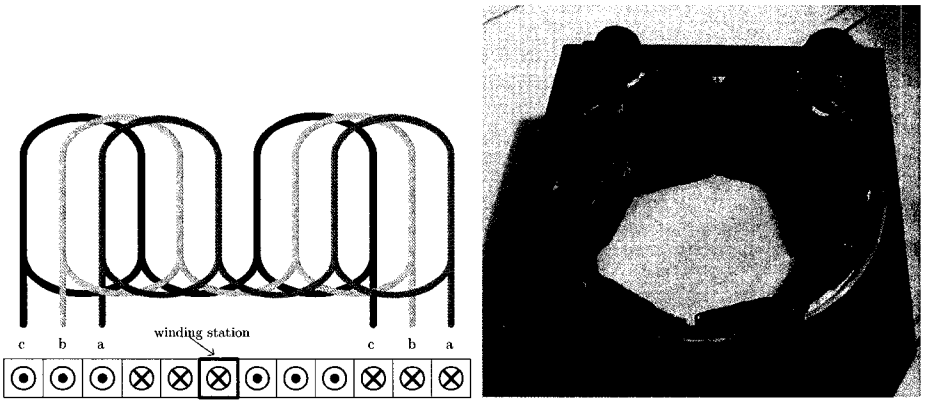

(a) schematic for single segment (b) actual toothless stator with windings

Figure 5.2: Winding configuration.

according to the stator angle Φ by

$$\pi\left(\frac{k}{2}-\frac{3}{4}\right) \leqslant \Phi_k < \pi\left(\frac{k}{2}-\frac{1}{4}\right), \quad 1 \leqslant k \leqslant 4. \tag{5.1}$$

Each segment represents a three-phase concentrated winding consisting of $3M/2$ *winding stations* where M is the number of PM pole pairs. The winding stations are depicted in Figure 5.2(a). Each winding station spans $\pi/(3M)$ radM and is composed of N_w wires, assumed to be uniformly distributed. The winding distribution for the a, b and c phases, $N_a(\Phi), N_b(\Phi), N_c(\Phi)$ respectively, are physically displaced relative to one another by $\pi/3$ electrical radians (radE). For a high number of poles, which is the case in the practical realization of a TSBS to obtain sufficient bearing force and torque capacity, the concentrated windings are well approximated as sinusoidally distributed. Under a sinusoidal approximation, we express the phase winding distributions as

$$N_a(\Phi) = N_0 \sin\left(M\Phi - \frac{\pi}{3}\right), \tag{5.2a}$$

$$N_b(\Phi) = N_0 \sin\left(M\Phi\right), \tag{5.2b}$$

$$N_c(\Phi) = N_0 \sin\left(M\Phi + \frac{\pi}{3}\right), \tag{5.2c}$$

where N_0 is the amplitude of the sinusoidally approximated distribution. The windings for a prototype TSBS are shown in Figure 5.2(b).

To obtain a sinusoidal current distribution, the three-phase currents $i_{k,a}, i_{k,b}, i_{k,c}$ for segment k are correspondingly displaced by $\pi/3$ radE in phase angle. They are expressed

by

$$i_{k,a}(i_k, \gamma_k, \theta) = i_k \cos\left(M(\theta + \gamma_k) - \frac{\pi}{3}\right), \tag{5.3a}$$

$$i_{k,b}(i_k, \gamma_k, \theta) = i_k \cos\left(M(\theta + \gamma_k)\right), \tag{5.3b}$$

$$i_{k,c}(i_k, \gamma_k, \theta) = i_k \cos\left(M(\theta + \gamma_k) + \frac{\pi}{3}\right), \tag{5.3c}$$

and are controlled by their magnitude i_k and optionally their phase angle γ_k. For now it is assumed that $\gamma_k = 0$, but in Chapters 6 and 7 we will consider how it can be advantageous. The current distribution for the k^{th} segment is thus given by

$$\begin{aligned} I_k(\Phi, \theta) &= N_a(\Phi) i_{k,a}(\theta) + N_b(\Phi) i_{k,b}(\theta) + N_c(\Phi) i_{k,c}(\theta) \\ &= N_0' i_k \sin\left[M\left(\Phi - \theta\right)\right]. \end{aligned}$$

where $N_0' = 3N_0/2$. The overall current distribution I is given by

$$I = \begin{cases} I_1, & -\pi/4 \leq \Phi < \pi/4 \\ I_2, & \pi/4 \leq \Phi < 3\pi/4 \\ I_3, & 3\pi/4 \leq \Phi < 5\pi/4 \\ I_4, & 5\pi/4 \leq \Phi < 7\pi/4 \end{cases}$$

which is a sinusoid with a piecewise constant amplitude. Further analysis of the winding configuration is found in [103].

5.2.2 Magnetic flux distribution

Magnetic circuit analysis [22] is adopted to estimate the flux distribution within the TSBS. In applying magnetic circuit analysis, we are assuming that a uniform flux flows across along discrete paths between the rotor and the stator. This is the so-called *1D* magnetic modeling approach because all of the magnetic flux contributing to force and torque is assumed to be radially directed across the air gap, and that tangentially-directed flux in the air gap can be neglected. For a toothless machine the 1D approach is clearly an idealization since the iron does not provide discrete paths of flux flow. A partial-differential-equation-based, i.e. *2D*, approach is more general and can capture the force and torque contributions from tangential flux flow [101]. The benefit of the 1D approach is that the force and torque expressions are considerably more simple.

A 1D characterization of the magnetic flux distribution involves superposition of two separate sources of air-gap flux density, namely the PMs and the stator windings. Superposition of is valid under the assumption that no saturation of the iron occurs. Figure 5.3 shows the unwrapped geometry of the TSBS, and superimposed is a possible reluctance

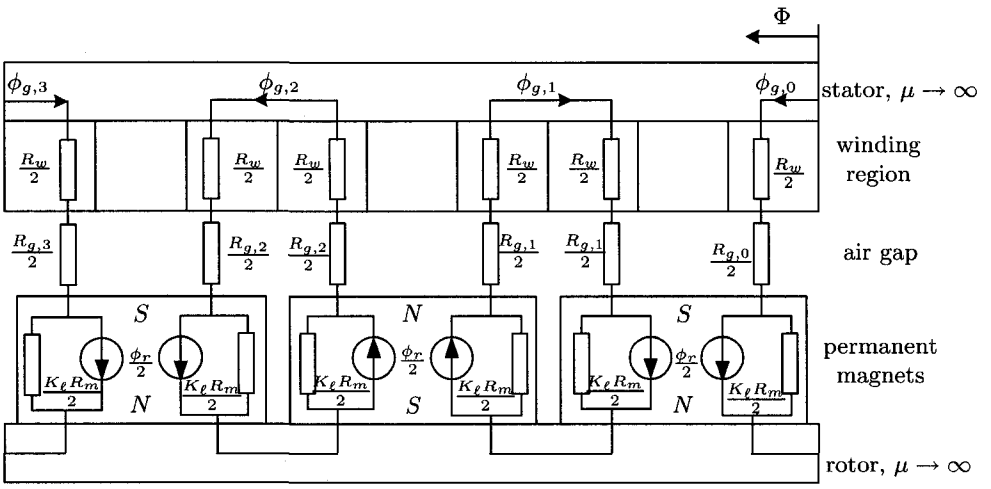

Figure 5.3: Unwrapped geometry of the toothless self-bearing servomotor with decoupled magnetic circuits superimposed.

network approach to model PM flux across the air gap. The TSBS is spatially discretized to approximate the PM reluctance R_m, winding region reluctance R_w, and air gap reluctances R_{g_i} which vary from circuit to circuit. A de-rating factor K_ℓ scales the PM reluctance as a way to approximate the effect of leakage flux in the air gap and iron is assumed to be infinitely permeable. Whereas a fully coupled reluctance network would lead to complex solutions for the air gap flux, we instead opt for decoupled magnetic circuits which is a reasonable approximation [50].

The PMs are modeled as constant flux sources with remanence flux $\phi_r = B_r A_m$ where B_r is the remanence flux density and A_m is the PM outer cross-sectional area. From Figure 5.3, analysis of the i^{th} magnetic circuit leads to expressions for the air gap flux given by

$$\phi_{g,i}(x,y) = \frac{K_\ell R_m}{R_{g_i}(x,y) + R_w + K_\ell R_m}\phi_r, \quad 0 \leqslant i \leqslant 2M-1. \tag{5.4}$$

Correspondingly, the magnitude of the air gap flux density is approximated as

$$\begin{aligned} \bar{B}_{g,m_i}(x,y) &= \frac{\phi_{g,i}(x,y)}{A_g} \\ &= \frac{C_\phi B_r K_\ell R_m}{R_{g_i}(x,y) + R_w + K_\ell R_m}, \end{aligned} \tag{5.5}$$

where A_g is the cross-sectional area of the winding region opposite a PM, and $C_\phi = A_m/A_g$ is the flux concentration factor. Now, since the TSBS is toothless, then the air gap is annular, and the radial distance between the rotor and stator, g, can be approximated

by

$$g(x, y, \Phi) = g_0 - x\cos\Phi - y\sin\Phi,$$

where g_0 is the nominal air gap. Therefore, for the i^{th} magnetic circuit, we approximate the air gap by the $g_i(x, y) := g(x, y, \Phi_i)$ where $\Phi_i = \pi i/8$ and it is assumed that $\theta = 0$. Therefor the air gap reluctances are given by

$$R_{g_i}(x, y) = \frac{g_i(x, y)}{\mu_0 A_g}. \tag{5.6}$$

Our magnetic circuit models a flux density that is a square-wave function of the stator angle, where the magnitude of the square wave varies from circuit to circuit, as determined by (5.5). The flux density is more realistic as a continuous function, which we obtain by assuming that the air gap reluctance varies continuously as a function of Φ, i.e.

$$R_g(x, y, \Phi) = \frac{g_0 - x\cos\Phi - y\sin\Phi}{\mu_0 A_g},$$

whereby the magnitude of the air gap flux density function becomes

$$\bar{B}_{g,m}(x, y, \Phi) = \frac{C_\phi B_r K_\ell R_m}{R_g(x, y, \Phi) + R_w + K_\ell R_m}. \tag{5.7}$$

Finally, we approximate the square wave flux density function by sinusoid of equivalent root-mean-square value [120],

$$\begin{aligned} B_{g,m}(x, y, \Phi, \theta) &= \sqrt{2}\bar{B}_{g,m}(x, y, \Phi)\sin[M(\Phi - \theta)] \\ &= -\frac{\sqrt{2}C_\phi B_r K_\ell R_m \sin[M(\Phi - \theta)]}{R_g(x, y, \Phi) + R_w + K_\ell R_m} \\ &= \frac{m_1 \sin[M(\theta - \Phi)]}{m_2 - x\cos\Phi - y\sin\Phi}, \end{aligned} \tag{5.8}$$

where constants $m_1 = \sqrt{2}C_\phi B_r \mu_0 A_g K_\ell R_m$ and $m_2 = \mu_0 A_g (K_\ell R_m + R_w) + g_0$ are used to simplify notation in (5.8).

The current distribution I is also a source of air gap flux. A decoupled reluctance network once again forms the basis for the following expressions, and the derivation is analogous to what was just described. As a rough approximation, we assume no tangential leakage flux and therefore the winding flux links all the turns in each coil. The resulting air-gap flux density distribution for the i^{th} circuit is

$$\bar{B}_{g,w_i}(x, y, i_k) = \frac{N_0' i_k}{A_g(R_w + R_m + R_{g_i}(x, y))},$$

where the current magnitude i_k is determined according to which segment the i^{th} magnetic circuit is located based on (5.1). The continuous flux density magnitude for the k^{th} segment

is given by

$$\bar{B}_{g,w}(x, y, \Phi, i_k) = \frac{N_0' i_k}{A_g(R_w + R_m + R_g(x, y, \Phi))},$$

and making a sinusoidal approximation to the square wave function, we have

$$\begin{aligned} B_{g,w,k}(x, y, \Phi, \theta, i_k) &= \sqrt{2}\bar{B}_{g,w}(x, y, \Phi, i_k)\cos[M(\Phi - \theta)] \\ &= \frac{\sqrt{2}N_0' i_k \cos[M(\Phi - \theta)]}{A_g(R_w + R_m + R_g(x, y, \Phi))} \\ &= \frac{w_1 i_k \cos[M(\Phi - \theta)]}{w_2 - x\cos\Phi - y\sin\Phi}. \end{aligned} \tag{5.9}$$

The above cosine approximation of the flux density indicates that the air gap flux due to the windings is displaced $\pi/2$ radE with respect to the current distribution. Furthermore, we have defined constants $w_1 = \sqrt{2}\mu_0 N_0'$ and $w_2 = \mu_0 A_g(R_w + R_m) + g_0$. Note, however, that (5.9) applies to the k^{th} segment, and that the overall flux density function $B_{g,w}$ is only piecewise continuous. As a result, we are ignoring flux coupling between segments for the sake of maintaining simple expressions, however, inter-segment flux coupling is addressed in [102].

Figure 5.4 depicts the waveforms for the radial air gap flux density components and current distribution for a single segment.

5.2.3 Force and torque calculation

The total force and torque acting on the TSBS rotor is determined by integrating the Maxwell stress tensor [132, 114] over the surface of the stator. Generally speaking, the Maxwell stress tensor T_M is given by

$$T_M = \mu \begin{bmatrix} H_x^2 - \frac{1}{2}H^2 & H_z H_y & H_x H_z \\ H_y H_x & H_y^2 - \frac{1}{2}H^2 & H_y H_z \\ H_z H_x & H_z H_y & H_z^2 - \frac{1}{2}H^2 \end{bmatrix}, \tag{5.10}$$

where μ is the magnetic permeability, H is the magnitude of the magnetic field intensity vector and H_x, H_y, H_z denote the associated components in the cartesian coordinate system (x, y, z). The mechanical stress T acting on a surface element is calculated with

$$T = T_M e_n, \tag{5.11}$$

where e_n is vector perpendicular to the surface element. Now, consider the cylindrical surface S defined by the inner surface of the stator. When expressed in cylindrical coordinates (R, Φ, z), the surface element of the stator surface has a normal component in the R direction only. Furthermore, having assumed that the tangential, i.e. Φ-directed, component of

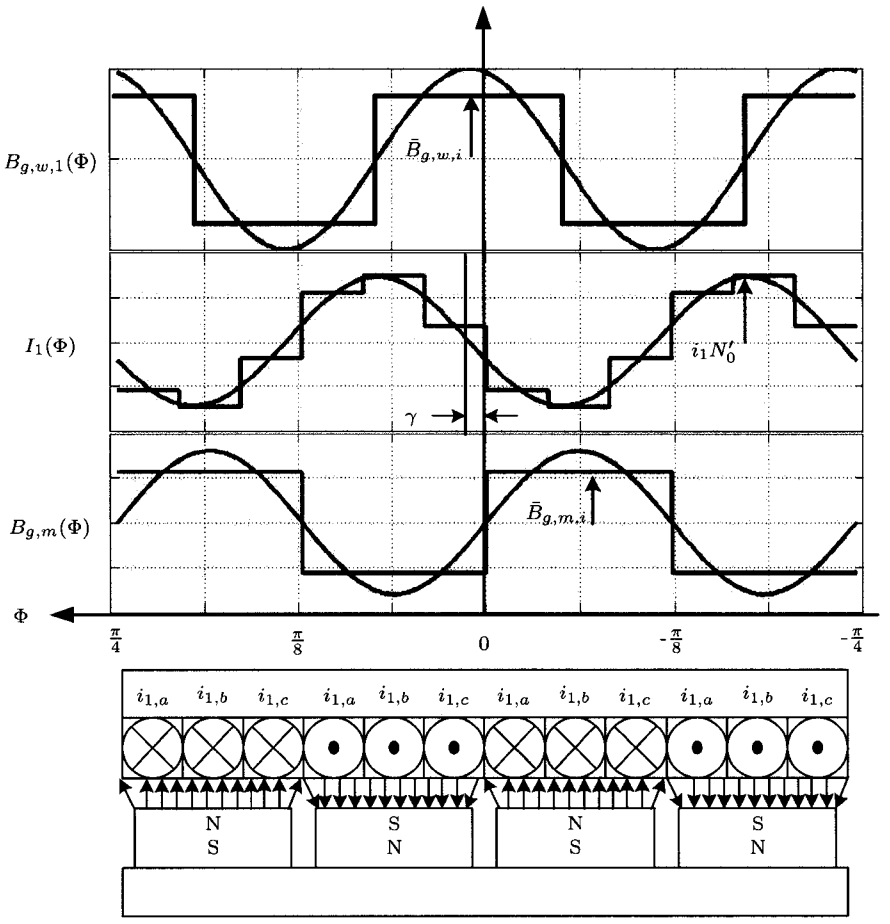

Figure 5.4: Unwrapped geometry of the toothless self-bearing servomotor showing the current distribution and air-gap flux density waveforms in Segment 1 as a function of the stator angle Φ. Here it is assumed that the rotor position $(x, y, \theta) = 0$ for simplicity. The permanent magnets (PMs) are assumed to generate a uniform flux density across the air gap (as depicted by the flux lines in the bottom of the picture), of which the magnitude $\bar{B}_{g,m,i}$ is approximated by magnetic circuit analysis. The square wave function is approximated as sinusoidal so that a continuous flux density distribution $B_{g,m}$ results. The PM flux interacts with the current distribution I_1 based on the assumption of sinusoidally distributed windings. The sinusoidal distribution approximates a step-wise current distribution that results from the fact that the windings of the TSBS are actually concentrated. Finally, the windings themselves are a source of air gap flux density, whose magnitude $\bar{B}_{g,w,i}$ is likewise determined from circuit analysis, and whose continuous approximation $B_{g,w,1}$ is displaced $\pi/2$ radE with respect to I_1. The phase angle γ denotes an offset between the current distribution and the PM flux distribution. This phase offset γ is studied in Chapter 6.

flux density in the air gap can be ignored, then the mechanical stress (5.11) expressed in cylindrical coordinates is

$$T = \begin{bmatrix} T_{R,R} \\ T_{\Phi,R} \\ 0 \end{bmatrix} = \begin{bmatrix} \frac{B_g^2}{2\mu_0} \\ -B_g \frac{I}{r} \\ 0 \end{bmatrix} \tag{5.12}$$

where $T_{R,R}$ is the *normal stress*, $T_{\Phi,R}$ is the *shear stress*, and mechanical stress perpendicular to the cross section of the rotor does not occur since no axial component of magnetic flux is assumed. The radially directed component of flux density B_g is simply the sum of air-gap flux densities contributed by the PMs and the stator windings, i.e.

$$B_g = B_{g,m} + B_{g,w}.$$

The radius to the inner stator surface is r, and I is the current distribution on the inner stator surface approximated as a thin current sheet.

The radial forces and torque acting on the rotor are determined by a integrating the normal and shear stresses over the cylindrical stator surface S. The total normal and tangential force components are given by

$$F_R = \iint_S T_{R,R} \mathrm{d}S = r \int_{z=0}^{L} \int_{\Phi=0}^{2\pi} T_{R,R} \mathrm{d}\Phi \mathrm{d}z = rL \int_0^{2\pi} T_{R,R} \mathrm{d}\Phi,$$

$$F_\Phi = \iint_S T_{\Phi,R} \mathrm{d}S = r \int_{z=0}^{L} \int_{\Phi=0}^{2\pi} T_{\Phi,R} \mathrm{d}\Phi \mathrm{d}z = rL \int_0^{2\pi} T_{\Phi,R} \mathrm{d}\Phi,$$

where L is the axial length of the TSBS. The x and y axis components of force as well as torque are obtained from

$$\begin{aligned} F_x &= F_R \cos\Phi - F_\Phi \sin\Phi \\ &= rL \int_0^{2\pi} T_{R,R} \cos\Phi \mathrm{d}\Phi - rL \int_0^{2\pi} T_{\Phi,R} \sin\Phi \mathrm{d}\Phi, \end{aligned} \tag{5.13a}$$

$$\begin{aligned} F_y &= F_R \sin\Phi + F_\Phi \cos\Phi \\ &= rL \int_0^{2\pi} T_{R,R} \sin\Phi \mathrm{d}\Phi + rL \int_0^{2\pi} T_{\Phi,R} \cos\Phi \mathrm{d}\Phi, \end{aligned} \tag{5.13b}$$

$$\tau = r^2 L \int_0^{2\pi} T_{\Phi,r} \mathrm{d}\Phi. \tag{5.13c}$$

Substituting the normal and shear stress expressions from (5.12) into (5.13) gives

$$\begin{aligned}
F_x &= \frac{rL}{2\mu_0}\int_0^{2\pi} B_g^2(\Phi)\cos\Phi \mathrm{d}\Phi + L\int_0^{2\pi} B_g(\Phi)I(\Phi)\sin\Phi \mathrm{d}\Phi \\
&= F_{x,M} + F_{x,L}, \\
F_y &= \frac{rL}{2\mu_0}\int_0^{2\pi} B_g^2(\Phi)\sin\Phi \mathrm{d}\Phi - L\int_0^{2\pi} B_g(\Phi)I(\Phi))\cos\Phi \mathrm{d}\Phi \\
&= F_{y,M} + F_{y,L}, \\
\tau &= -rL\int_0^{2\pi} B_g(\Phi)I(\Phi)\mathrm{d}\Phi.
\end{aligned}$$

The tangential force components $F_{x,L}, F_{y,L}$ are Lorentz forces expressed in integral form. It is the Lorentz force that is the basis for levitation and torque. More precisely, we calculate the Lorentz forces and torque by

$$F_{x,L}(x,y,\theta,i_k) = L\sum_{k=1}^{4}\int_{l_k}^{u_k} B_{g,m}(\Phi)I_k(\Phi)\sin\Phi \mathrm{d}\Phi, \tag{5.14a}$$

$$F_{y,L}(x,y,\theta,i_k) = -L\sum_{k=1}^{4}\int_{l_k}^{u_k} B_{g,m}(\Phi)I_k(\Phi)\cos\Phi \mathrm{d}\Phi, \tag{5.14b}$$

$$\tau(x,y,\theta,i_k) = -rL\sum_{k=1}^{4}\int_{l_k}^{u_k} B_{g,m}(\Phi)I_k(\Phi)\mathrm{d}\Phi, \tag{5.14c}$$

with the limits of integration defined by $l_k = k\pi/2 - 3\pi/4$ and $u_k = k\pi/2 - \pi/4$.

The normal force components $F_{x,M}, F_{y,M}$ are Maxwell, or reluctance, forces which are destabilizing because they tend to draw the rotor towards the stator. More precisely, $F_{x,M}, F_{y,M}$ are computed from the integrals

$$F_{x,M}(x,y,\theta,i_k) = \frac{rL}{2\mu_0}\sum_{k=1}^{4}\int_{l_k}^{u_k}(B_{g,m}(\Phi) + B_{g,w,k}(\Phi))^2\cos\Phi \,\mathrm{d}\Phi, \tag{5.15a}$$

$$F_{y,M}(x,y,\theta,i_k) = \frac{rL}{2\mu_0}\sum_{k=1}^{4}\int_{l_k}^{u_k}(B_{g,m}(\Phi) + B_{g,w,k}(\Phi))^2\sin\Phi \,\mathrm{d}\Phi. \tag{5.15b}$$

In order to evaluate the expressions for the integrals in (5.14)-(5.15) we make the harmonic approximation

$$\frac{m_1}{m_2 - x\cos\Phi - y\sin\Phi} \approx \frac{m_1}{m_2}\left(1 + \frac{x\cos\Phi}{m_2} + \frac{y\sin\Phi}{m_2}\right), \tag{5.16}$$

which is good under the assumption that $x^2 + y^2 \ll m_2^2$. This is a reasonable assumption in practice since m_2 approximately represents the magnetic air gap, i.e. the PMs, winding region and mechanical air gap. The magnetic air gap is large in a toothless machine, and the rotor's displacement is limited to only a very small fraction of that by the touchdown bearings.

5.2.4 Reduction of control currents

Evaluating (5.14)-(5.14) at the home rotor position $(x, y, \theta) = 0$ gives

$$F_{x,L} = \frac{\sqrt{2}LN_0'P^2m_1}{(P^2-1)m_2} \cdot \frac{i_4 - i_2}{2}, \tag{5.17a}$$

$$F_{y,L} = \frac{\sqrt{2}LN_0'P^2m_1}{(P^2-1)m_2} \cdot \frac{i_1 - i_3}{2}, \tag{5.17b}$$

$$\tau = \frac{\pi r LN_0'm_1}{m_2} \cdot \frac{i_1 + i_2 + i_3 + i_4}{4}, \tag{5.17c}$$

where $P = 2M$ denotes the number of PM poles. Equation (5.17) is only valid for positive integer multiples of 4 for M because it results in an even number of poles in each segment. Equation (5.17) also confirm our earlier assertion that, in this ideal scenario, only Segments 2 and 4 determine the x-axis force and only Segments 1 and 3 determine the y-axis force.

It is evident that $F_{x,L}, F_{y,L}$ and τ can be obtained in a non-unique way from the control currents i_k, $1 \leqslant k \leqslant 4$ since the control degrees of freedom exceed the mechanical degrees of freedom. A transformation is sought that yields individual control of force and torque with new inputs i_x, i_y and i_θ. Such a transformation can be obtained by setting

$$\begin{aligned} \frac{i_4 - i_2}{2} &= i_x, \\ \frac{i_1 - i_3}{2} &= i_y, \\ \frac{i_1 + i_2 + i_3 + i_4}{4} &= i_\theta. \end{aligned}$$

To obtain a unique solution, we impose a constraint on the balance of torque generated by the x-axis currents, i_2, i_4, and by the y-axis currents, i_1, i_3. This constraint can be expressed as

$$\frac{i_1 + i_3}{4} = \lambda i_\theta, \quad 0 \leq \lambda \leq 1$$

where λ is defined as the fraction of total torque generated by the y-axis currents. Thus, the input transformation is

$$i_1 = 2\lambda i_\theta + i_y, \tag{5.18a}$$

$$i_2 = 2(1-\lambda) i_\theta - i_x, \tag{5.18b}$$

$$i_3 = 2\lambda i_\theta - i_y, \tag{5.18c}$$

$$i_4 = 2(1-\lambda) i_\theta + i_x. \tag{5.18d}$$

Setting $\lambda = 1/2$ means equal torque generation from each quadrant and was the intuitive choice originally proposed in [120]. Nonetheless, λ is a potentially useful degree of freedom for control which will get exploited in Chapter 6. By substituting (5.18) into (5.17),

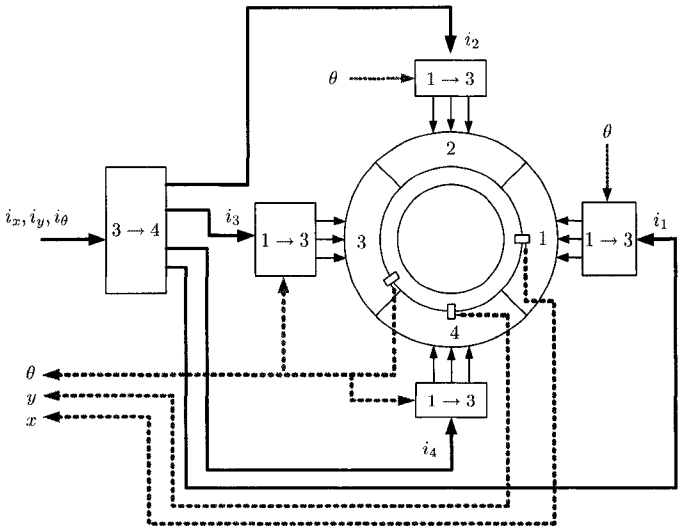

Figure 5.5: Plant schematic. Twelve physical inputs (the current for each of the twelve phases), are effectively controlled by the three virtual inputs i_x, i_y, i_θ. The 3-to-4 transformation is given by (5.18), and the 1-to-3 transformations are given by (5.3).

independent of the choice of λ, we get

$$F_{x,L} = \frac{\sqrt{2}LN_0'P^2m_1}{(P^2-1)m_2} i_x,$$
$$F_{y,L} = \frac{\sqrt{2}LN_0'P^2m_1}{(P^2-1)m_2} i_y,$$
$$\tau = \frac{\pi r LN_0'm_1}{m_2} i_\theta$$

which decouple force and torque. Decoupling simplifies the control and the dynamic model becomes square, i.e. where input and output dimensions are equal, such that it is amenable to decentralized control design. Figure 5.5 illustrates the plant schematically under the input transformation.

5.2.5 General expressions

We now give the complete force and torque expressions in the general case where the rotor is not in the home position, i.e. $(x, y, \theta) \neq 0$. Evaluation[1] of the Lorentz integrals (5.14)

[1] In the general case where $(x, y, \theta) \neq 0$, the integrals are evaluated with the aid of a symbolic mathematical package. These calculations can be obtained from the author by request.

yields

$$F_{x,L} = \frac{\sqrt{2}LN_0'm_1\left(P^2-1+\cos(P\theta)\right)}{(P^2-1)m_2}i_x - \frac{\sqrt{2}PLN_0'm_1\sin(P\theta)}{(P^2-1)m_2}i_y - \frac{\pi LN_0'm_1 y}{2m_2^2}i_\theta, \tag{5.19a}$$

$$F_{y,L} = \frac{\sqrt{2}LN_0'm_1\left(P^2-1+\cos(P\theta)\right)}{(P^2-1)m_2}i_y + \frac{\sqrt{2}PLN_0'm_1\sin(P\theta)}{(P^2-1)m_2}i_x + \frac{\pi LN_0'm_1 x}{2m_2^2}i_\theta, \tag{5.19b}$$

$$\tau = \frac{\pi rLN_0'm_1}{m_2}i_\theta + \frac{\sqrt{2}rLN_0'm_1[P\sin(P\theta)x-(P^2-1+\cos(P\theta))y]}{(P^2-1)m_2^2}i_x + \frac{\sqrt{2}rLN_0'm_1[P\sin(P\theta)y+(P^2-1+\cos(P\theta))x]}{(P^2-1)m_2^2}i_y. \tag{5.19c}$$

The Lorentz forces (5.19) are nonlinear, fully coupled, and characterized by their linear dependence on the control currents i_x, i_y and i_θ. Rotor-angle-dependent cross-coupling is apparent; there is also an orthogonal position dependence when torque is being generated, i.e. $F_{x,L}, F_{y,L}$ are functions of y, x respectively when $i_\theta \neq 0$. This can be physically explained by the fact that an eccentric rotor strengthens the Lorentz force in one segment (e.g. Segment 3) and correspondingly weakens that of the opposite segment (i.e. Segment 1) if equal currents are applied to each. Since i_θ is applied equally to opposing segments, then a radial force will accompany rotor eccentricity.

Evaluating the Maxwell integrals (5.15) results in lengthy force expressions. The Maxwell forces are physically representative of the magnetic attraction between the rotor and stator. These force are not being usefully exploited, and are in fact destabilizing because their tendency is to pull the rotor away from the center of the stator. The most significant components of Maxwell forces are the negative stiffness terms

$$F_{x,PM} = \frac{\pi rLm_1^2}{2\mu_0 m_2^3}x, \tag{5.20a}$$

$$F_{y,PM} = \frac{\pi rLm_1^2}{2\mu_0 m_2^3}y. \tag{5.20b}$$

The term *negative stiffness* comes from the fact that the linear force-displacement relationships in (5.20) are opposite to the restoring force-displacement relationship of a traditional spring. This negative stiffness is due to the PMs being attracted to the stator back iron. Maxwell force terms also result from the winding flux attracting the rotor back iron. For

the centered rotor these additional forces are

$$F_{x,W_1} = \frac{\sqrt{2}rLw_1^2\left[(P^2-1-\cos(P\theta))i_y i_\theta - P\sin(P\theta)i_x i_\theta\right]}{\mu_0(P^2-1)w_2^2}, \tag{5.21a}$$

$$F_{y,W_1} = \frac{\sqrt{2}rLw_1^2\left[(\cos(P\theta)-P^2+1)i_x i_\theta - P\sin(P\theta)i_y i_\theta\right]}{\mu_0(P^2-1)w_2^2}. \tag{5.21b}$$

The forces (5.21) are termed *center-rotor side pull* [120]. As expected, these forces are quadratic in current, similar to the force principle behind AMBs. In addition, center-rotor side pull only occurs when torque is generated. This is sensible because for opposing segments, e.g. Segments 1 and 3, i_θ is analogous to a bias current and i_y is analogous to a differential current since $i_1 = 2\lambda i_\theta + i_y, i_3 = 2\lambda i_\theta - i_y$. If $i_\theta = 0$ then opposite currents are applied to opposing segments, e.g. $i_1 = -i_3$, the corresponding Maxwell forces cancel. If $i_\theta \neq 0$, then a net Maxwell force will result along the x axis.

For an off-center rotor, the remaining Maxwell force terms due to winding flux attraction are[2]

$$F_{x,W_2} = \frac{\pi rLw_1^2 x}{2\mu_0 w_2^3}i_\theta^2 + \frac{rLw_1^2}{2\mu_0 w_2^3}\left(\frac{(\pi+2)x}{2} - \frac{x\cos(P\theta)+My\sin(P\theta)}{M^2-1}\right)i_y^2 + \frac{rLw_1^2}{2\mu_0 w_2^3}\left(\frac{(\pi-2)x}{2} + \frac{x\cos(P\theta)+My\sin(P\theta)}{M^2-1}\right)i_x^2, \tag{5.22a}$$

$$F_{y,W_2} = \frac{\pi rLw_1^2 y}{2\mu_0 w_2^3}i_\theta^2 + \frac{rLw_1^2}{2\mu_0 w_2^3}\left(\frac{(\pi+2)y}{2} - \frac{y\cos(P\theta)-Mx\sin(P\theta)}{M^2-1}\right)i_x^2 + \frac{rLw_1^2}{2\mu_0 w_2^3}\left(\frac{(\pi-2)y}{2} + \frac{y\cos(P\theta)-Mx\sin(P\theta)}{M^2-1}\right)i_y^2. \tag{5.22b}$$

The Maxwell forces (5.22) have components that are individually quadratic in each of the control currents. Finally, the Maxwell force integrals produce cross terms from multiplication of $B_{g,m}$ and $B_{g,w,k}$. The cross terms are

$$F_{x,X} = -\frac{\sqrt{2}rLm_1w_1\left(P\cos(P\theta)i_x - \sin(P\theta)i_y\right)}{\mu_0(P^2-1)m_2w_2}, \tag{5.23a}$$

$$F_{y,X} = -\frac{\sqrt{2}rLm_1w_1\left(P\cos(P\theta)i_y + \sin(P\theta)i_x\right)}{\mu_0(P^2-1)m_2w_2}. \tag{5.23b}$$

The cross terms are interesting in that they are linearly dependent and constructively interfere with the rotor-angle-dependent cross-coupling terms in the Lorentz-force expressions. The total forces F_x, F_y are the sum of terms (5.19)-(5.23),

$$F_x = F_{x,L} + F_{x,PM} + F_{x,W_1} + F_{x,W_2} + F_{x,X}, \tag{5.24a}$$

$$F_y = F_{y,L} + F_{y,PM} + F_{y,W_1} + F_{y,W_2} + F_{y,X}, \tag{5.24b}$$

and the only contribution to torque is from (5.17c).

[2]Maxwell force terms with a quadratic position dependence are significantly outweighed by terms having a linear position dependence and are thus ignored.

5.2.6 General model structure

We may obtain a more compact formulation of (5.24) by additional modeling approximations and grouping of like terms. Specifically we assume that $P^2 - 1 \gg \cos(P\theta)$ and $(\pi \pm 2)/2 \gg \cos(P\theta)/(M^2 - 1)$. Applying these approximations to (5.24) gives

$$F_x = [\alpha_1 - \alpha_2 \cos(P\theta)]i_x - \alpha_3 \sin(P\theta)i_y - \alpha_4 y i_\theta + \alpha_5 x + \alpha_6 i_y i_\theta - \alpha_7 \sin(P\theta)i_x i_\theta + \alpha_8 x[2\pi i_\theta^2 + (\pi + 2)i_y^2 + (\pi - 2)i_x^2] + \alpha_9 y \sin(P\theta)(i_x^2 - i_y^2), \tag{5.25a}$$

$$F_y = [\alpha_1 - \alpha_2 \cos(P\theta)]i_y + \alpha_3 \sin(P\theta)i_x + \alpha_4 x i_\theta + \alpha_5 y - \alpha_6 i_x i_\theta - \alpha_7 \sin(P\theta)i_y i_\theta + \alpha_8 y[2\pi i_\theta^2 + (\pi + 2)i_x^2 + (\pi - 2)i_y^2] + \alpha_9 x \sin(P\theta)(i_x^2 - i_y^2), \tag{5.25b}$$

$$\tau = \beta_1 i_\theta + \beta_2(x i_y - y i_x) + \beta_3(x i_x + y i_y)\sin(P\theta), \tag{5.25c}$$

for constant parameters α_i, $1 \leqslant i \leqslant 9$, and β_j, $1 \leqslant j \leqslant 3$. In the sequel, we identify these parameters and obtain a simplified version of (5.25) by discriminating between significant and insignificant terms in the model.

In the following discussion, we will refer to specific terms of the force and torque expressions based on the subscript of the parameter associated with the term. For example, *force Term 2* refers to both $\alpha_2 \cos(P\theta)i_x$ and $\alpha_2 \cos(P\theta)i_y$.

5.3 Parameter identification

The coefficients α_i, β_j from (5.25) are constants which are dependent upon previously defined parameters. We cannot, however, determine the values of α_i, β_j with sufficient accuracy on a purely analytical basis. The main reason for this is the motor's geometry. Specifically, well-defined paths for uniform flux flow do not exist in a toothless motor. In addition, force and torque contributions may exist from tangential flux. Therefore, we may only coarsely approximate $R_m, R_w, R_g, A_g, C_\phi$ and K_ℓ. In practice, uncertainty in the value of these parameters inevitably arises. For example, it is difficult to model actual PMs due to their multi-valued material property, and the motor construction process creates irregularities in the geometry and the windings. Instead, we estimate the parameters by empirical means and employ identification techniques, i.e. curve fitting. Due to the linear parameterization of (5.25), we use linear, i.e. ordinary, least squares to obtain a global solution to the curve fit. FEA data can be conveniently employed for this task.

From FEA we obtain a force and torque data set

$$(F_x[1], F_y[1], \tau[1], \ldots, F_x[K], F_y[K], \tau[K])$$

from a sufficiently informative set of operating points $(\xi[1], \ldots, \xi[K])$ where

$$\xi[k] = (x[k], y[k], \theta[k], i_x[k], i_y[k], i_\theta[k])$$

and $1 \leqslant k \leqslant K$, K being the size of the data set. An informative data set ensures that we may discriminate between all significant terms in our force and torque expressions and that a numerically well-conditioned solution exists [72]. Linear least squares estimates parameters via pseudo matrix inversion so as to minimize the sum of squares of differences between the predicted and actual data points (in this case, the difference between the simulated and analytical force and torque). The underlying assumptions of this technique are that the model is correct and that the errors between the model predictions and the data points are, statistically speaking, uncorrelated, have zero mean, and a constant variance. To demonstrate, consider that we are calibrating the torque model. The parameters $\Theta = (\beta_1, \beta_2, \beta_3)^{\mathrm{T}}$ are estimated by $\hat{\Theta} = (\Phi^{\mathrm{T}}\Phi)^{-1}\Phi^{\mathrm{T}}U$ where $\hat{\Theta}$ is the parameter estimate, $U = (\tau[1], \ldots, \tau[K])^{\mathrm{T}}$ and $\Phi = [\Phi_1\ \Phi_2\ \Phi_3]$ such that

$$\Phi_1 = (i_\theta[1], \ldots, i_\theta[K])^{\mathrm{T}},$$

$$\Phi_2 = ((xi_y - yi_x)[1], \ldots, (xi_y - yi_x)[K])^{\mathrm{T}},$$

$$\Phi_3 = ((xi_x + yi_y)\sin(P\theta)[1], \ldots (xi_x + yi_y)\sin(P\theta)[K])^{\mathrm{T}}.$$

Since the general model has twelve parameters to be identified, it is desirable to reduce this number by retaining only the terms associated with parameters which noticeably improve the model fit-to-data. Pragmatically, we consider a set of candidate model structures, specifically models with a reduced number of terms, and evaluate each model by its average squared prediction error $e^{\mathrm{T}}e/K$ where $e = U - \Phi\hat{\Theta}$ defines the prediction error.

5.4 Finite element analysis

FEA data is utilized for parameter identification and to test the quality of the resultant model. The reason for this is that FEA simulates more complex phenomena that is not explicitly modeled, such as tangential flux flow and saturation of the iron. Furthermore, FEA provides a convenient basis to compare the quality of our model to other TSBS modeling efforts based on a 2D flux model [103]. These results are shown at the end of this chapter.

The FEA solutions are based on the TSBS geometry depicted in Figure 5.6 and is representative of an experimental TSBS at the University of Alberta that was built by Airex Corporation (Somersworth, NH). The depicted TSBS has sixteen PM poles and the winding stations are modeled as solid conductors. A quantitative description of material and geometric properties is given in Table 5.1.

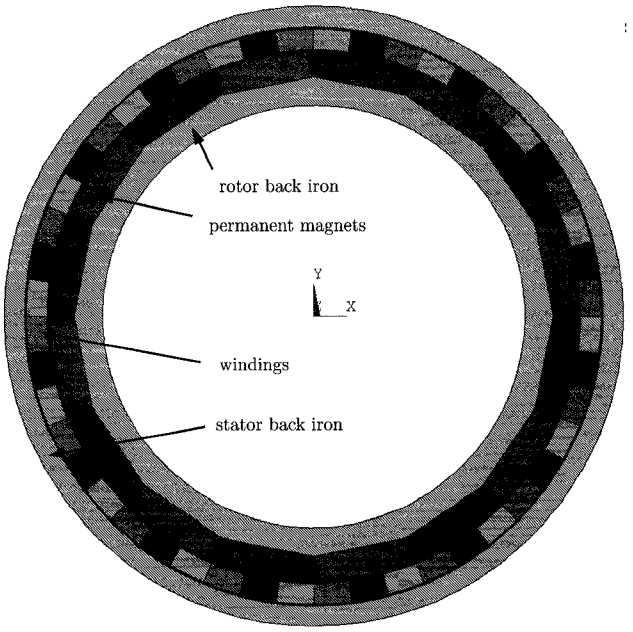

Figure 5.6: finite element analysis (FEA) geometry for a sixteen-pole TSBS. A solid model was developed in Pro/Engineer from which geometry was exported to the FEA software ANSYS (courtesy of C. Forbrich).

Parameter	Value	Parameter	Value
windings/station	40	winding thickness	6.2 mm
length (L)	74.2 mm	nominal air gap (g_0)	0.9 mm
rotor ID	126.4 mm	rotor iron thickness	7.1 mm
PM remanence (B_r)	1.3 T	stator iron thickness	6.1 mm
PM thickness	8.6 mm	PM width	27.0 mm
steel material	Carbon 1026	PM material	Nd-Fe-B N44H

Table 5.1: Geometrical and material parameters of a simulated toothless, self-bearing servomotor (TSBS). The TSBS is simulated using finite element analysis, and its geometry is shown in Figure 5.6.

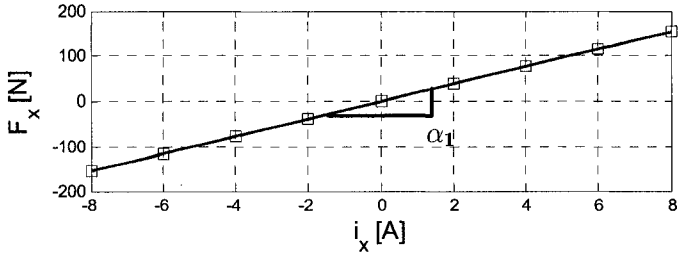

Figure 5.7: Average bearing capacity: $\xi = (0, 0, \pi/32 \text{ rads}, i_x, 0, 0)$.

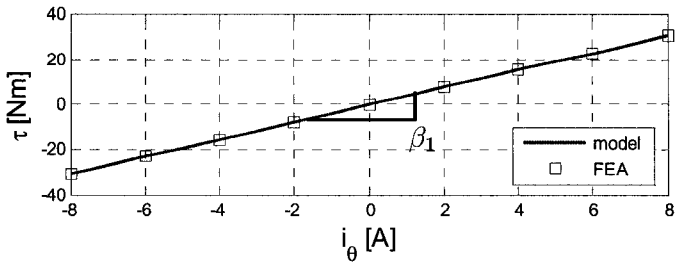

Figure 5.8: Average torque capacity: $\xi = (0, 0, \pi/48 \text{ rads}, 0, 0, i_\theta)$.

Each FEA solution corresponds to the force and torque generated at the operating point $\xi = (x, y, z, i_x, i_y, i_\theta)$. By proper choice of operating points we are able to isolate most of the individual force and torque terms and thus identify the corresponding coefficient. This brings to light the key force and torque characteristics of the TSBS, namely the static capacity, ripple, and displacement sensitivity. Figures 5.7-5.13 present some identification data. Figures 5.7-5.8 plot the average static bearing force and torque capacities for the operating points $\xi = (0, 0, \pi/32 \text{ rads}, i_x, 0, 0)$ and $\xi = (0, 0, \pi/48 \text{ rads}, 0, 0, i_\theta)$ respectively. From this we identify the direct force constant α_1 and torque constant β_1. Linearity is confirmed over the operating regime, however note that due to the common coil winding scheme, the demands for bearing force and torque must be shared. Since α_1, β_1 are averaged over an electrical period of the motor, in Figures 5.9-5.10 we investigate how significant the force and torque variation is with respect to rotor angle θ. Figure 5.9 shows the direct and coupled force ripple for the case of $\xi = (0, 0, \theta, 1 \text{ A}, 0, 0)$, whereby we identify the direct force ripple amplitude α_2 and orthogonal force ripple amplitude α_3. Both α_2 and α_3 are less than 10% of the average, but could be potentially significant If unbalanced radial loading conditions exist, e.g. if $i_x \gg i_y$. Encouragingly, Figure 5.9 confirms that the sinusoidal approximation in our modeling is fairly accurate in characterizing the ripple waveform.

Figure 5.10 depicts the torque ripple for $\xi = (0, 0, \theta, 0, 0, 1 \text{ A})$. While the nominal torque model (5.25c) theoretically predicts no cogging for a centered rotor, a ripple appears that is periodic with the winding station pitch. As discussed in prior work [102], the waveform is mainly characterized by a third harmonic resulting from the existence of concentrated windings, as opposed to the initial assumption of sinusoidally distributed ones. To confirm that this is in fact the case, we augment the torque model with a fourth term, i.e.

$$\tau = \beta_1 i_\theta + \beta_2(x i_y - y i_x) + \beta_3(x i_x + y i_y)\sin(P\theta) + \beta_4 \cos(3P\theta) i_\theta.$$

Figure 5.10 shows a modeled torque waveform accounting for the effect of concentrated

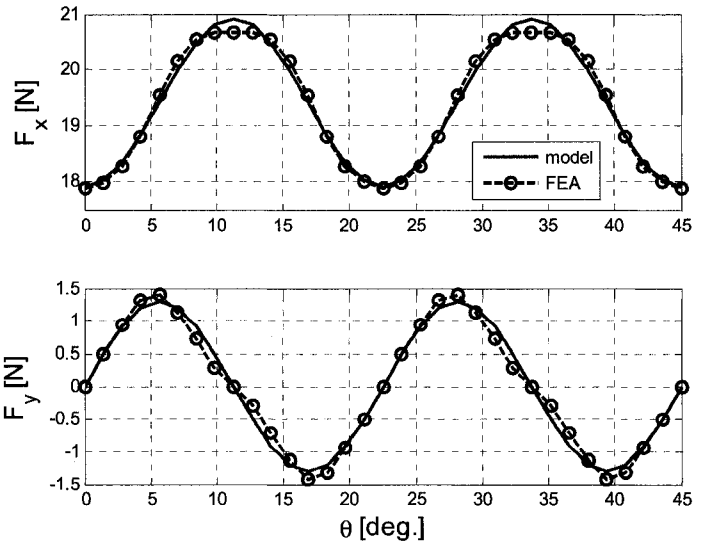

Figure 5.9: Centered-rotor force ripple: $\xi = (0, 0, \theta, 1 \text{ A}, 0, 0)$. Amplitude of F_x waveform is α_2 and the amplitude of F_y waveform is α_3. Radial force coupling with rotor angle dependence is apparent.

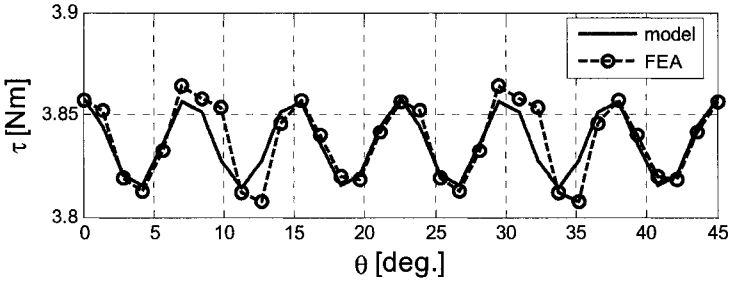

Figure 5.10: Torque ripple: $\xi = (0, 0, \theta, 0, 0, 1 \text{ A})$. Amplitude of waveform is β_4.

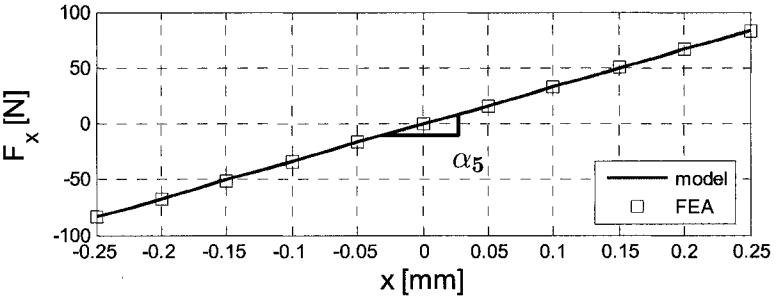

Figure 5.11: Negative stiffness: $\xi = (x, 0, 0, 0, 0, 1 \text{ A})$.

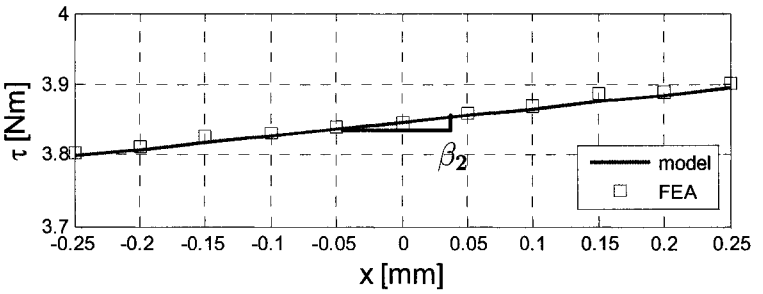

Figure 5.12: Torque displacement sensitivity: $\xi = (x, 0, \pi/32 \text{ rads}, 1 \text{ A}, 1 \text{ A}, 1 \text{ A})$.

windings. Modeling this effect does visibly improve the fit, but it is not practically necessary in this particular example as the ripple is extremely small ($< 1\%$). Moreover, the modeled cogging torque associated with rotor eccentricity, torque Term 2, does not appear to be significant as well.

Figure 5.11 displays the motor's displacement sensitivity for $\xi = (x, 0, 0, 0, 0, 1 \text{ A})$. The direct displacement sensitivity is significant and dominated by force Term 5, the PM attraction to the stator back iron. Superimposed, and less significant is force Term 8, which is representative of rotor attraction to the windings. Figure 5.13 shows the force produced by center-rotor side pull (force Term 6) in isolation. The large magnetic air gap of the TSBS appears to render Maxwell force contributions from to winding flux relatively insignificant. Orthogonal displacement sensitivity due to the Lorentz force is too small to register over the actual motor's allowable range of motion and operating currents, and therefore it is not shown. Figure 5.12 shows the torque displacement sensitivity for $\xi = (x, 0, \pi/32 \text{ rads}, 1 \text{ A}, 1 \text{ A}, 1 \text{ A})$. This dependence only becomes a significant effect in extreme operating conditions, e.g. $i_x, i_y \gg i_\theta$ and the rotor is far off center.

A total of $K = 175$ operating points comprise the identifying data set. To reduce the complexity of the model (5.25), we consider approximate force and torque expressions with a reduced number of terms. These approximations are evaluated based on their prediction error and some examples are listed in Table 5.2 alongside their corresponding average prediction error. The comparison of force models ultimately indicated that the majority of data is characterized by force Terms 1, 2, 3, 5, and 6. All of the remaining force terms yielded less than 0.1% reduction in the prediction error.

A comparison of torque models shows that each of the four terms yields a perceptible improvement in modeling the data, which is shown in Figure 5.15. Torque Term 3, however, yields only a marginal improvement in the torque prediction error. Hence, the modeled

force and torque curves presented in Figures 5.7-5.14 are based on force Terms 1,2,3,5 and 6 and torque Terms 1,2 and 4. The values of these identified parameters are given in Table 5.3.

Although the identified model is shown to align well with the chosen estimation data set, a good test of the model is to compare its prediction of force and torque to to that from FEA for operating points not used to identify α_i, β_j. Tables 5.4-5.6 present a validation data set. These Tables are adapted from [102], in which PDE modeling of a 24-pole TSBS is considered. For each operating point, we give the FEA solutions to force and torque alongside what is predicted by the identified model. The third and fourth columns under each of F_x, F_y and τ compare the prediction error for a 2D flux-based model of [102] to the prediction error of our identified model. The comparison shows that our identified model provides similar accuracy to that of a more complex PDE model. While the result of [102] is based on a 24-pole TSBS, it would be reasonable to expect similar accuracy on a 16-pole TSBS such as ours since the design and material properties are similar. As further validation, Figures 5.14-5.15 presents force and torque ripple waveforms for the more complex operating point $\xi = (-0.2 \text{ mm}, 0, \theta, 5 \text{ A}, 2 \text{ A}, 1 \text{ A})$. The model predictions align reasonably well.

In summary, our results suggests that a force and torque model based on a 1D flux distribution with identified parameters can achieve a comparable level of accuracy to a model based on a 2D distribution. Having taken a semi-analytic approach, i.e. combining analytical and identification techniques, to obtain a model we avoid the complexity associated with developing a model on a purely analytical basis [103, 102]. We remark that although the FEA geometry being studied is representative of an experimental TSBS, we were not testing the absolute accuracy of the model in identifying parameters. FEA provided a convenient basis for comparison, and tested the quality of the model structure. With that being said, the parameters identified from FEA provide reasonable estimates of actual values and is therefore a starting point for controller development.

In principle, our modeling efforts provide new avenues to explore in the way of control system design. For example, our nonlinear model retains rotor angle dependence, unlike the linearized models previously put forth. In practice, whether nonlinear compensation of the TSBS is necessary depends on the actual system. In the case study just considered, rotor-angle-dependent cross-coupling as well as winding-flux-induced Maxwell forces do not appear to be significant. As such, we develop a dynamic model in the next chapter based on further simplification of the force and torque expressions, and employ experimental means

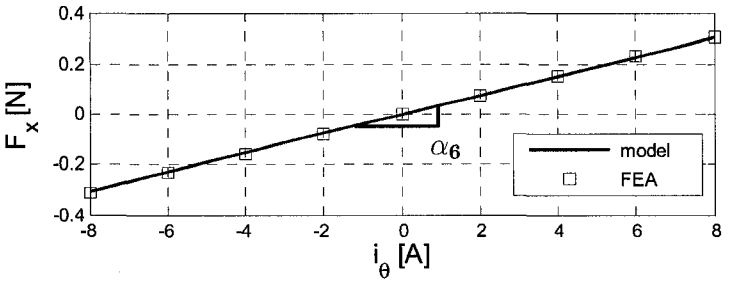

Figure 5.13: Centered-rotor side pull: $\xi = (0, 0, 0, 0, 1\text{ A}, i_\theta)$.

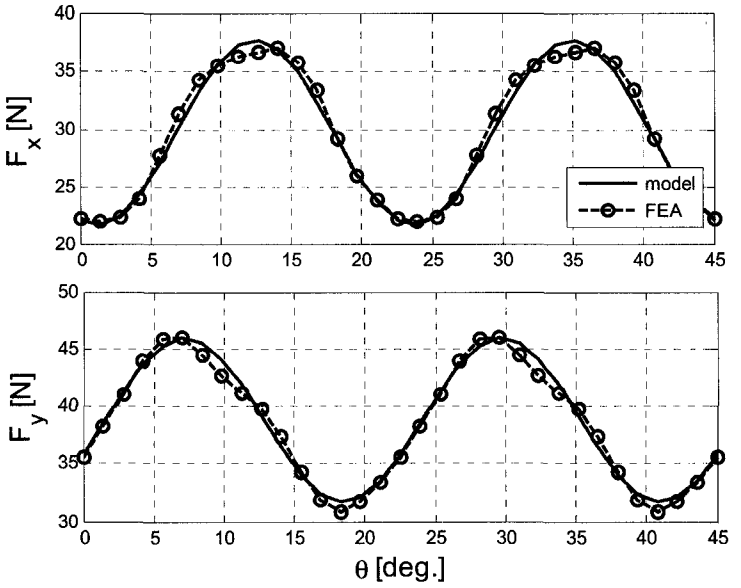

Figure 5.14: Validation force data: $\xi = (-0.2\text{ mm}, 0, \theta, 5\text{ A}, 2\text{ A}, 1\text{ A})$.

to identify parameters. From our modeling efforts, however, we see potential in exploiting the additional control variables, in particular the phase offset γ and the torque distribution parameter λ.

5.5 Conclusions

A bearing force and torque model is presented for a toothless self-bearing servomotor based on analytic and identification techniques. The analytic modeling is based on a 1D magnetic flux distribution, and a complete characterization yields coupled, nonlinear expressions. We abstract the general model structure and identify the parameters via linear least squares. In addition to identifying parameters, we acquire a more compact model by identifying and

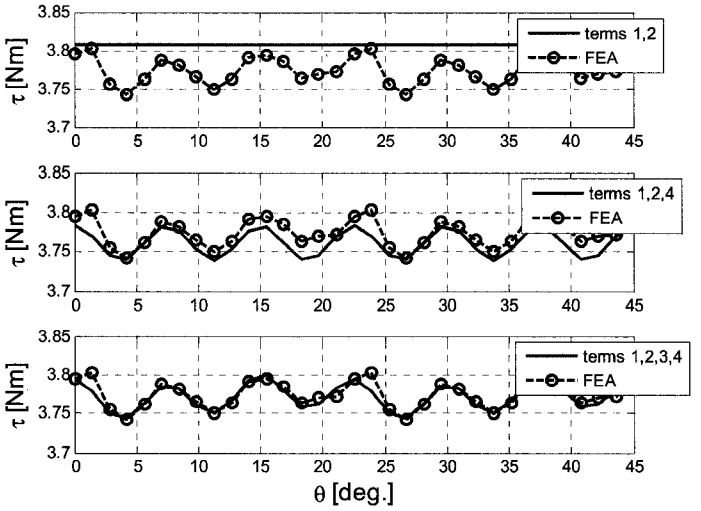

Figure 5.15: Validation torque data: $\xi = (-0.2 \text{ mm}, 0, \theta, 5 \text{ A}, 2 \text{ A}, 1 \text{ A})$.

Force		**Torque**	
included terms	$(e^{\mathrm{T}}e)/K$	included terms	$(e^{\mathrm{T}}e)/K$
$1, 2, 3, 5$	0.0945 N^2	1,2	0.0015 $(\text{N-m})^2$
$1, 2, 3, 5, 6$	0.0791 N^2	1,2,4	1.31e-4 $(\text{N-m})^2$
$1-9$	0.0791 N^2	1-4	1.30e-4 $(\text{N-m})^2$

Table 5.2: Comparison of identified force and torque models. It is evident that numerous terms from the general force and torque model (5.25) do not significantly reduce the prediction error. These terms which do not significantly reduce the prediction error are disregarded.

Force			**Torque**		
Parameter	Value	Units	Parameter	Value	Units
α_1	19.36	N/A	β_1	3.85	N·m/A
α_2	1.50	N/A	β_2	185.19	N/A
α_3	1.29	N/A	β_4	0.02	N·m/A
α_5	334.23	N/mm			
α_6	0.04	N/A^2			

Table 5.3: Identified force and torque parameters. The parameters retained were those associated with terms that improve the fit-to-data, based on the results of Table 5.2.

Operating Point						F_x(N)			
i_x [A]	i_y [A]	i_θ [A]	x [mil]	y [mil]	θ [deg.]	FEA	model	%error	%error[102]
0	0	2	0	0	0	0.00	0.00	-	-
3	0	0	0	0	0	53.51	53.55	0.08	0.58
0.5	1.5	0	0	0	0	8.92	8.93	0.09	0.58
0	1	2	0	0	0	0.08	0.08	0.00	2.27
0	0.2	0.5	0	0	0	0.00	0.00	0.00	0.58
2	1.5	0.5	0	0	0	35.70	35.73	0.07	0.58
2	1.5	0.5	0	0	11.25	41.25	41.75	1.21	0.37
0	0	0	-20	0	0	-170.61	-170.30	0.18	1.14
2	1.5	0.5	-20	0	0	-134.92	-134.57	-0.26	1.57
0	0	0	10	10	0	85.19	85.15	0.04	1.05
2	1.5	0.5	10	10	0	120.90	120.88	-0.02	1.25

Table 5.4: x-axis force validation data from [102]. The first six columns on the left define the operating point. The identified model's force prediction is compared to that of finite element analysis (FEA) and the percentage error is given. An analytic force model based on a 2D flux distribution is developed in [102] and its accuracy is tested on a similar system using FEA. The percentage error for the same set of operating points is given in the right-hand column. A comparison of the two percentage errors show that a comparable level of accuracy is achieved. Note that 1 mil $= 25.4$ μm.

discarding insignificant portions of the model. Based on FEA results, our force and torque expressions compare well to a purely analytic force and torque model based on a 2D flux distribution. The resulting model is relatively simple and provides new avenues to explore in the way of control design.

Operating Point						F_y(N)			
i_x [A]	i_y [A]	i_θ [A]	x [mil]	y [mil]	θ [deg.]	FEA	model	%error	%error[102]
0	0	2	0	0	0	0.00	0.00	-	-
3	0	0	0	0	0	0.00	0.00	-	-
0.5	1.5	0	0	0	0	26.76	26.78	0.07	0.58
0	1	2	0	0	0	17.84	17.85	0.15	0.07
0	0.2	0.5	0	0	0	3.57	3.57	0.00	0.58
2	1.5	0.5	0	0	0	26.72	26.74	0.07	0.58
2	1.5	0.5	0	0	11.25	30.88	31.25	1.21	0.37
0	0	0	-20	0	0	0.00	0.00	-	-
2	1.5	0.5	-20	0	0	26.71	26.74	0.10	2.88
0	0	0	10	10	0	85.27	85.25	-0.14	1.05
2	1.5	0.5	10	10	0	112.00	111.89	-0.10	0.44

Table 5.5: y-axis force validation data from [102]. The first six columns on the left define the operating point. The identified model's force prediction is compared to that of finite element analysis (FEA) and the percentage error is given. An analytic force model based on a 2D flux distribution is developed in [102] and its accuracy is tested on a similar system using FEA. The percentage error for the same set of operating points is given in the right-hand column. A comparison of the two percentage errors show that a comparable level of accuracy is achieved. Note that 1 mil = 25.4 μm.

Operating Point						τ(N-m)			
i_x [A]	i_y [A]	i_θ [A]	x [mil]	y [mil]	θ [deg.]	FEA	model	%error	%error[102]
0	0	2	0	0	0	7.72	7.71	0.04	2.32
3	0	0	0	0	0	0.00	0.00	-	-
0.5	1.5	0	0	0	0	0.00	0.00	-	-
0	1	2	0	0	0	7.71	7.72	0.04	2.32
0	0.2	0.5	0	0	0	1.93	1.93	0.00	2.32
2	1.5	0.5	0	0	0	1.93	1.93	0.00	2.32
2	1.5	0.5	0	0	11.25	1.90	1.91	0.14	0.96
0	0	0	-20	0	0	0.00	0.00	-	-
2	1.5	0.5	-20	0	0	1.80	1.79	-0.66	2.28
0	0	0	10	10	0	0.00	0.00	-	-
2	1.5	0.5	10	10	0	1.90	1.91	0.22	2.29

Table 5.6: Torque force validation data from [102]. The first six columns on the left define the operating point. The identified model's torque prediction is compared to that of finite element analysis (FEA) and the percentage error is given. An analytic force model based on a 2D flux distribution is developed in [102] and its accuracy is tested on a similar system using FEA. The percentage error for the same set of operating points is given in the right-hand column. A comparison of the two percentage errors show that a comparable level of accuracy is achieved. Note that 1 mil = 25.4 μm.

Chapter 6

Dynamic Modeling and Control of a Toothless Self-Bearing Servomotor

In this chapter, we migrate from a static analysis of force and torque characterization to dynamic modeling and feedback control of the toothless self-bearing servomotor (TSBS). It is here that we realize the benefits of our modeling efforts so that improved performance is ultimately realized.

6.1 Introduction

The Lorentz force is an attractive alternative to the Maxwell force as a basis for magnetic levitation. The principle advantage of Lorentz levitation is linearity between the applied current and the resulting magnetic force, thus enabling bi-directional force generation. Therefore, the magnetic force can be repulsive as well as attractive, unlike the reluctance force which can only be attractive. The Lorentz force can provide both magnetic levitation and propulsion because it exploits a motor principle. The integration of magnetic levitation and motoring through a common Lorentz principle has led to the contactless linear drive used in precision positioning platforms [62, 94], and in the rotary version, all-Lorentz self-bearing motors (SBMs) [101, 123]. As a precision servo-drive, the TSBS can be viewed as both an all-Lorentz SBM as well as a precision positioning platform. The TSBS produces minimal cogging torque and detent because of its toothless construction and contactless nature, and was conceived as a potential alternative to mechanical gimbals in precision pointing and slewing applications.

Although the TSBS was designed to produce smooth torque, it also possesses some undesirable levitation characteristics. From the FEA study in Chapter 5, it is clear that the TSBS has a low bearing capacity relative to conventional active magnetic bearings (AMBs).

Low bearing capacity leads to a restricted region of operation and can pose startup difficulties. A second problem is that, in the presence of input saturation, bearing forces are in conflict with torque since both are generated from a common winding set. The purpose of this chapter is to show that both of these problems can be alleviated, to varying degrees, by advanced control.

Central to the ideas in this chapter is exploitation of previously unutilized control variables. As it was originally conceived, the TSBS generates four tangential control forces to produce motion in 3DOF. This is shown in Figure 6.1. Each control force is generated from an individual three-phase winding driven by its current magnitude. The established control design consists of a static four-to-three input transformation leading to a decentralized control [101]. In this chapter we present a more general operating principle of the TSBS through the additional manipulation of the phase angle γ in the commutation scheme. This generalization is simply based on established work on the commutation and control of all-Lorentz SBMs and linear permanent magnet synchronous motors (LPMSMs) . Specifically, all-Lorentz SBMs, with the exception of the TSBS, are levitated by three-phase currents where the phase angle determines the direction of the net radial force [90, 61]. Likewise, LPMSMs utilize vector control of three-phase windings to generate suspension (normal) and propulsion (tangential) on the translating member [124]. By analogy, phase-angle manipulation of the TSBS generates normal forces on the rotor in addition to tangential forces. The benefit is radial load balancing, in effect current equalization among segments, independent of rotor position and the direction of loading. Manipulating a common phase angle among all four segments of the TSBS, we devise an *active load balancing* scheme that achieves performance benefits relative the established commutation and control of the TSBS. Specifically, phase-angle manipulation permits an expanded range of rotor positioning including alleviation of startup difficulties. We also show that a four-to-four input transformation recovers a free control parameter. We use this parameter to maximize torque production in a priority scheme that resolves the force-torque conflict. As a basis for this control redesign, we begin this chapter with a derivation of a dynamic model for the TSBS that incorporates phase-angle manipulation as well as modeling results from Chapter 5.

6.2 Generalized force and torque generation

We briefly revisit force and torque modeling from Chapter 5 to include the phase-angle manipulation in the commutation scheme, and to establish the expressions which will form

a basis for the dynamic model.

To derive the control forces in terms of the excitation currents, we recall from Figure 6.1 the 3DOF coordinate system (x, y, θ) and the stator angle Φ over which we integrate to calculate force and torque. The air-gap flux density due to the permanent magnets (PMs) is given by (5.8), and the winding distribution is given by (5.2). Three-phase currents for

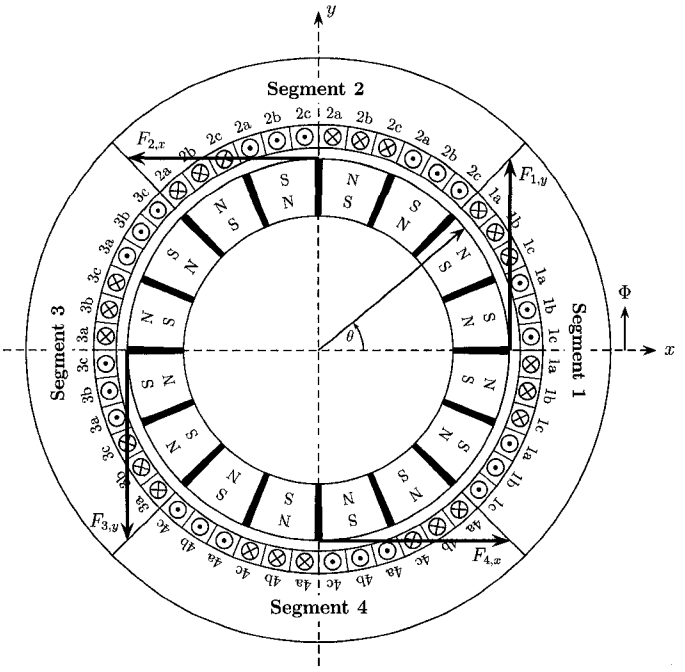

Figure 6.1: A sixteen-pole, toothless self-bearing servomotor (TSBS). The x and y axes denote rotor coordinates relative to the stator center, Φ is the stator angle and θ is the rotor angle. The four control forces are denoted $F_{1,y}, F_{2,x}, F_{3,y}$ and $F_{4,x}$.

segment k, when controlled by their magnitude i_k and phase angle γ_k, are expressed as

$$\begin{aligned} i_{k,a}(i_k, \gamma_k, \theta) &= i_k \cos\left(M(\theta + \gamma_k) - \frac{\pi}{3}\right), \\ i_{k,b}(i_k, \gamma_k, \theta) &= i_k \cos\left(M(\theta + \gamma_k)\right), \\ i_{k,c}(i_k, \gamma_k, \theta) &= i_k \cos\left(M(\theta + \gamma_k) + \frac{\pi}{3}\right). \end{aligned}$$

For simplicity, it is henceforth assumed that all segments share a common phase angle such that $\gamma_k = \gamma, 1 \leq k \leq 4$. The resulting current distribution for the k^{th} quadrant is thus given by

$$\begin{aligned} I_k(i_k, \gamma, \Phi, \theta) &= N_a(\Phi) i_{k,a}(i_k, \gamma, \theta) + N_b(\Phi) i_{k,b}(i_k, \gamma, \theta) + N_c(\Phi) i_{k,c}(i_k, \gamma, \theta) \\ &= N_0' i_k \sin\left[M\left(\Phi - \theta - \gamma\right)\right], \end{aligned}$$

The x- and y-axis Lorentz forces $F_{x,L}, F_{y,L}$ and torque τ are now computed from the integrals

$$F_{x,L}(x,y,\theta,i_k,\gamma) = L\sum_{k=1}^{4}\int_{l_k}^{u_k} B_{g,m}(\Phi)I_k(\Phi)\sin\Phi \mathrm{d}\Phi, \tag{6.1a}$$

$$F_{y,L}(x,y,\theta,i_k,\gamma) = -L\sum_{k=1}^{4}\int_{l_k}^{u_k} B_{g,m}(\Phi)I_k(\Phi)\cos\Phi \mathrm{d}\Phi, \tag{6.1b}$$

$$\tau_L(x,y,\theta,i_k,\gamma) = -rL\sum_{k=1}^{4}\int_{l_k}^{u_k} B_{g,m}(\Phi)I_k(\Phi)\mathrm{d}\Phi. \tag{6.1c}$$

Evaluation of (6.1) is obtained through the harmonic approximation (5.16). Form the insight obtained in Chapter 5, we assume that force and torque has a negligible dependence on rotor angle. Therefore, we use approximate expressions obtained by evaluating (6.1) at the home rotor, $(x,y,\theta) = 0$:

$$F_{x,L}(i_k,\gamma) = \frac{\sqrt{2}LN_0'Pm_1}{(P^2-1)m_2}\left(P\cos(M\gamma)\frac{i_4-i_2}{2} - \sin(M\gamma)\frac{i_1-i_3}{2}\right), \tag{6.2a}$$

$$F_{y,L}(i_k,\gamma) = \frac{\sqrt{2}LN_0'Pm_1}{(P^2-1)m_2}\left(P\cos(M\gamma)\frac{i_1-i_3}{2} + \sin(M\gamma)\frac{i_4-i_2}{2}\right), \tag{6.2b}$$

$$\tau_L(i_k,\gamma) = \frac{\pi rLN_0'm_1\cos(M\gamma)}{m_2}\left(\frac{i_1+i_2+i_3+i_4}{4}\right). \tag{6.2c}$$

where $P = 2M$ and (6.2) is valid for M being a positive integer multiple of 4. The x- and y-axis Maxwell forces $F_{x,M}, F_{y,M}$ are obtained by

$$F_{x,M}(x,y,\theta,i_k,\gamma) = \frac{rL}{2\mu_0}\sum_{k=1}^{4}\int_{l_k}^{u_k}(B_{g,m}(\Phi)+B_{g,w,k}(\Phi))^2\cos\Phi\,\mathrm{d}\Phi, \tag{6.3a}$$

$$F_{y,M}(x,y,\theta,i_k,\gamma) = \frac{rL}{2\mu_0}\sum_{k=1}^{4}\int_{l_k}^{u_k}(B_{g,m}(\Phi)+B_{g,w,k}(\Phi))^2\sin\Phi\,\mathrm{d}\Phi, \tag{6.3b}$$

where $B_{g,w,k}$ is the air-gap flux due to the k^{th} segment's stator windings and given by (5.9). integrals (6.3) are approximated the dominant negative stiffness as well as the cross terms described in Chapter 5:

$$F_{x,M} = \frac{\pi rLm_1^2}{2\mu_0 m_2^3}x - \frac{\sqrt{2}Lrm_1w_1P^2\sin(M\gamma)}{(P^2-1)\mu_0 m_2 w_2}\left(\frac{i_1-i_3}{2}\right), \tag{6.4a}$$

$$F_{y,M} = \frac{\pi rLm_1^2}{2\mu_0 m_2^3}y + \frac{\sqrt{2}Lrm_1w_1P^2\sin(M\gamma)}{(P^2-1)\mu_0 m_2 w_2}\left(\frac{i_4-i_2}{2}\right). \tag{6.4b}$$

The combination of the Lorentz forces (6.2) and the Maxwell forces (6.4) approximates the total force $F_{x,m}, F_{y,m}$ and torque τ. Lumping parameters, the total force and torque is

given by

$$F_{x,m}(x, i_k, \gamma) = \alpha_d \cos(M\gamma) \left(\frac{i_4 - i_2}{2} \right) - \alpha_c \sin(M\gamma) \left(\frac{i_1 - i_3}{2} \right) + \alpha_x x, \quad (6.5a)$$

$$F_{y,m}(y, i_k, \gamma) = \alpha_d \cos(M\gamma) \left(\frac{i_1 - i_3}{2} \right) + \alpha_c \sin(M\gamma) \left(\frac{i_4 - i_2}{2} \right) + \alpha_x y, \quad (6.5b)$$

$$\tau(i_k, \gamma) = \alpha_\tau \cos(M\gamma) \frac{(i_1 + i_2 + i_3 + i_4)}{4}, \quad (6.5c)$$

where α_d, α_c denote the direct and cross current gains, α_x is the negative stiffness gain, and α_τ is the torque constant. For $\gamma = 0$, (6.5a)-(6.5b) bare the familiar structure of a bias-current-linearized AMB (2.19).

6.3 Experimental realization

A laboratory TSBS was constructed by Airex Corporation (Somersworth, NH) and is housed in the Applied Nonlinear Control Laboratory at the University of Alberta. It is integrated with AMBs to create a 6DOF contactless actuator. Figure 6.2(a) is a solid model of the system generated with the software package Pro/Engineer. It is a horizontal shaft configuration consisting of a sixteen-pole TSBS, two radial AMBs and an axial AMB. A redundant radial AMB is located adjacent to the TSBS and is useful for the commissioning, identification, and loading of the TSBS. The radial AMBs have a standard eight pole configuration.

The shaft, shown in Figure 6.2(b), is a hollow cylinder composed of a high permeability, low-carbon steel so that it functions as journal material for the radial bearings and as back iron for the PMs. The shaft wall has a varying thickness in the range of 0.3-0.375" (7.6-9.5 mm). The TSBS portion of the shaft has a larger diameter to create more surface area for the PMs, which in turn yields greater bearing forces. Hence, the shaft has a diameter of approximately $4.5''$ (114.3 mm) for the first $3''$ (76.2 mm) of shaft length, and then steps down to a diameter of $3''$ for the remaining $7''$ (177.8 mm) of shaft length. The shaft has PMs (N44H type with a remanence flux density of 1.3 T) bonded to it at the outboard end and a thrust disk at the inboard end.

Software-based modal analysis of the shaft indicates that the first bending mode is at about 4.2 kHz and the second at about 8.5 kHz. Since these frequencies far exceed the bandwidth of the servoamplifiers, and since the TSBS is intended for low-speed application, a rigid body is assumed for modeling and control design. With respect to the TSBS, its nominal air gap is about 0.9 mm, and the thicknesses of the PMs, windings and stator are approximately 8.6 mm, 6.2 mm, and 7.1 mm, respectively.

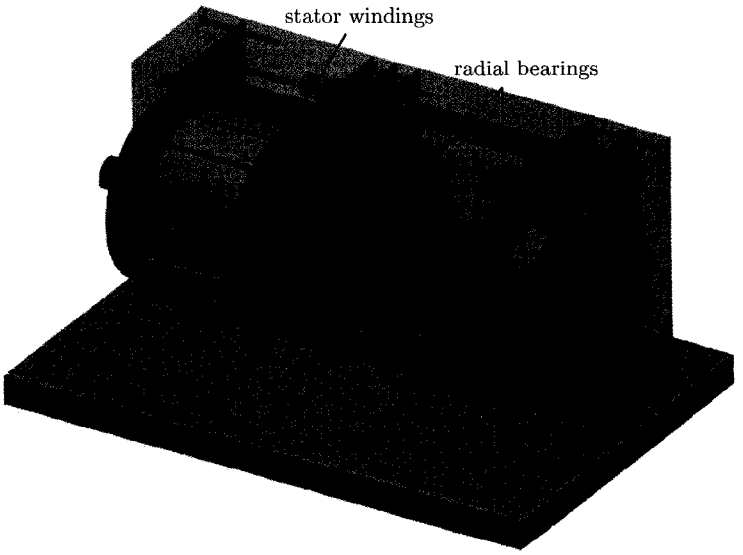

(a) computer generated view of shaft and actuators (courtesy of R. Chladny)

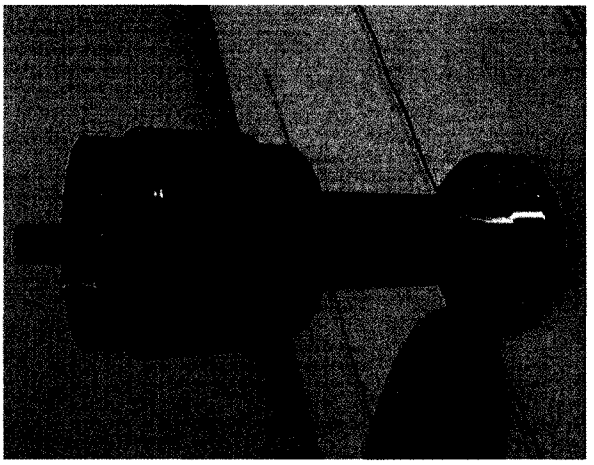

(b) actual shaft

Figure 6.2: Experimental realization of a toothless self-bearing servomotor within a 6 degree-of-freedom system. Additional levitation is provided by radial and axial active magnetic bearings.

Eddy current proximity sensors measure radial displacement of the shaft in two planes and axial displacement in one plane. An angular encoder based on a pair of differential hall sensors in quadrature sense the angle of rotation. The TSBS and AMBs are driven by a combined 22 single-phase servoamplifiers (twelve for the TSBS, four per radial AMB, and two for the axial AMB). Single-phase amplifiers provide hardware flexibility but are not necessary for the TSBS since each of its segments can alternatively be driven by a three-

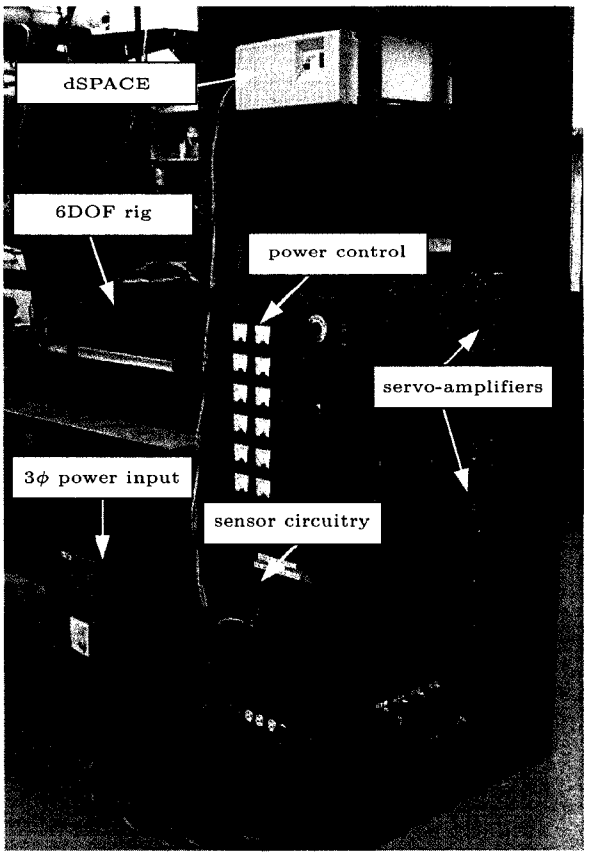

Figure 6.3: Experimental setup. The cabinet contains a dSpace digital signal processor for real-time computation, 22 servoamplifiers (12 for the toothless self-bearing servomotor, and 10 for the active magnetic bearings), sensor conditioning and thermal management circuitry, and power controls to engage banks of servoamplifiers in succession.

phase inverter. The amplifiers are digital PWM with a switching frequency of 25 kHz, a continuous current rating of 12 A and a voltage rating of 148 VDC. Due to the very low inductance of the TSBS coils (40 turns each), each of which is approximately 0.2-0.5 mH, we assume that the servoamplifiers have infinite bandwidth for the purpose of control design. Based on the high power of the overall system, thermal sensing and overheating protection circuitry are integrated with the rig.

Feedback control and commutation are implemented in Matlab/Simulink and executed in real-time with dSpace modular hardware at a sampling frequency of 10 kHz. The dSpace modular system is flexible and was also the hardware platform used with the AMB test bench described in Chapter 2. A graphical interface was designed with software accompanying the dSpace. The interface allows for real-time logging of data and tuning of parame-

ters.

Figure 6.3 shows the overall experimental setup. In addition to the control hardware, servoamplifiers, sensor circuitry and input power module, power controls are necessary to engage banks of servoamplifiers in succession for soft-starting.

6.4 Dynamic model

We briefly provide a dynamic model for the experimental 6DOF system and proceed to narrow our investigation on the TSBS portion of the system. We assume a rigid rotor without mass unbalance and gyroscopic behavior. The system is depicted in Figure 6.4 and its dynamic equations are given by

$$m\ddot{x} = F_{x,m} + F_{x,o} + F_{x,i}, \tag{6.6a}$$

$$m\ddot{y} = F_{y,m} + F_{y,o} + F_{y,i} - mg, \tag{6.6b}$$

$$m\ddot{z} = F_z, \tag{6.6c}$$

$$J\ddot{\phi} = \ell_{i,a}F_{y,i} - \ell_{o,a}F_{y,o} - \ell_m F_{y,m}, \tag{6.6d}$$

$$J\ddot{\psi} = -\ell_{i,a}F_{x,i} + \ell_{o,a}F_{x,o} + \ell_m F_{x,m}, \tag{6.6e}$$

$$J_z\ddot{\theta} = \tau - B\dot{\theta}, \tag{6.6f}$$

where x, y and z define the translation of the center of mass (COM) from the origin of the inertial frame. The angles ϕ and ψ denote the small angle rotation of the shaft with respect to the translated x and y axes, and θ is rotation about the z-axis. The model parameters are described in Table 6.1. As depicted in Figure 6.4, x- and y-axis forces are generated in three actuator planes (m - "motor", o, a - "outboard actuator", i, a - "inboard actuator") and radial displacement is sensed in two planes (i, s -"inboard sensor", o, s - "outboard sensor"). From (6.6c) it is evident that the axial dynamics are trivial, and we shall henceforth ignore them. Furthermore, we shall ignore the outboard AMB forces $F_{x,o}, F_{y,o}$ since they do not factor into the control design. Rather, their use is made clear during the discussion on parameter identification.

Displacement in the actuator planes must be calculated from the measured displacements based on the system geometry. Accordingly, there are five system outputs: the rotor angle θ, and displacement along the x and y axes in the measurement planes, denoted

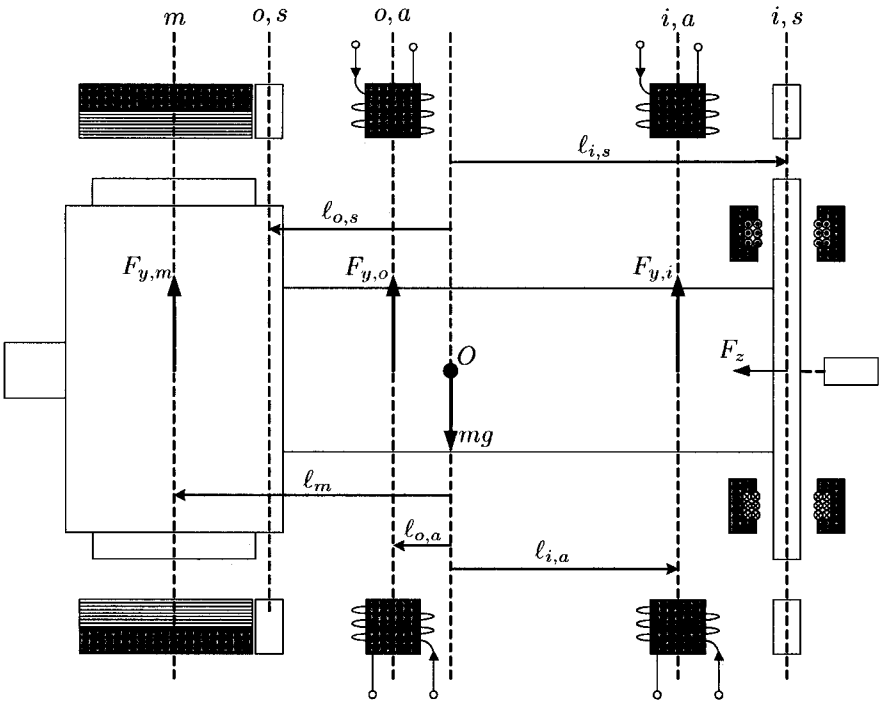

Figure 6.4: A schematic view of the $y-z$ plane of the 6 degree-of-freedom experimental system. Detailed here are the distances of the sensor and actuator planes from the shaft's center of mass, O, as well as the actuator forces, $F_{y,m}, F_{y,o}, F_{y,i}, F_z$, and gravity, mg. The notation o, s denotes "outboard sensor," o, a denotes "outboard actuator," i, s denotes "inboard sensor," i, a denotes "inboard actuator," and m denotes "motor".

$\tilde{x}_{o,s}, \tilde{y}_{o,s}, \tilde{x}_{i,s}, \tilde{y}_{i,s}$. The radial displacement measurements are further expressed as

$$\begin{bmatrix} \tilde{x}_{o,s} \\ \tilde{y}_{o,s} \\ \tilde{x}_{i,s} \\ \tilde{y}_{i,s} \end{bmatrix} = \begin{bmatrix} x_{o,s} - \bar{x}_{o,s} \\ y_{o,s} - \bar{y}_{o,s} \\ x_{i,s} - \bar{x}_{i,s} \\ y_{i,s} - \bar{y}_{i,s} \end{bmatrix}$$

to account for magnetic offsets, denoted $\bar{x}_{i,s}, \bar{y}_{i,s}, \bar{x}_{o,s}, \bar{y}_{o,s}$. Magnetic offsets are described in Chapter 2, and lead to bias forces. The COM coordinates x, y, ϕ, ψ are expressed in terms of the system outputs by

$$\phi = \frac{(\tilde{y}_{i,s} + \bar{y}_{i,s}) - (\tilde{y}_{o,s} + \bar{y}_{o,s})}{\ell_{i,s} + \ell_{o,s}}, \tag{6.7a}$$

$$\psi = \frac{(\tilde{x}_{o,s} + \bar{x}_{o,s}) - (\tilde{x}_{i,s} + \bar{x}_{i,s})}{\ell_{i,s} + \ell_{o,s}}, \tag{6.7b}$$

$$x = \frac{\ell_{o,s}(\tilde{x}_{i,s} + \bar{x}_{i,s}) + \ell_{i,s}(\tilde{x}_{o,s} + \bar{x}_{o,s})}{\ell_{i,s} + \ell_{o,s}}, \tag{6.7c}$$

$$y = \frac{\ell_{o,s}(\tilde{y}_{i,s} + \bar{y}_{i,s}) + \ell_{i,s}(\tilde{y}_{o,s} + \bar{y}_{o,s})}{\ell_{i,s} + \ell_{o,s}}. \tag{6.7d}$$

parameter	description	value
m	mass of shaft	10.2 kg
g	acceleration due to gravity	9.81 m/s^2
J	transverse inertia	0.116 kg-m^2
J_z	polar inertia	0.033 kg-m^2
$l_{o,a}$	from COM to outboard AMB actuating plane	0.010 m
l_m	from COM to motor actuating plane	0.122 m
$l_{i,a}$	from COM to inboard AMB actuating plane	0.115 m
$l_{o,s}$	from COM to outboard sensing plane	0.052 m
$l_{i,s}$	from COM to inboard sensing plane	0.161 m

Table 6.1: Mass and geometry parameters of the 6 degree-of-freedom experimental system, as depicted in Figure 6.4. COM denotes the "center of mass" of the shaft and is determined, along with the inertias, from software analysis of the solid model depicted in Figure 6.2(a).

Manipulation of (6.6) and (6.7) gives the system model in output coordinates

$$
\begin{aligned}
m\ddot{\tilde{x}}_{o,s} &= \left(1+\frac{m\ell_{o,s}\ell_m}{J}\right)F_{x,m}+\left(1-\frac{m\ell_{o,s}\ell_{i,a}}{J}\right)F_{x,i},\\
m\ddot{\tilde{y}}_{o,s} &= \left(1+\frac{m\ell_{o,s}\ell_m}{J}\right)F_{y,m}+\left(1-\frac{m\ell_{o,s}\ell_{i,a}}{J}\right)F_{y,i}+\frac{l_{i,a}}{l_{i,a}+l_m}mg,\\
m\ddot{\tilde{x}}_{i,s} &= \left(1-\frac{m\ell_{i,s}\ell_m}{J}\right)F_{x,m}+\left(1+\frac{m\ell_{i,s}\ell_{i,a}}{J}\right)F_{x,i},\\
m\ddot{\tilde{y}}_{i,s} &= \left(1-\frac{m\ell_{i,s}\ell_m}{J}\right)F_{y,m}+\left(1+\frac{m\ell_{i,s}\ell_{i,a}}{J}\right)F_{y,i}+\frac{l_m}{l_{i,a}+l_m}mg,\\
J_z\ddot{\theta} &= \tau - B\dot{\theta}.
\end{aligned}
$$

Based on the parameter values in Table 6.1, the influence of $F_{x,m}, F_{y,m}$ on the outboard measurement plane is over three times as great as the influence of $F_{x,i}, F_{y,i}$. This is justification for decoupling of the TSBS and the inboard AMB. Hence the approximate dynamic model for the TSBS portion of the experimental system is

$$
\begin{aligned}
m\ddot{\tilde{x}}_{o,s} &= \left(1+\frac{m\ell_{o,s}\ell_m}{J}\right)F_{x,m},\\
m\ddot{\tilde{y}}_{o,s} &= \left(1+\frac{m\ell_{o,s}\ell_m}{J}\right)F_{y,m}+\frac{l_{i,a}}{l_{i,a}+l_m}mg,\\
J_z\ddot{\theta} &= \tau - B\dot{\theta}.
\end{aligned}
$$

We incorporate the TSBS force and torque expressions (6.5) and assume that the inboard AMB independently stabilizes the inboard end of the shaft so that $(\tilde{x}_{i,s}, \tilde{y}_{i,s}) = 0$. The

resulting model is

$$m'\ddot{\tilde{x}}_{o,s} = \alpha_d \cos(M\gamma)\left(\frac{i_4 - i_2}{2}\right) - \alpha_c \sin(M\gamma)\left(\frac{i_1 - i_3}{2}\right) + \alpha'_x \tilde{x}_{o,s} + F_{c,x}, \quad (6.8a)$$

$$m'\ddot{\tilde{y}}_{o,s} = \alpha_d \cos(M\gamma)\left(\frac{i_1 - i_3}{2}\right) + \alpha_c \sin(M\gamma)\left(\frac{i_4 - i_2}{2}\right) + \alpha'_x \tilde{y}_{o,s} + F_{c,y}, \quad (6.8b)$$

$$J_z\ddot{\theta} = \alpha_\tau \cos(M\gamma)\frac{(i_1 + i_2 + i_3 + i_4)}{4} - B\dot{\theta} + T_c, \quad (6.8c)$$

where we define the effective mass $m' = mJ/(J + m\ell_{o,s}\ell_m)$, the negative stiffness coefficient $\alpha'_x = (\ell_{i,s} + \ell_m)/(\ell_{i,s} + \ell_{o,s})\alpha_x$ accounting for sensor-actuator non-colocation, bias forces $F_{c,x} = \alpha_x \bar{x}_m$ and $F_{c,y} = \alpha_x \bar{y}_m + l_{i,a}m'g/(l_{i,a} + l_m)$ accounting for gravity and magnetic offsets, and a bias torque T_c capturing possible detent. The resultant system is sixth order with five inputs, $i_1, i_2, i_3, i_4, \gamma$, and three outputs, $\tilde{x}_{o,s}, \tilde{y}_{o,s}, \theta$.

6.5 Nominal control design

Our empirical investigation begins with the implementation of a control strategy which is based on previous TSBS research efforts [120, 119]. The purpose is to establish a performance benchmark and gain insight into its performance limitations. The established design is decentralized proportional-plus-integral-plus-derivative (PID) under the assumption of $\gamma = 0$ and the four-to-three input transformation

$$i_1 = i_\theta + i_y, \quad (6.9a)$$

$$i_2 = i_\theta - i_x, \quad (6.9b)$$

$$i_3 = i_\theta - i_y, \quad (6.9c)$$

$$i_4 = i_\theta + i_x, \quad (6.9d)$$

that, when substituted into (6.8), gives the decoupled equations of motion

$$m'\ddot{\tilde{x}}_{o,s} = \alpha_d i_x + \alpha'_x \tilde{x}_{o,s} + F_{c,x}, \quad (6.10a)$$

$$m'\ddot{\tilde{y}}_{o,s} = \alpha_d i_y + \alpha'_x \tilde{y}_{o,s} + F_{c,y}, \quad (6.10b)$$

$$J_z\ddot{\theta} = \alpha_\tau i_\theta - B\dot{\theta} + T_c. \quad (6.10c)$$

Finite element analysis from Chapter 5 gave preliminary estimates for the parameters in (6.10) as a basis for control design. Within the set of theoretically feasible pole locations, finding ones that resulted in closed-loop stability, experimentally speaking, is not challenging. This owes mainly to the very low flexibility of the shaft, resulting in a high immunity

to noise. In fact, additional filtering in the closed loop, which is often necessary to stabilize rotor-AMB systems, is unnecessary here. Proportional, integral, and derivative gains of

$$(K_p, K_i, K_d) = (100 \text{ A/mm}, 0.2 \text{ A-s/mm}, 100 \text{ A/(mm-s)})$$

and

$$(K_{p,\theta}, K_{i,\theta}, K_{d,\theta}) = (50 \text{ A/rad}, 0.5 \text{ A-s/rad}, 50 \text{ A/(rad-s)})$$

were chosen for the levitation and rotational subsystems respectively.

The simplicity of decentralized PID and the ease of gain selection are indeed favorable characteristics. However, two drawbacks are apparent from operating the TSBS with the established control system. First, due to the large air gap and high negative stiffness of the PMs, the TSBS has insufficient bearing capacity to lift off. Stability only results from maintaining the shaft in a region near or above the stator center where the negative stiffness of the PMs is either small or offsets gravity. The second problem is that aggressive operation of the rotational subsystem, through large and fast reference signals or high gain, immediately lead to instability of the levitation subsystem. Whether aggressive operation of the rotational subsystem is necessary or not depends on the application. Nevertheless, it is an obvious drawback of the machine which we choose to address with our control design efforts.

6.6 Model validation and identification

We describe some simple model-based experiments and least squares fits to validate the force expressions (6.5a)-(6.5b) and estimate the parameters of the dynamic model (6.8).

6.6.1 AMB calibration

To experimentally identify TSBS parameter, we calibrate the radial AMBs so that they can function as force sensors. Both the inboard and outboard AMBs, when levitating the shaft and stabilizing it to origin, have a linear force-current relationship defined by

$$F_{y,i} = K_i i_i + \bar{F}_{y,i}$$
$$F_{y,o} = K_o i_o + \bar{F}_{y,o}$$

where $F_{y,i}, F_{y,o}$ are the y-axis inboard and outboard forces respectively (our attention in this section is restricted to the $y-z$ plane), K_i, K_o are the current-to-force constants for each radial AMB, i_i, i_o are the control currents operating in constant-current-sum mode (see

the Chapter 2 introduction for an explanation), and $\bar{F}_{y,i}, \bar{F}_{y,o}$ are bias forces. If we hang a known mass m_Δ off the outboard end of the shaft at a known distance ℓ_Δ from the center of mass of the shaft, the steady state equations of motion simplify to

$$0 = F_{y,i} + F_{y,o} + F_{c,y} - (m + m_\Delta)g, \tag{6.11a}$$

$$0 = \ell_{i,a}F_{y,i} - \ell_{o,a}F_{y,o} - \ell_m F_{c,y} + \ell_\Delta m_\Delta g, \tag{6.11b}$$

where $F_{c,y}$ is bias force due to magnetic offset of the TSBS. We hang a series of known masses $m_\Delta[k], 1 \leq k \leq N$ to the shaft, measure the resulting control currents in steady state $i_i[k], i_o[k]$, and de-trend successive pairs of equations to eliminate unknown bias forces. Equation (6.11) becomes

$$0 = K_i\Delta i_i[k] + K_o\Delta i_o[k] - \Delta m_\Delta[k]g,$$

$$0 = \ell_{i,a}K_i\Delta i_i[k] - \ell_{o,a}K_o\Delta i_o[k] + \ell_\Delta\Delta m_\Delta[k]g.$$

where Δ is the backward difference operator, e.g. $\Delta i_i[k] = i_i[k] - i_i[k-1]$. We solve for K_i, K_o by pseudo-inversion of the following system of equations

$$\begin{bmatrix} \Delta i_i[k+1] & \Delta i_o[k+1] \\ \ell_{i,a}\Delta i_i[k+1] & -\ell_{o,a}\Delta i_o[k+1] \\ \vdots & \vdots \\ \Delta i_i[k+N] & \Delta i_o[k+N] \\ \ell_{i,a}\Delta i_i[k+N] & -\ell_{o,a}\Delta i_o[k+N] \end{bmatrix} \begin{bmatrix} K_i \\ K_o \end{bmatrix} = \begin{bmatrix} m_\Delta[k+1]g \\ \ell_\Delta m_\Delta[k+1]g \\ \vdots \\ m_\Delta[k+N]g \\ \ell_\Delta m_\Delta[k+N]g \end{bmatrix}$$

based on known parameters from Table 6.1. A series of $N = 4$ masses are used to obtain a fit, and the experiment is repeated over a range of rotor angles to get an average. The results are shown in Figure 6.5(a) and the averages values obtained, for a bias current of 3 A in each AMB, are

$$K_i = 73.2 \pm 4.4\% \text{ N/A}, \tag{6.12a}$$

$$K_o = 74.4 \pm 4.3\% \text{ N/A}. \tag{6.12b}$$

6.6.2 TSBS direct force constant

With the AMBs calibrated as force sensors, the previous procedure is effectively reversed. That is, unknown forces are applied to the levitated shaft by injecting open-loop currents into the TSBS. The unknown forces are measured by the load absorbed by the AMBs. For a fixed and centered shaft, the force from the TSBS is

$$F_{y,m} = \alpha_d i_y + F_{c,y},$$

where $i_x = \gamma = 0$ is assumed. The resulting balance of forces and moments in steady state are

$$0 = F_{y,i} + F_{y,o} + F_{y,m} - mg, \tag{6.13a}$$

$$0 = \ell_{i,a} F_{y,i} - \ell_{o,a} F_{y,o} - \ell_m F_{y,m}. \tag{6.13b}$$

Applying successive open-loop $i_y[k]$ and de-trending, equation (6.13) becomes

$$0 = K_i \Delta i_i[k] + K_o \Delta i_o[k] - \alpha_d \Delta i_y[k], \tag{6.14a}$$

$$0 = \ell_{i,a} K_i \Delta i_i[k] - \ell_{o,a} K_o \Delta i_o[k] - \ell_m \alpha_d \Delta i_y[k]. \tag{6.14b}$$

The direct force constant α_d is the only unknown quantity in (6.14) and can be estimated by means of linear least squares similar to that used in the last section to identify K_i, K_o.

Another experiment identifies the negative stiffness coefficient α_x. The details are omitted since the approach is analogous to that just described, with the exception being that the unknown force is applied via eccentric positioning of the shaft, i.e.

$$F_{y,m} = \alpha_x' \tilde{y}_{o,s} + F_{c,y}.$$

6.6.3 Radial force coupling

We now assess the accuracy of the phase-angle dependent force model. This is a key relationship which we exploit for control redesign. Furthermore, it remains to identify the coupled force-to-current constant α_c. As one approach, we operate the TSBS in closed-loop, stabilize the rotor at the home position, i.e. $(\tilde{x}_{o,s}, \tilde{y}_{o,s}, \theta) = 0$, and vary γ in small increments. The steady state equations of motion for the TSBS levitation subsystem are

$$0 = \alpha_d \cos(M\gamma) i_x - \alpha_c \sin(M\gamma) i_y + F_{c,x},$$

$$0 = \alpha_d \cos(M\gamma) i_y + \alpha_c \sin(M\gamma) i_x + F_{c,y}.$$

For a series of phase angles $\gamma[k], 1 \leqslant k \leqslant R$, we measure the resulting steady state set $(i_x[k], i_y[k])$. De-trending the resulting equations gives

$$\begin{bmatrix} \Delta(\cos(M\gamma[k+1]) i_x[k+1]) \\ \Delta(\cos(M\gamma[k+1]) i_y[k+1]) \\ \vdots \\ \Delta(\cos(M\gamma[k+R]) i_x[k+R]) \\ \Delta(\cos(M\gamma[k+R]) i_y[k+R]) \end{bmatrix} \alpha_d/\alpha_c = \begin{bmatrix} \Delta(\sin(M\gamma[k+1]) i_y[k+1]) \\ -\Delta(\sin(M\gamma[k+1]) i_x[k+1]) \\ \vdots \\ \Delta(\sin(M\gamma[k+R]) i_y[k+R]) \\ -\Delta(\sin(M\gamma[k+R]) i_x[k+R]) \end{bmatrix}. \tag{6.15}$$

A unique solution of $\alpha_d/\alpha_c = 0.85$ results which allows us to calculate α_c. This data fit is based on the range of phase angles $-2.5 \leqslant \gamma \leqslant 3.5$ in 0.5 deg increments such that

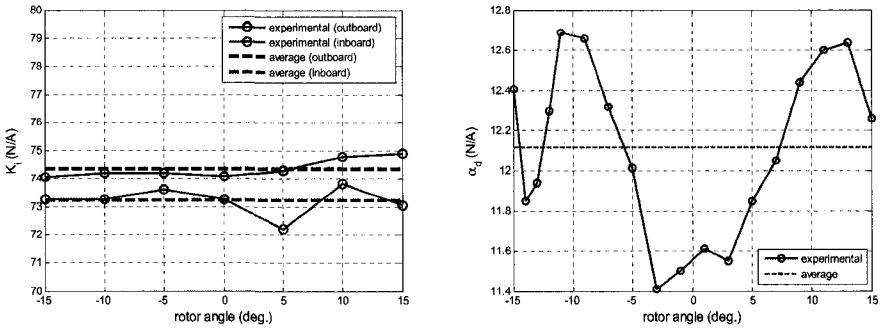

(a) radial AMB calibration

(b) TSBS direct force constant vs. rotor angle

Figure 6.5: Parameter identification. Initially, the radial AMBs are calibrated by a procedure of hanging known masses off the levitated shaft and measuring the deflection in AMB control current. Then the current-to-force ratio of the TSBS is determined by applying open-loop test currents and measuring the load absorbed by the AMBs.

$N = 13$. The model fit-to-data error is $\pm 2\%$ confirming the accuracy of our analytical force model.

The fact that $\alpha_c \neq \alpha_d$ is an interesting result. Strictly speaking, this fact aligns with our 1D-flux-based force modeling. However, analytical force modeling of LPMSMs in [124, 62] based on a 2D flux distribution predicts that lateral and vertical forces constants are equal. At any rate, a clear explanation as to why this discrepancy exists in practice requires further investigation but we conjecture that operating all four segments with a common phase angle does not lead each segment to operate with uniform characteristics (due to errors in the phase-spacing of the TSBS coils, for example). Therefore, some interference in the force generation is to be expected, e.g. one segment generating a residual normal force when $\gamma = 0$.

6.6.4 Rotation subsystem

Figure 6.6(a) plots the torque-to-current ratio for various phase angles. In this setup, the TSBS is operated only as a servomotor whereas the outboard AMB provides levitation in addition to the inboard AMB. The TSBS is controlled in closed-loop to maintain the shaft at $\theta = 0$ while known torques are applied. This setup is depicted in Figure 6.6(c). Specifically, three masses $m_\Delta = \{0.75 \text{ kg}, 1.83 \text{ kg}, 2.20 \text{ kg}\}$ are hung at a radius of $\ell_\tau = 0.23$ m. The deflection in the servo control current i_θ is measured for each mass, and this procedure is repeated for the range of phase angles shown in Figure 6.6(a). Least squares is used to

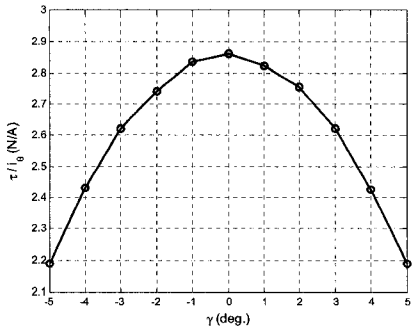

(a) torque constant vs. phase angle

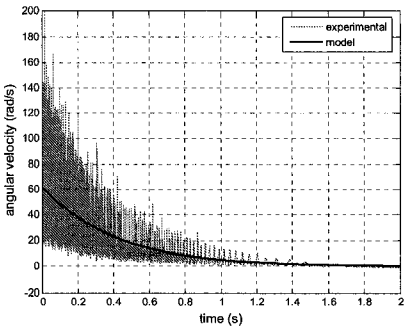

(b) rotor spindown tests

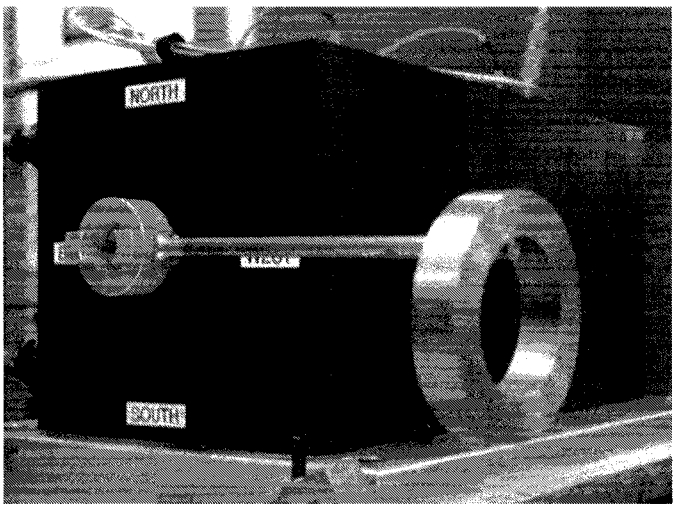

(c) applying torque to the TSBS

Figure 6.6: Experimental measurements used to determine the torque constant and coefficient of friction.

estimate α_τ on the assumption that

$$m_\Delta \ell_\tau = \alpha_\tau \cos(M\gamma) i_\theta$$

. The peak of the graph in Figure 6.6(a) is the torque constant α_τ.

Spindown tests of the shaft are used to identify the coefficient of magnetic friction B, assumed to have a similar characteristic to viscous friction. Magnetic friction is unusually high in this system due to the prominence of eddy-currents which result from the magnetic bearings suspending an unlaminated rotor. Figure 6.6(b) shows the superimposed result of a spindown test and the modeled deceleration based on the equation

$$\omega(t) = \omega(t_0) e^{-B(t-t_0)/J}, \qquad t \geq t_0 \tag{6.16}$$

parameter	description	value
α_d	direct force-to-current constant	12.1 N/A
α_c	coupled force-to-current constant	14.3 N/A
α'_x	negative stiffness constant	322.3 N/mm
α_τ	torque constant	2.87 N-m/A
B	coefficient of magnetic friction	0.081 N-m-s/rad

Table 6.2: Experimentally identified model parameters of the TSBS. The prototype TSBS produces smooth torque but suffers from low bearing capacity relative to conventional AMBs of a similar size. Applications of positioning tend to be the most suitable given this characteristic.

where $\omega = \dot{\theta}$ and (6.16) is the solution to

$$J_z\dot{\omega} = -B\omega$$

The parameters $\omega(t_0)$ and B/J from (6.16) are fit by a nonlinear least squares curve fitting tool, and B is recovered from knowledge of J_z.

Table 6.2 gives the values for all model parameters with the exception of $F_{c,x}$, $F_{c,y}$ and T_c, which must be estimated online. Comparing the force constant α_d to the AMB force constants (6.12), it is confirmed that the prototype TSBS has a relatively low bearing capacity. The relatively large mechanical air gap the TSBS ($\approx$ 0.9 mm) is a major cause because it weakens the air gap flux from the PMs. Indeed, from magnetic circuit analysis in Chapter 5 we show that the force and torque constants are inversely proportional to m_2 where m_2 is approximately equal to the magnetic air gap, i.e. the radial distance between the rotor and stator back irons.

6.7 Control

In this section, the control system is redesigned to alleviate instability from aggressive rotation of the shaft as well as increase the physical range of control authority. The problem of instability arises because there is conflict between force and torque when their combined control effort exceeds what is available. The problem of control authority arises because the bearing capacity is not sufficient to overcome the negative stiffness over the entire air gap. Both of these problems are the effects of input saturation.

6.7.1 Current allocation for force and torque

We consider how to balance the current demands for radial force and torque generation in the presence of input saturation. This problem is inherent among self-bearing motors with

a *common-coil* or *split* winding, meaning that the same coils generate force and torque. It has been recognized in [6], however, that split windings offer flexibility in terms of variable force and torque capacity to meet changing load conditions and make the most efficient use of copper. Be that as it may, few explicit solutions to the force-torque tradeoff have been put forth in the literature for any particular SBM configuration.

We recall the basic operating principles. Assuming $\gamma = 0$, the control force and torque at the home rotor position is given by

$$F_{x,L} = \frac{\sqrt{2}LN_0'P^2m_1}{(P^2-1)m_2}\left(\frac{i_4 - i_2}{2}\right), \tag{6.17a}$$

$$F_{y,L} = \frac{\sqrt{2}LN_0'P^2m_1}{(P^2-1)m_2}\left(\frac{i_1 - i_3}{2}\right), \tag{6.17b}$$

$$\tau = \frac{\pi r LN_0'm_1}{m_2}\left(\frac{i_1 + i_2 + i_3 + i_4}{4}\right). \tag{6.17c}$$

In Chapter 5, we considered how $F_{x,L}, F_{y,L}$ and τ can be obtained in from the control currents i_k, $1 \leqslant k \leqslant 4$. To obtain a unique solution, we imposed the conditions

$$\frac{i_4 - i_2}{2} = i_x, \tag{6.18a}$$

$$\frac{i_1 - i_3}{2} = i_y, \tag{6.18b}$$

$$\frac{i_1 + i_2 + i_3 + i_4}{4} = i_\theta, \tag{6.18c}$$

$$\frac{i_1 + i_3}{4} = \lambda i_\theta, \quad 0 \leq \lambda \leq 1, \tag{6.18d}$$

where λ defines the fraction of total torque generated by the y-axis currents. Thus, i_k are obtained by inverting (6.18):

$$i_1 = 2\lambda i_\theta + i_y, \tag{6.19a}$$

$$i_2 = 2(1-\lambda)i_\theta - i_x, \tag{6.19b}$$

$$i_3 = 2\lambda i_\theta - i_y, \tag{6.19c}$$

$$i_4 = 2(1-\lambda)i_\theta + i_x. \tag{6.19d}$$

Since i_k are physical inputs representative of the three-phase current magnitudes, they are subject to saturation[1]. We define the current saturation, $I_s > 0$, such that $|i_k| \leqslant I_s$. With only saturation of the i_k, conflict between i_x, i_y and i_θ arises. For instance, consider the y-axis where force is generated by Segments 1 and 3. Before saturation we have $i_1^r = 2\lambda i_\theta^r + i_y^r$

[1]This is a somewhat conservative approach since individual phase currents could take on higher amplitudes depending on the phase angle and still remain with saturation limits. But by bounding the amplitudes and not individual phases currents, we can ensure that none of the phases exceed the maximum current level. We can also ensure that our modeling assumptions remain valid so long as the current amplitudes are not saturated.

and $i_3^r = 2\lambda i_\theta^r - i_y^r$ where the superscript r denotes the reference. Suppose that only i_1^r exceeds saturation such that $i_1^r = I_s + \Delta I_s,\ \Delta I_s > 0$. Therefore, $i_1 = I_s = i_1^r - \Delta I_s$, $i_3 = i_3^r$, and

$$i_y = \frac{i_1 - i_3}{2} = i_y^r - \Delta I_s/2. \tag{6.20}$$

Therefore (6.20) shows that the desired radial force control current is reduced by an amount $\Delta I_s/2$. In the worse situation where both i_1^r and i_3^r exceed saturation, for example when $i_\theta \geqslant I_s + |i_y|$, we end up with $i_y = 0$, or a complete loss of control of levitation. Such situations are easy to demonstrate in practice. For example, an angular step response can saturate the controller and lead to insufficient bearing force capacity. Insufficient bearing force capacity can easily lead to instability. Thus, aggressive control of the angular subsystem is problematic with respect to maintaining the system's overall stability. We alleviate this problem in the following way. We restate the saturation constraints as

$$-I_s - i_y \leqslant 2\lambda i_\theta \leqslant I_s - i_y, \tag{6.21a}$$

$$-I_s + i_x \leqslant 2(1-\lambda) i_\theta \leqslant I_s + i_x, \tag{6.21b}$$

$$-I_s + i_y \leqslant 2\lambda i_\theta \leqslant I_s + i_y, \tag{6.21c}$$

$$-I_s - i_x \leqslant 2(1-\lambda) i_\theta \leqslant I_s - i_x. \tag{6.21d}$$

Taking the more conservative bounds, (6.21) becomes

$$-I_s + |i_y| \leqslant 2\lambda i_\theta \leqslant I_s - |i_y|,$$
$$-I_s + |i_x| \leqslant 2(1-\lambda) i_\theta \leqslant I_s - |i_x|,$$

otherwise stated as

$$2\lambda |i_\theta| \leqslant I_s - |i_y|, \tag{6.22a}$$

$$2(1-\lambda)|i_\theta| \leqslant I_s - |i_x|. \tag{6.22b}$$

Next we apply saturation bounds to i_x, i_y and i_θ and give radial force precedence over torque. The reason for this is that the unforced, open-loop rotational subsystem is stable (asymptotically stable if rotor angle velocity is the output), and the levitation subsystem is open-loop unstable. Although insufficient torque generation may impact the control objectives of precision pointing and slewing, it does not impact the stability of the TSBS in closed-loop. On the other hand, insufficient bearing capacity, even momentarily, can lead to instability which is clearly a less desirable result. Therefore we proceed with the assumption that $|i_x|, |i_y| \leqslant I_s$, that is we meet the radial force current references up to saturation.

We then determine how much control effort remains available for torque generation. Based on (6.22), we compute the maximum torque current $\bar{i}_\theta$ obtained from the optimal choice of λ, denoted λ_{op}, from

$$2\lambda_{\text{op}}|\bar{i}_\theta| = I_s - |i_y|, \tag{6.23a}$$

$$2(1-\lambda_{\text{op}})|\bar{i}_\theta| = I_s - |i_x|. \tag{6.23b}$$

Solving for $\lambda, \bar{i}_\theta$ in (6.23) gives

$$\lambda_{\text{op}} = \frac{I_s - |i_y|}{2I_s - |i_x| - |i_y|}, \tag{6.24a}$$

$$\begin{aligned} |\bar{i}_\theta| &= \frac{I_s - |i_y|}{2\lambda_{\text{op}}} \\ &= I_s - \frac{|i_x|}{2} - \frac{|i_y|}{2}. \end{aligned} \tag{6.24b}$$

What $|\bar{i}_\theta|$ represents is a dynamic saturation constraint on i_θ. Equation (6.24b) calculates the available control effort for torque generation without impinging on the control effort necessary to maintain stable levitation. Figure 6.7 shows an example where dynamically constraining i_θ is beneficial. An experimental comparison of two input transformations (ITs) is presented based on a two degree angular step response of the rotor. The first IT is the established approach [120] which encompasses the static four-to-three transformation (6.9) and saturation of the physical inputs, equal to 10 A for our rig. The second IT encompasses the four-to-four transformation (6.19) and the dynamic input saturation (6.24b) giving priority to levitation.

Figures 6.7(a) and 6.7(b) indicate that although both approaches yield a very similar step response, the dynamic IT provides a significant reduction in the peak deviation of the rotor off center (as indicated by the orbital plot). For the controller parameters used in this experiment, larger steps cannot be tolerated by the control system with the static IT because the rotor deviations increase and lead to instability. On the other hand, a step response of arbitrary size is tolerable using the proposed dynamic IT. The reason for the degraded performance in the case of the static IT is apparent from Figure 6.7(c). Figure 6.7(c) shows the reference values and actual values for the input currents, and thus the conflict between force and torque. The reference step commands a high reference value for i_θ which, due to input saturation, causes i_x and i_y to fall of their reference values. In the absence of sufficient levitation control current, the rotor quickly diverges due to the negative stiffness of the rotor. For control using the dynamic IT, it is shown in Figure 6.7(d) that i_x and i_y

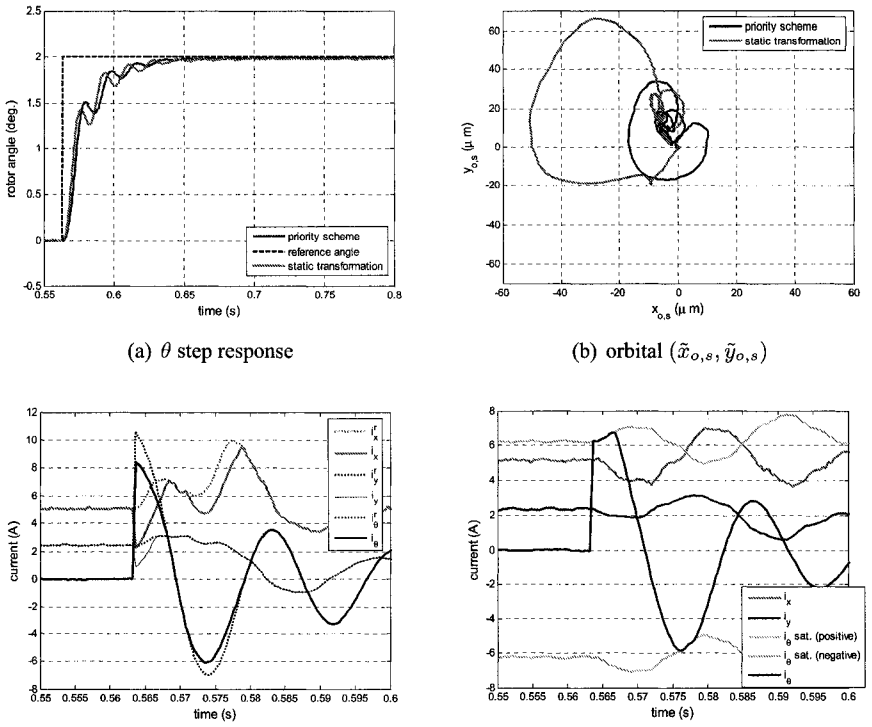

(a) θ step response

(b) orbital $(\tilde{x}_{o,s}, \tilde{y}_{o,s})$

(c) input currents, static transformation

(d) input currents, priority scheme

Figure 6.7: An experimental comparison of two input transformations based on an angular step response. The first is based on [119] which uses a static transformation given by (6.9). The second is a priority scheme given by equations (6.19) and (6.24b). The static transformation creates conflict between the current demands for bearing force and torque when their sum is greater than the available control effort. The priority scheme alleviates this by dynamically constraining i_θ. The priority scheme leads to a significant reduction in the peak deviation of the rotor off center, as indicated by the orbital plot.

track their reference values whereas i_θ is constrained by time-varying saturation levels $\pm\bar{i}_\theta$.

One might expect some degradation in the step response using the dynamic IT because radial force generation is given priority over torque generation. However, this is compensated in good measure by the dynamic IT's ability to maximize torque through the previously unexploited control parameter λ. We show this in Figure 6.8 by comparing the maximum rotational speed, obtained by setting $i_\theta = \bar{i}_\theta$, for $\lambda = \lambda_{\text{op}}$ and $\lambda = 0.5$. Figure 6.8(a) compares the instantaneous rotor speed over time, which varies due to changing demands from the levitation subsystem as well as voltage saturation of the servoamplifiers. On average, a dynamically calculated λ yields an average speed of 601 r/min, while a static

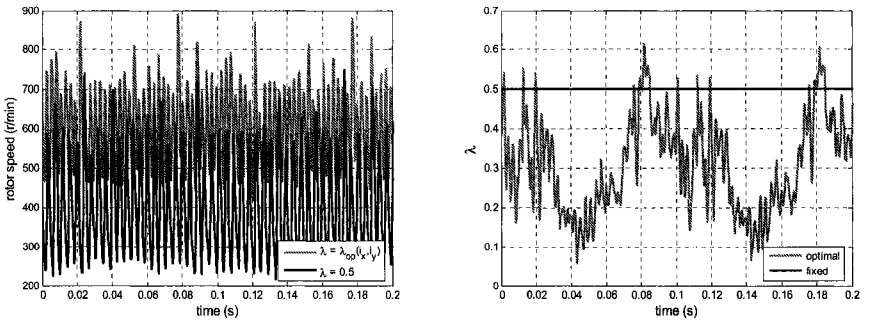

(a) rotor speed

(b) fraction of torque generation from y-axis

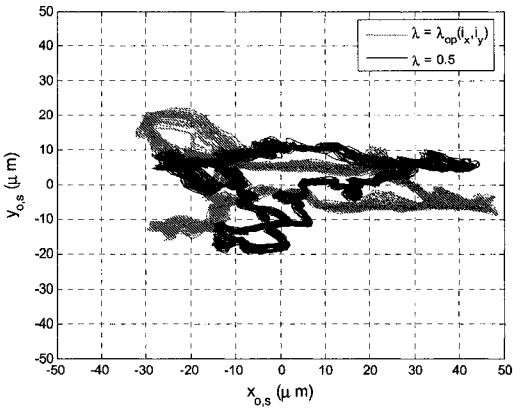

(c) orbital $(\tilde{x}_{o,s}, \tilde{y}_{o,s})$

Figure 6.8: Maximum rotational speed for $\lambda = 0.5$ and for $\lambda = \lambda_{\text{op}}(i_x, i_y)$ as given by (6.24a). The static calculation $\lambda = 0.5$ assumes equal torque generation from all segments whereas a dynamically calculated λ yields allocates torque generation among Segments (1,3) and Segments (2,4). A 49% increase in the average rotor speed results from the latter approach.

setting of $\lambda = 0.5$ yielded an average of 403 r/min; hence a 49% increase. These values of λ are shown in Figure 6.8(b). Figure 6.8(c) shows the corresponding orbitals in both cases, confirming stable levitation.

6.7.2 Decoupled control in a transformed coordinate frame

We now consider the problem of how to eliminate radial force cross-coupling when $\dot{\gamma} \neq 0$. The motivation for this is the possibility of continuously manipulating the phase angle γ while maintaining a simple and familiar model structure for control design. In the next section we show how manipulating γ can be useful; for now we just treat it as a time-varying

parameter bounded such that $\gamma \in (-\pi/(2M), \pi/(2M))$. Dropping sub- and superscript to simplify notation, the levitation subsystem dynamics are re-expressed as

$$\ddot{x} = \frac{\alpha_d}{m}\cos(M\gamma)i_x - \frac{\alpha_c}{m}\sin(M\gamma)i_y + \frac{\alpha_x}{m}x + \frac{F_{c,x}}{m}, \tag{6.25a}$$

$$\ddot{y} = \frac{\alpha_d}{m}\cos(M\gamma)i_y + \frac{\alpha_c}{m}\sin(M\gamma)i_x + \frac{\alpha_x}{m}y + \frac{F_{c,y}}{m}, \tag{6.25b}$$

using the IT from the previous section. The solution to decoupling lies in an appropriate coordinate transformation. One such possibility is

$$\begin{bmatrix} x' \\ y' \\ \dot{x}' \\ \dot{y}' \\ F'_{c,x} \\ F'_{c,y} \end{bmatrix} = \begin{bmatrix} \cos\varphi & \sin\varphi & 0 & 0 & 0 & 0 \\ -\sin\varphi & \cos\varphi & 0 & 0 & 0 & 0 \\ -\sin\varphi\dot{\varphi} & \cos\varphi\dot{\varphi} & \cos\varphi & \sin\varphi & 0 & 0 \\ -\cos\varphi\dot{\varphi} & -\sin\varphi\dot{\varphi} & -\sin\varphi & \cos\varphi & 0 & 0 \\ 0 & 0 & 0 & 0 & \cos\varphi & \sin\varphi \\ 0 & 0 & 0 & 0 & -\sin\varphi & \cos\varphi \end{bmatrix} \begin{bmatrix} x \\ y \\ \dot{x} \\ \dot{y} \\ F_{c,x} \\ F_{c,y} \end{bmatrix}, \tag{6.26}$$

where

$$\varphi = \tan^{-1}\left(\frac{\alpha_c}{\alpha_d}\tan(M\gamma)\right). \tag{6.27}$$

The transformation (6.26) has the form $\xi' = T(\varphi, \dot{\varphi})\xi$. To obtain the dynamics (6.25) in the new coordinate frame we compute

$$\dot{\xi}' = \left(\frac{\mathrm{d}T(\varphi,\dot{\varphi})}{\mathrm{d}t}\xi + T(\varphi,\dot{\varphi})\frac{\mathrm{d}\xi}{\mathrm{d}t}\right)\Big|_{\xi = T^{-1}(\varphi,\dot{\varphi})\xi'}$$

from which we extract dynamic equations without radial force cross-coupling,

$$m\ddot{x}' = \alpha_d\cos(M\gamma)\sqrt{1 + \frac{\alpha_c^2\tan^2(M\gamma)}{\alpha_d^2}}i_x + \alpha_x x' + F'_{c,x} + \dot{\varphi}^2 x' + \ddot{\varphi}y' + 2\dot{\varphi}\dot{y}', \tag{6.28a}$$

$$m\ddot{y}' = \alpha_d\cos(M\gamma)\sqrt{1 + \frac{\alpha_c^2\tan^2(M\gamma)}{\alpha_d^2}}i_y + \alpha_x y' + F'_{c,y} + \dot{\varphi}^2 y' - \ddot{\varphi}x' - 2\dot{\varphi}\dot{x}'. \tag{6.28b}$$

For $\dot{\gamma} = 0$, (6.28) reduces to decoupled equations of motion. The motivation behind the coordinate transformation (6.26)-(6.27) comes from studying the geometry shown in Figure 6.9. This idea is this: as γ is varied, the vector sum of the resulting normal and tangential forces for a given segment is such that it can be viewed as only a tangential force in a transformed frame. By maintaining a coordinate frame such that only tangential forces exist, decoupling in the radial force generation is maintained.

Decoupling through a coordinate transformation has some appeal relative to decoupling by another multi-input, multi-output feedback scheme, such the force feedback followed by

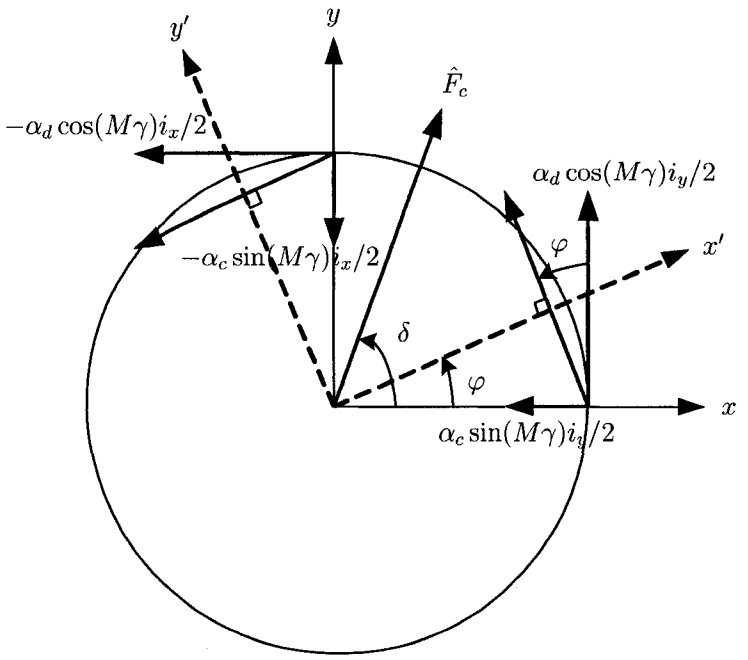

Figure 6.9: Definition of coordinate frames and angles. The angle of the transformed frame relative to the fixed frame, φ, is chosen so that the vector sum of normal and tangential forces in the fixed frame appears only as tangential forces in the transformed frame. $\hat{F}_c$ is the vector sum of the estimated quantities $\hat{F}'_{c,x}$ and $\hat{F}'_{c,y}$.

force-to-current inversion studied in Chapter 2, Section 4. The appeal of our approach is that the equations of motion retain the same structure as (6.10) for $\dot{\gamma} = 0$. Therefore feedback can be designed in terms of familiar quantities instead of auxiliary variables, and a decentralized control design remains valid once transformed, with the exception of possible scaling. For a time-varying phase some complication arises which may require additional terms in the control law. If the phase is slowly varying, one would expect the additional phase-dependent terms in (6.28) to be negligible. In general, the nonlinear state feedback

$$i_x = \frac{-\alpha_x x' - F'_{c,x} - \dot{\varphi}^2 x' - \ddot{\varphi} y' - 2\dot{\varphi}\dot{y}' - K_p m(x' - x'_r) - K_d m\dot{x}'}{\alpha_d \cos(M\gamma)\sqrt{1 + \frac{\alpha_c^2 \tan^2(M\gamma)}{\alpha_d^2}}}, \tag{6.29a}$$

$$i_y = \frac{-\alpha_x y' - F'_{c,y} - \dot{\varphi}^2 y' + \ddot{\varphi} x' + 2\dot{\varphi}\dot{x}' - K_p m(y' - y'_r) - K_d m\dot{y}'}{\alpha_d \cos(M\gamma)\sqrt{1 + \frac{\alpha_c^2 \tan^2(M\gamma)}{\alpha_d^2}}}, \tag{6.29b}$$

$$\varphi = \tan^{-1}\left(\frac{\alpha_c}{\alpha_d}\tan(M\gamma)\right), \tag{6.29c}$$

yields the closed-loop error dynamics $\ddot{e}_x + K_d\dot{e}_x + K_p e_x = 0$ and $\ddot{e}_y + K_d\dot{e}_y + K_p e_y = 0$ which ensures exponential convergence of the setpoint tracking errors $e_x = x' - x'_r, e_y =$

$y' - y'_r$ for $K_p, K_d > 0$. The input parameters (x'_r, y'_r) denote the radial setpoint in the transformed coordinates. The control law (6.29) is position and velocity feedback with constant disturbance cancelation in lieu of error integration in addition to the cancelation of time-varying phase-dependent terms. The corresponding control law for the rotational subsystem is

$$i_\theta = \frac{B\dot{\theta} - T_c - J_z K_{p,\theta}(\theta - \theta_r) - J_z K_{d,\theta}\dot{\theta}}{\alpha_\tau \cos(M\gamma)}$$

for $K_{p,\theta}, K_{d,\theta} > 0$ which ensures asymptotic setpoint tracking of the reference angle θ_r. Implementation of (6.29) assumes the availability of position, velocity, constant disturbances and input derivatives, specifically $\dot{\varphi}$ and $\ddot{\varphi}$. We employ the sixth-order, nonlinear, position-velocity-constant-disturbance (PVCD) observer

$$\dot{\hat{x}}' = \hat{v}'_x + \ell_1(x' - \hat{x}'), \tag{6.30a}$$

$$\dot{\hat{v}}'_x = \frac{(\alpha_x + \dot{\varphi}^2)}{m}x' + \frac{\hat{F}'_{c,x}}{m} + \frac{\ddot{\varphi}}{m}y' + \frac{2\dot{\varphi}}{m}\hat{v}'_y + \frac{\alpha_d \cos(M\gamma)}{m}\sqrt{1 + \frac{\alpha_c^2 \tan^2(M\gamma)}{\alpha_d^2}}\, i_x + \ell_2(x' - \hat{x}'), \tag{6.30b}$$

$$\dot{\hat{F}}'_{c,x} = \ell_3(x' - \hat{x}'), \tag{6.30c}$$

$$\dot{\hat{y}}' = \hat{v}'_y + \ell_4(y' - \hat{y}'), \tag{6.30d}$$

$$\dot{\hat{v}}'_y = \frac{(\alpha_x + \dot{\varphi}^2)}{m}y' + \frac{\hat{F}'_{c,y}}{m} - \frac{\ddot{\varphi}}{m}x' - \frac{2\dot{\varphi}}{m}\hat{v}'_x + \frac{\alpha_d \cos(M\gamma)}{m}\sqrt{1 + \frac{\alpha_c^2 \tan^2(M\gamma)}{\alpha_d^2}}\, i_y + \ell_5(y' - \hat{y}'), \tag{6.30e}$$

$$\dot{\hat{F}}'_{c,y} = \ell_6(y' - \hat{y}'), \tag{6.30f}$$

to estimate velocities $\hat{v}'_x, \hat{v}'_y$ and constant disturbances $\hat{F}'_{c,x}, \hat{F}'_{c,y}$ in the transformed coordinates under the assumption that phase angle derivatives are available. The observer (6.30) has the linear error dynamics

$$\begin{bmatrix} \dot{x}' - \dot{\hat{x}}' \\ \dot{v}'_x - \dot{\hat{v}}'_x \\ \dot{F}_{c,x} - \dot{\hat{F}}'_{c,x} \\ \dot{y}' - \dot{\hat{y}}' \\ \dot{v}'_y - \dot{\hat{v}}'_y \\ \dot{F}_{c,y} - \dot{\hat{F}}'_{c,y} \end{bmatrix} = \begin{bmatrix} -\ell_1 & 1 & 0 & 0 & 0 & 0 \\ -\ell_2 & 0 & \frac{1}{m} & 0 & \frac{2\dot{\varphi}}{m} & 0 \\ -\ell_3 & 0 & 0 & 0 & 0 & 0 \\ 0 & 0 & 0 & -\ell_4 & 1 & 0 \\ 0 & -\frac{2\dot{\varphi}}{m} & 0 & -\ell_5 & 0 & \frac{1}{m} \\ 0 & 0 & 0 & -\ell_6 & 0 & 0 \end{bmatrix} \begin{bmatrix} x' - \hat{x}' \\ v'_x - \hat{v}'_x \\ F_{c,x} - \hat{F}'_{c,x} \\ y' - \hat{y}' \\ v'_y - \hat{v}'_y \\ F_{c,y} - \hat{F}'_{c,y} \end{bmatrix}. \tag{6.31}$$

The zero solution of (6.31) can be made exponentially stable even with the existence of two time-varying entries in the matrix. A simple Lyapunov function argument can show this. The error dynamics (6.31) take the form $\dot{x} = A(t)x$. $A(t)$ is bounded because φ

is effectively an input, statically mapped to γ through (6.27), and has a bounded rate-of-change. Taking

$$V(x) = x^{\mathrm{T}}x = ||x||^2$$

and computing

$$\dot{V}(x) = x^{\mathrm{T}}(A(t) + A^{\mathrm{T}}(t))x = x^{\mathrm{T}}\bar{A}x$$

we see that $\bar{A}$ is time invariant. Since $\bar{A}$ is almost in observer canonical form, choice of the observer gains ℓ_i, $1 \leqslant i \leqslant 6$ is straightforward so that $\bar{A}$ can be made negative definite and $x = 0$ is exponentially stable.

The key assumption in the observer design is the availability of $\dot{\varphi}$ and $\ddot{\varphi}$ since they allow for term cancelation and thus linear error dynamics. In principle, differentiation can provide "fast" enough estimates so that it could be assumed that they are directly measured. Conventional numerical differentiation techniques, however, are problematic in practice because noise is amplified twice to obtain acceleration. Instead, we employ the algebraic derivative (AD) method investigated in Chapter 4 (which is known to have good immunity to noise) to obtain successive time derivatives of a signal. Our derivative estimator is based on a Taylor series truncation order of 6. Applying the design equations (4.13)-(4.15) we get the state equations

$$\dot{\eta}_1 = \eta_2 + 450t^4\varphi, \tag{6.32a}$$

$$\dot{\eta}_2 = \eta_3 - 2400t^3\varphi, \tag{6.32b}$$

$$\dot{\eta}_3 = \eta_4 + 5400t^2\varphi, \tag{6.32c}$$

$$\dot{\eta}_4 = \eta_5 - 4320t\varphi, \tag{6.32d}$$

$$\dot{\eta}_5 = 720\varphi, \tag{6.32e}$$

as well as the output equations

$$\dot{\varphi}_e = -\frac{\eta_1 - 30t^5\varphi}{t^6}, \tag{6.33a}$$

$$\ddot{\varphi}_e = -\frac{\eta_2 + 300t^4\varphi - 24t^5\dot{\varphi}_e}{t^6}, \tag{6.33b}$$

where $\dot{\varphi}_e, \ddot{\varphi}_e$ denote the estimates of the first and second derivatives of φ. To achieve sufficient accuracy on a continual basis, overlapping estimators are employed in the manner described in Chapter 4, Section 2.3. The combination of time-shifted AD estimation with the PVCD observer yields an overall sixteenth order estimator for the levitation subsystem.

6.7.3 Phase-based control

Having established stabilizing feedback that permits a time-varying phase angle, we turn our attention to a feedback law for γ to achieve additional performance benefits. Setting $\gamma \neq 0$ creates normal forces on the rotor in addition to tangential forces and as such, phase angle manipulation allows us to freely orient the force that each segment applies to the rotor. The useful implication of this fact is that the axes of maximum bearing capacity can be freely oriented as well. This can be seen from the Lorentz force model where the angle of the axis of maximum bearing capacity (in the first and third quadrants) relative to the x-axis is given by

$$\tan^{-1}\left(\frac{F_y}{F_x}\right)\Big|_{i_x=i_y} = \tan^{-1}\left(\frac{\alpha_d\cos(M\gamma)+\alpha_c\sin(M\gamma)}{\alpha_d\cos(M\gamma)-\alpha_c\sin(M\gamma)}\right),$$

and is only a function of γ. By contrast, AMBs have fixed axes of maximum bearing capacity. For instance, the radial axes of an AMB supporting a horizontal shaft are typically aligned at 45 degrees to the horizon so that they absorb gravity in equal measure. Such AMBs can absorb a greater load along the horizontal and vertical axes than along the axes of force generation.

An advantage of being able to orient the axes of maximum bearing capacity is that we can maintain balanced loads among segments in spite of the direction of loading or the position of the rotor. Since the PVCD observers generate radial loading estimates, phase-based control offers the possibility of active load balancing by orientation of the axes of maximum bearing capacity. Our approach is to convert the estimates $\hat{F}'_{c,x}, \hat{F}'_{c,y}$ to polar coordinates to determine the angle δ of the axis of disturbance force relative to the x-axis. This is given by

$$\delta = \tan^{-1}\left(\frac{\hat{F}_{c,y}}{\hat{F}_{c,x}}\right) = \tan^{-1}\left(\frac{\hat{F}'_{c,y}}{\hat{F}'_{c,x}}\right) + \varphi \tag{6.34}$$

and is shown graphically in Figure 6.9. Then, we align the axes of maximum bearing capacity with the axis of disturbance force by solving

$$\delta = \tan^{-1}\left(\frac{F_y}{F_x}\right)\Big|_{i_x=i_y} = \tan^{-1}\left(\frac{\alpha_d\cos(M\gamma)+\alpha_c\sin(M\gamma)}{\alpha_d\cos(M\gamma)-\alpha_c\sin(M\gamma)}\right)$$

for $0 < \delta < \pi/2$ (quadrants 1 and 3) and

$$\delta = \tan^{-1}\left(\frac{F_y}{F_x}\right)\Big|_{i_x=-i_y} = \tan^{-1}\left(\frac{-\alpha_d\cos(M\gamma)+\alpha_c\sin(M\gamma)}{\alpha_d\cos(M\gamma)+\alpha_c\sin(M\gamma)}\right).$$

for $-\pi/2 < \delta \leqslant 0$ (quadrants 2 and 4). The solution is

$$\gamma = \begin{cases} \frac{1}{M}\tan^{-1}\left(\frac{\alpha_d}{\alpha_c}\frac{\tan(\delta)+1}{1-\tan(\delta)}\right), & -\pi/2 < \delta \leqslant 0 \\ \frac{1}{M}\tan^{-1}\left(\frac{\alpha_d}{\alpha_c}\frac{\tan(\delta)-1}{\tan(\delta)+1}\right), & 0 < \delta < \pi/2. \end{cases} \tag{6.35}$$

Equation (6.35) is discontinuous at $\delta = 0$ and at the boundary between $\delta = \pi/2$ and $\delta = -\pi/2$ because δ is restricted to two quadrants in its computation. Because of the bi-directionality of Lorentz-force generation, disturbance forces in all four quadrants are compensated. Restricting δ to two quadrants is in fact desirable because it minimizes the bound on γ which is also the torque angle. From (6.35) the bound is $|\gamma| < \tan^{-1}\left(\frac{\alpha_d}{\alpha_c}\right)/M$, corresponding to $|\gamma| < 5.03\,\text{deg}$ based on parameter values from Table 6.2. This corresponds to a 23% reduction in the torque-to-current ratio in the worst case based on Figure 6.6(a). Nonetheless, this tradeoff buys the levitation subsystem the ability to extend its region of operation and an example below shows this. A good approximation to (6.35) is

$$\gamma = \frac{1}{M}\tan^{-1}\left(\frac{\alpha_d}{\alpha_c}\tan\left(\text{sign}(\delta)\left(|\delta| - \frac{\pi}{4}\right)\right)\right). \tag{6.36}$$

The approximation is good in the sense that, if one plots γ versus δ based on Table 6.2 parameters, the discrepancy is less than 1%. Geometrically speaking, (6.36) positions the axis of disturbance exactly between the x' and y' axes. In doing so, it sets $F'_{c,x} = F'_{c,y}$ which in turn guarantees $i_x = i_y$ in steady state. This fact simply follows from (6.28a)–(6.28b), which reduces to equal and independent equations of motion for a centered rotor. For a non-centered rotor, current equalization results form computing δ due to both the negative stiffness and constant disturbances:

$$\delta = \tan^{-1}\left(\frac{\alpha_x y' + \hat{F}'_{c,y}}{\alpha_x x' + \hat{F}'_{c,x}}\right) + \phi. \tag{6.37}$$

Altogether, the phase-based control law is (6.36) followed by (6.37). Implementating (6.36)–(6.37) requires additional provisions. Because (6.36) is discontinuous, we subject γ to a slew rate limit to make the function continuous and ensure φ has a sufficiently low rate-of-change. As a result, we avoid excessive control effort to suppress the phase velocity and phase acceleration dependent terms in (6.28). In addition, (6.36)-(6.37) contain an algebraic loop which we break by insertion of a delay element. The existence of feedback within the phase control law does not pose any concerns it terms of its stability. This is because although it appears that the computation of δ is a function of γ, it is in fact not. Equation (6.34) makes this point clear by showing that δ depends only on operating conditions in the fixed frame. The computation of δ has the form $\delta = \kappa(\gamma) + \varphi(\gamma)$ and the computation of γ in one step re-apportions δ between κ and φ such that $\kappa = \pi/4$. A block diagram of the closed-loop system is given in Figure 6.10.

An example where phase-based control is useful is upon startup. When the TSBS portion of the rotor is de-levitated, there is insufficient bearing capacity to lift it when $\gamma = 0$

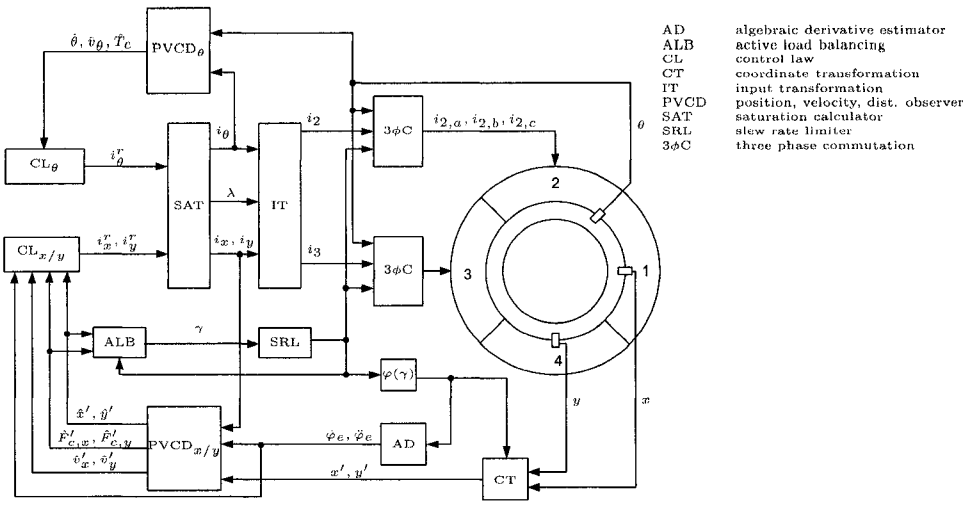

Figure 6.10: A block diagram of the toothless self-bearing servomotor under closed-loop control. A legend on the right describes each block. The control system consists of state observers, state feedback control laws, dynamic constraining of the control inputs, fast derivative estimation, a current equalization loop, and commutation of twelve phases. The three-phase commutation (3ϕC) blocks to segments 1 and 4 are omitted for clarity of presentation.

due to gravity as well as the negative stiffness which exists when the shaft is delevitated. This problem is shown in Figure 6.11 which focuses in on the y-axis. Before lift-off, we observe in Figure 6.11(a) that the shaft remains at rest while in Figure 6.11(b) the input current is saturated. A manual increase in γ from 0 deg to 1.5 deg, also shown in Figure 6.11(b), provides the additional lift necessary for startup.

Figure 6.12 demonstrates active load balancing. For this experiment the rotor tracks the reference

$$
\begin{aligned}
x_r &= 100\cos\left(\frac{\pi t}{2}\right)\ \mu\text{m}, \\
y_r &= 100\sin\left(\frac{\pi t}{2}\right)\ \mu\text{m}, \\
\theta_r &= 0,
\end{aligned}
$$

which is shown in Figure 6.12(a). At about 5.4 s, active load balancing is engaged. At this point, as it is shown in Figure 6.12(c), γ goes from a nominal value of 0 deg to being a function of the changing radial loads. Figure 6.12(d) shows the loads $\alpha_x x' + F'_{c,x}$ and $\alpha_x y' + F'_{c,y}$ being equalized. More important, Figure 6.12(b) shows the control currents becoming equalized resulting in a 26% drop in the peak value of i_y. The extra signal headroom made available by balancing expands the stable operating range of the device

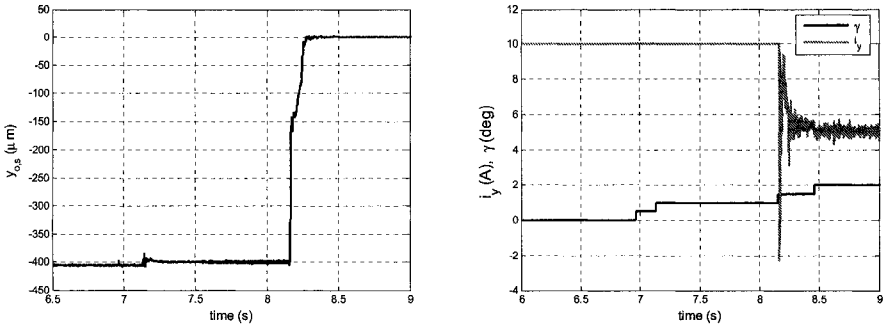

(a) y-axis rotor position

(b) y-axis current and γ

Figure 6.11: Startup levitation of the toothless self-bearing servomotor. Due to insufficient bearing capacity at $\gamma = 0$, the control current i_y is saturated and the rotor remains at rest on the y-axis. A manual increase in γ provides the additional lift necessary for startup.

and reduces its susceptibility to transient disturbances.

Figures 6.12(e) and 6.12(f) show the outputs of the AD estimator, $\dot{\varphi}_e$ and $\ddot{\varphi}_e$, obtained from $\epsilon = 0.2$ s. Due to the slew-rate limiting of γ to ± 25 deg/s the resulting magnitude of phase velocity and phase acceleration dependent terms in the control law are kept small. For instance, based on the magnitude of values in Figures 6.12(a) and 6.12(f), the control effort associated with the terms $\ddot{\varphi}_e x$ and $\ddot{\varphi}_e y$ in (6.29) have an order of magnitude of 10^{-3} A. The slew rate limiter also leads to γ overshooting its theoretical maximum of 5.03 deg, leading to a slight and temporary unbalance in the loads and currents. However, γ still stays well within acceptable bounds and slew-rate limiting is shown to ease the transient when active load balancing is engaged.

6.8 Conclusion

A generalized dynamic model and an improved control design for a TSBS is derived and validated. A priority scheme is established with respect to the actuator's two functions - levitation and torque generation - and torque production is maximized by optimizing a previously unutilized control variable. We design an estimated state feedback in a transformed coordinate to permit phase-based control. Phase-based control is shown to enable input current equalization, independent of rotor position and the direction of loading, by positioning the axes of maximum bearing capacity. In the next chapter we reduce the hardware requirements of the TSBS by realizing its functionality with two segments instead of four.

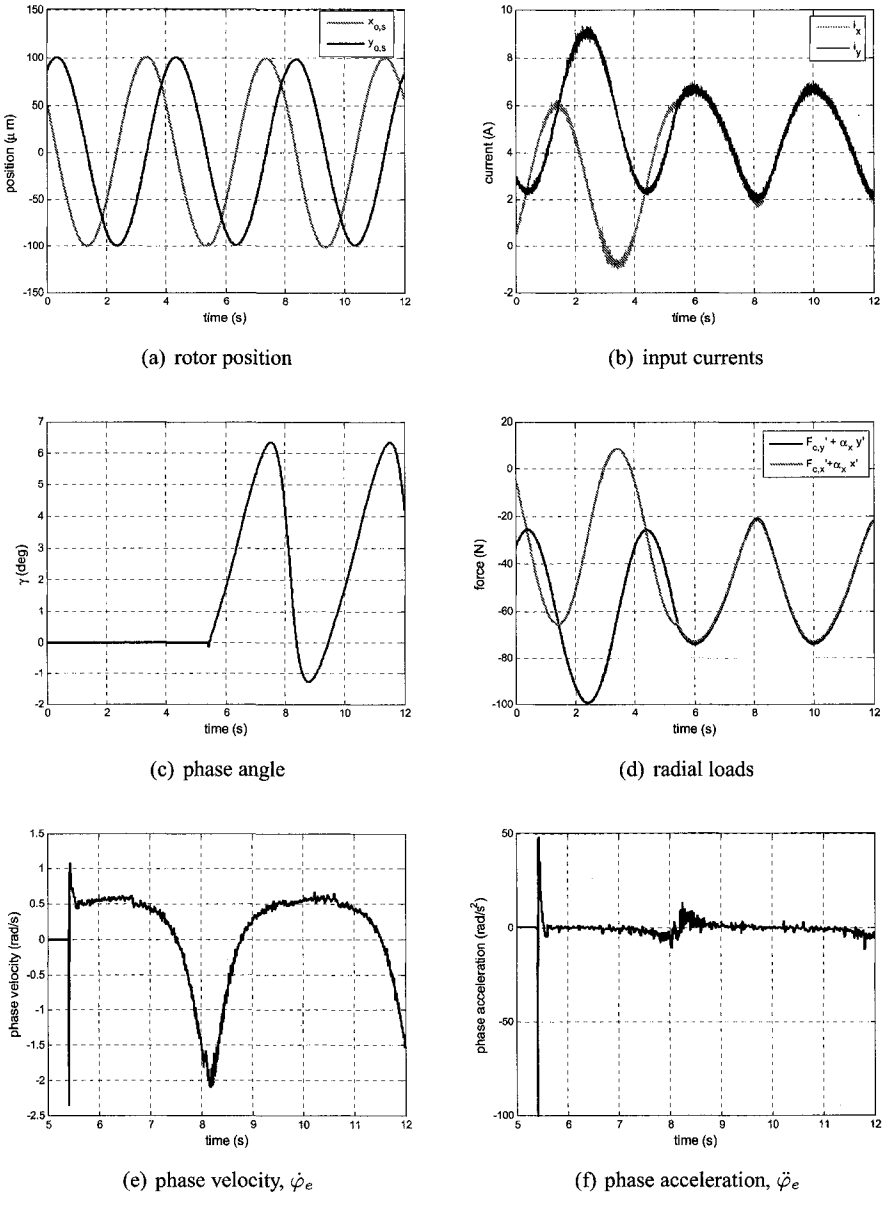

(a) rotor position

(b) input currents

(c) phase angle

(d) radial loads

(e) phase velocity, $\dot{\varphi}_e$

(f) phase acceleration, $\ddot{\varphi}_e$

Figure 6.12: Active load balancing. The rotor center follows a circular trajectory of radius 100 μm and a frequency of 0.25 Hz. At about 5.4 s active load balancing is engaged, equalizing the currents and recovering input signal headroom.

Chapter 7

Redesign of a Toothless Self-Bearing Servomotor

We are motivated by phase-based control developed in Chapter 6 to redesign the toothless self-bearing servomotor (TSBS). The TSBS configuration considered in Chapters 5 and 6 consists of four segments and therefore twelve phases. Manipulating the phase angle so that normal forces are applied to the rotor in addition to tangential forces, we present the concept and prove the feasibility of a six-phase TSBS in this chapter. We adapt the dynamic model and control techniques of the twelve-phase system to the six-phase system. The design is validated on the experimental twelve-phase test rig by driving pairs of segments with common inputs.

The resulting six-phase design reduces the necessary drive circuitry by a factor of two (roughly), and brings the hardware requirements of the TSBS more in line with that of typical self-bearing motors (SBMs). The majority of hybrid-type SBMs, those which utilize the Maxwell force for levitation and the Lorentz force for rotation, are realized with either five or six phases [16]. Hybrid-type SBMs with single-phase motoring characteristics have been realized with as few as four phases [113]. All other previously-proposed all-Lorentz SBMs are, to the author's knowledge, six-phase machines. The TSBS is therefore at a clear disadvantage relative to its counterparts in terms of its electrical complexity and, ultimately, cost.

7.1 Description

Figure 7.1 shows the cross-section of a sixteen-pole, six-phase TSBS. In comparison to its original twelve-phase conception, the six-phase TSBS can be viewed as the connection of the windings of Segments 1 and 2 in series, and the connection of the windings of Segments

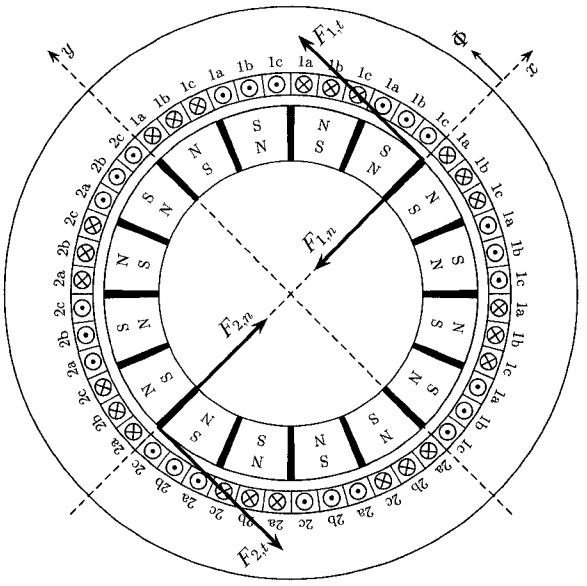

Figure 7.1: Cross-section of a six-phase, toothless self-bearing servomotor (TSBS). The six-phase TSBS has two segments, each of which can generate a normal and a tangential force on the rotor. These are the forces $F_{1,t}, F_{1,n}, F_{2,t}$ and $F_{2,n}$.

3 and 4 in series. The two segments generate tangential forces $F_{1,t}, F_{2,t}$ and normal forces $F_{1,n}, F_{2,n}$ on the rotor. The tangential forces control motion along the y-axis as well as rotation, whereas the normal forces only control motion along the x-axis. Tangential and normal forces from each segment are generated by manipulation of the amplitude and phase of its associated three-phase winding.

7.2 Force and torque characteristics

Deriving expressions for radial force and torque follows from the approach previously described in Chapters 5 and 6. We introduce the stationary $x-y$ coordinate system as shown in Figure 7.1. The stator angle Φ is defined relative to the x-axis in the counterclockwise direction.

Expressions for radial gap flux density due to the PMs (5.8) and winding distribution (5.2) remain the same. We redefine the segmentation according to the stator angle Φ by

$$\pi\left(k-\frac{3}{2}\right) \leqslant \Phi_k < \pi\left(k-\frac{1}{2}\right), \quad 1 \leqslant k \leqslant 2,$$

and drive the windings with the following three-phase currents

$$i_{k,a}(i_k, \gamma_1, \theta) = i_k \cos\left(M(\theta + \gamma_k) - \frac{\pi}{3}\right), \tag{7.1a}$$

$$i_{k,b}(i_k, \gamma_1, \theta) = i_k \cos\left(M(\theta + \gamma_k)\right), \tag{7.1b}$$

$$i_{k,c}(i_k, \gamma_1, \theta) = i_k \cos\left(M(\theta + \gamma_k) + \frac{\pi}{3}\right), \tag{7.1c}$$

for $k = 1, 2$. Thus, the four control variables are the current magnitudes i_1, i_2 and phase angle offsets γ_1, γ_2 for Segments 1 and 2, respectively. The resulting current distribution for the k^{th} segment is

$$I_k(\Phi, \theta, i_k, \gamma_k) = N_0' i_k \sin\left[M\left(\Phi - \theta - \gamma_k\right)\right],$$

and the associated air-gap flux distribution due to the windings is

$$B_{g,w,k}(x, y, \Phi, \theta, i_k, \gamma_k) = \frac{w_1 i_k \cos[M(\Phi - \theta - \gamma_k)]}{w_2 - x\cos\Phi - y\sin\Phi}.$$

Expressions for force and torque arise from the Lorentz-force integrals

$$F_{x,L}(x, y, \theta, i_k, \gamma_k) = L\sum_{k=1}^{2}\int_{l_k}^{u_k} B_{g,m}(\Phi) I_k(\Phi)\sin\Phi \mathrm{d}\Phi, \tag{7.2a}$$

$$F_{y,L}(x, y, \theta, i_k, \gamma_k) = -L\sum_{k=1}^{2}\int_{l_k}^{u_k} B_{g,m}(\Phi) I_k(\Phi)\cos\Phi \mathrm{d}\Phi, \tag{7.2b}$$

$$\tau_L(x, y, \theta, i_k, \gamma_k) = -rL\sum_{k=1}^{2}\int_{l_k}^{u_k} B_{g,m}(\Phi) I_k(\Phi) \mathrm{d}\Phi, \tag{7.2c}$$

and Maxwell-force integrals

$$F_{x,M}(x, y, \theta, i_k, \gamma_k) = \frac{rL}{2\mu_0}\sum_{k=1}^{2}\int_{l_k}^{u_k} (B_{g,m}(\Phi) + B_{g,w,k}(\Phi))^2 \cos\Phi \, \mathrm{d}\Phi, \tag{7.3a}$$

$$F_{y,M}(x, y, \theta, i_k, \gamma_k) = \frac{rL}{2\mu_0}\sum_{k=1}^{2}\int_{l_k}^{u_k} (B_{g,m}(\Phi) + B_{g,w,k}(\Phi))^2 \sin\Phi \, \mathrm{d}\Phi, \tag{7.3b}$$

with the limits of integration now defined by $l_k = (k - 3/2)\pi$ and $u_k = (k - 1/2)\pi$. Using the approach in Chapter 6, we evaluate the integrals (7.2)-(7.3) and retain the dominant negative stiffness term as well as all terms associated with the home rotor position $(x, y, \theta) = 0$. The approximate expressions for force and torque are

$$F_x(x, i_k, \gamma_k) = \alpha_n\left(\frac{\sin(M\gamma_2)i_2 - \sin(M\gamma_1)i_1}{2}\right) + \alpha_x x, \tag{7.4a}$$

$$F_y(y, i_k, \gamma_k) = \alpha_t\left(\frac{\cos(M\gamma_1)i_1 - \cos(M\gamma_2)i_2}{2}\right) + \alpha_x y, \tag{7.4b}$$

$$\tau(i_k, \gamma_k) = \alpha_\tau\left(\frac{\cos(M\gamma_1)i_1 + \cos(M\gamma_2)i_2}{2}\right), \tag{7.4c}$$

where α_t, α_n denote the tangential and normal current-to-force gains, α_x is the negative stiffness gain, and α_τ is the torque constant.

7.3 Dynamic model and parameter identification

We employ the same experimental test bench as described in Chapter 6, Section 3, to assess the feasibility of the proposed six-phase design. We use the existing twelve-phase TSBS to emulate a six-phase TSBS by driving Segments 1 and 2 with the same three-phase currents, and by driving Segments 3 and 4 with the same three-phase currents. As a result, the $x-y$ frame of the six-phase TSBS is positioned 45 degrees counterclockwise relative to the $x-y$ frame of the twelve-phase TSBS.

Adapting the force and torque expressions (7.4) to the dynamic model derived in Chapter 6, Section 4 gives

$$m'\ddot{x} = \alpha_n \left(\frac{\sin(M\gamma_2)i_2 - \sin(M\gamma_1)i_1}{2} \right) + \alpha'_x x + F_{c,x}, \tag{7.5a}$$

$$m'\ddot{y} = \alpha_t \left(\frac{\cos(M\gamma_1)i_1 - \cos(M\gamma_2)i_2}{2} \right) + \alpha'_x y + F_{c,y}, \tag{7.5b}$$

$$J_z\ddot{\theta} = \alpha_\tau \left(\frac{\cos(M\gamma_1)i_1 + \cos(M\gamma_2)i_2}{2} \right) - B\dot{\theta} + T_c, \tag{7.5c}$$

with effective mass m', negative stiffness coefficient α'_x, bias forces $F_{c,x}, F_{c,y}$, and bias torque T_c. The dynamic model remains sixth order but now has four inputs $i_1, i_2, \gamma_1, \gamma_2$, and three outputs x, y, θ. Note that x, y are the radial displacements of the rotor in the new $x-y$ coordinate system of the measurement plane and are related to the physical measurements $\tilde{x}_{o,s}, \tilde{y}_{o,s}$ by the relations

$$x = \cos\left(\frac{\pi}{4}\right)\tilde{x}_{o,s} + \sin\left(\frac{\pi}{4}\right)\tilde{y}_{o,s}, \tag{7.6a}$$

$$y = \cos\left(\frac{\pi}{4}\right)\tilde{x}_{o,s} - \sin\left(\frac{\pi}{4}\right)\tilde{y}_{o,s}. \tag{7.6b}$$

Having re-oriented the x- and y-axes 45 degrees counterclockwise, it results that

$$\alpha_t = \sqrt{2}\alpha_d,$$

$$\alpha_n = \sqrt{2}\alpha_c,$$

where α_d, α_c are the direct and cross-coupled current-to-force constants identified in Chapter 6. All other parameters remain the same as previously identified in Table 6.2.

7.4 Control

7.4.1 Decoupling via $d-q$ control

By control of the current magnitudes i_k and phase angles γ_k, we apply $d-q$ decomposition theory [65] and a further input transformation to decouple the equations of motion (7.5). The $d-q$ decomposition is introduced in conventional motors to remove time-varying inductances from the electrical dynamic equations and to isolate the stator current component responsible for torque generation. We define

$$i_{d,1} = \sin(M\gamma_1)i_1, \tag{7.7a}$$

$$i_{d,2} = \sin(M\gamma_2)i_2, \tag{7.7b}$$

$$i_{q,1} = \cos(M\gamma_1)i_1, \tag{7.7c}$$

$$i_{q,2} = \cos(M\gamma_2)i_2, \tag{7.7d}$$

where $i_{d,1}, i_{d,2}$ control the normal forces generated by Segments 1 and 2 respectively, and $i_{q,1}, i_{q,2}$ control the tangential forces responsible for torque. As such, the six-phase currents (7.1) are related to (7.7) by a variation[1] of the standard $d-q$ transformation. Specifically, it holds that

$$\begin{bmatrix} i_{q,k} \\ i_{d,k} \\ i_{0,k} \end{bmatrix} = K \begin{bmatrix} i_{a,k} \\ i_{b,k} \\ i_{c,k} \end{bmatrix} \tag{7.8}$$

for $k = 1, 2$. The homopolar current $i_{0,k} = 0$ and

$$K = \frac{2}{3} \begin{bmatrix} \cos\left(M\theta - \frac{\pi}{3}\right) & \cos\left(M\theta\right) & \cos\left(M\theta + \frac{\pi}{3}\right) \\ -\sin\left(M\theta - \frac{\pi}{3}\right) & -\sin\left(M\theta\right) & -\sin\left(M\theta + \frac{\pi}{3}\right) \\ \frac{1}{\sqrt{2}} & -\frac{1}{\sqrt{2}} & \frac{1}{\sqrt{2}} \end{bmatrix}. \tag{7.9}$$

The six-phase currents are computed from the $d-q$ currents via

$$\begin{bmatrix} i_{a,k} \\ i_{b,k} \\ i_{c,k} \end{bmatrix} = K^{-1} \begin{bmatrix} i_{q,k} \\ i_{d,k} \\ i_{0,k} \end{bmatrix} \tag{7.10}$$

where

$$K^{-1} = \begin{bmatrix} \frac{1}{2}\left(\cos\left(M\theta\right) + \sqrt{3}\sin\left(M\theta\right)\right) & \frac{1}{2}\left(\sqrt{3}\cos\left(M\theta\right) - \sin\left(M\theta\right)\right) & \frac{1}{\sqrt{2}} \\ \cos\left(M\theta\right) & -\sin\left(M\theta\right) & -\frac{1}{\sqrt{2}} \\ \frac{1}{2}\left(\cos\left(M\theta\right) - \sqrt{3}\sin\left(M\theta\right)\right) & \frac{1}{2}\left(-\sqrt{3}\cos\left(M\theta\right) - \sin\left(M\theta\right)\right) & \frac{1}{\sqrt{2}} \end{bmatrix}.$$

In fact, an analysis similar to that given above also holds for the twelve-phase TSBS. In Chapters 5 and 6, the current magnitudes i_k, $1 \leq k \leq 4$ are the q-axis components of stator current and no d-axis components are assumed to exist since $\gamma = 0$.

[1] The variation in our $d-q$ transformation is due to the $\pi/3$ phase spacing of our winding arrangement instead of the more common $2\pi/3$ phase spacing.

Substitution of the $d-q$ currents (7.7) into the dynamic model (7.5) gives

$$m'\ddot{x} = \alpha_n \left(\frac{i_{d,2} - i_{d,1}}{2} \right) + \alpha'_x x + F_{c,x}, \tag{7.11a}$$

$$m'\ddot{y} = \alpha_t \left(\frac{i_{q,1} - i_{q,2}}{2} \right) + \alpha'_x y + F_{c,y}, \tag{7.11b}$$

$$J_z\ddot{\theta} = \alpha_\tau \left(\frac{i_{q,1} + i_{q,2}}{2} \right) - B\dot{\theta} + T_c. \tag{7.11c}$$

Individual control of force and torque in (7.11) requires a further input transformation that gives

$$\left(\frac{i_{d,2} - i_{d,1}}{2} \right) = i_x, \tag{7.12a}$$

$$\left(\frac{i_{q,1} - i_{q,2}}{2} \right) = i_y, \tag{7.12b}$$

$$\left(\frac{i_{q,1} + i_{q,2}}{2} \right) = i_\theta. \tag{7.12c}$$

Equations (7.12b)-(7.12c) uniquely specify i_y and i_θ in terms of $i_{q,1}, i_{q,2}$ whereas (7.12a) is overspecified by $i_{d,1}, i_{d,2}$. As one approach, we set $i_{d,2} = -i_{d,1}$ whereby $i_{d,1}, i_{d,2}, i_{q,1}, i_{q,2}$ are recovered from i_x, i_y, i_θ by

$$i_{d,1} = -i_x, \tag{7.13a}$$

$$i_{d,2} = i_x, \tag{7.13b}$$

$$i_{q,1} = i_\theta - i_y, \tag{7.13c}$$

$$i_{q,2} = i_\theta + i_y. \tag{7.13d}$$

With this further input transformation, the dynamic model (7.11) becomes

$$\begin{aligned} m'\ddot{x} &= \alpha_n i_x + \alpha'_x x + F_{c,x}, \\ m'\ddot{y} &= \alpha_t i_y + \alpha'_x y + F_{c,y}, \\ J_z\ddot{\theta} &= \alpha_\tau i_\theta - B\dot{\theta} + T_c. \end{aligned}$$

For simplicity, we complete the control design by decoupled proportional-plus-integral-plus-derivative (PID) control laws

$$i_x = -K_p(x_r - x) - K_i \int_0^t (x_r(\tau) - x(\tau))\mathrm{d}\tau - K_d \frac{\mathrm{d}}{\mathrm{d}t}(x_r - x), \tag{7.14a}$$

$$i_y = -K_p(y_r - y) - K_i \int_0^t (y_r(\tau) - y(\tau))\mathrm{d}\tau - K_d \frac{\mathrm{d}}{\mathrm{d}t}(y_r - y), \tag{7.14b}$$

$$i_\theta = -K_{p,\theta}(\theta_r - \theta) - K_{i,\theta} \int_0^t (\theta_r(\tau) - \theta(\tau))\mathrm{d}\tau - K_{d,\theta} \frac{\mathrm{d}}{\mathrm{d}t}(\theta_r - \theta). \tag{7.14c}$$

7.4.2 Priority scheme

As discussed in Chapter 6, the TSBS generates radial force and torque from a common set of windings. Since the coil currents are subject to a saturation level, conflict can arise between the force needed to maintain stable levitation and the torque need to rotate the shaft. In chapter 6, a dynamic saturation scheme was established in which the reference currents to the levitation subsystem are given priority over the reference current to the rotational subsystem. This idea is founded on the fact that insufficient bearing capacity destabilizes the entire system whereas insufficient torque capacity does not.

We consider now the design of a priority scheme for the six-phase TSBS. We impose actuator saturation as a constraint on the amplitudes of each segment's three-phase currents such that $i_1, i_2 \leqslant I_s$, where $I_s > 0$ is the saturation current level. Bounding of the current amplitudes i_k can be otherwise stated as

$$\begin{aligned} i_{d,1}^2 + i_{q,1}^2 &\leqslant I_s^2, \\ i_{d,2}^2 + i_{q,2}^2 &\leqslant I_s^2, \end{aligned}$$

and, following substitution of (7.13), as

$$\begin{aligned} (-i_x)^2 + (i_\theta - i_y)^2 &\leqslant I_s^2, \\ i_x^2 + (i_\theta + i_y)^2 &\leqslant I_s^2. \end{aligned}$$

Assuming that $i_x^2 + i_y^2 < I_s^2$, which implies that the levitation subsystem is not saturated in the absence of torque generation, we have

$$i_\theta^2 + 2i_y i_\theta + i_x^2 + i_y^2 - I_s^2 \leqslant 0, \tag{7.15a}$$

$$i_\theta^2 - 2i_y i_\theta + i_x^2 + i_y^2 - I_s^2 \leqslant 0. \tag{7.15b}$$

We equate the constraints (7.15a)-(7.15b) to calculate the bounds on i_θ. Doing so gives

$$\bar{i}_\theta^2 + 2i_y \bar{i}_\theta + i_x^2 + i_y^2 - I_s^2 = 0, \tag{7.16a}$$

$$\bar{i}_\theta^2 - 2i_y \bar{i}_\theta + i_x^2 + i_y^2 - I_s^2 = 0, \tag{7.16b}$$

where $\bar{i}_\theta$ denotes a saturation value of i_θ. The solutions to the quadratic equations (7.16a)-(7.16b) are

$$\bar{i}_\theta = -i_y \pm \sqrt{I_s^2 - i_x^2}, \tag{7.17a}$$

$$\bar{i}_\theta = i_y \pm \sqrt{I_s^2 - i_x^2}. \tag{7.17b}$$

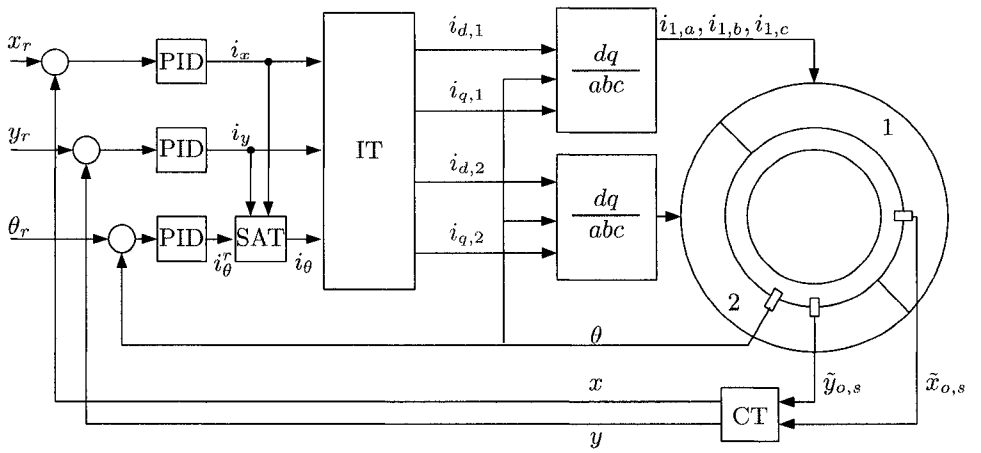

Figure 7.2: Block diagram of the six-phase TSBS under closed-loop control. We define the following acronyms: CT is the coordinate transformation given by (7.6); IT is the input transformation given by (7.13); $dq \rightarrow abc$ is the transformation (7.10); PID is the feedback control law given by (7.14); SAT is the dynamic saturation given by (7.18).

The intersection of (7.17a)-(7.17b) gives the range of feasible values for i_θ as a function of i_x and i_y. Therefore, i_θ is bounded above and below by $\bar{i}_\theta, -\bar{i}_\theta$ respectively where

$$\bar{i}_\theta = \mid |i_y| - \sqrt{I_s^2 - i_x^2} \mid. \tag{7.18}$$

Figure 7.2 is a block diagram of the closed-loop system showing the interconnection of the feedback control law, priority scheme, input transformation, and commutation.

7.5 Experimental validation

We confirm the theory of a six-phase TSBS on the existing twelve-phase TSBS test rig which is described in detail in Chapter 6, Section 3. The current setup is not identical to an actual six-phase system because it is still driven by twelve servoamplifiers. Therefore the inductances and resistances of the coils would be twice as large in an actual six-phase prototype as it is in the present setup. Since the coils are current driven, only an increase in inductance is potentially problematic because it degrades the bandwidth of the current controllers (see Chapter 2, Section 1 for an explanation). We do not expect this degradation to be significant for the TSBS because a doubling of the nominal coil inductance of our toothless machine would still make it comparable to that of AMBs.

Experimentation confirms that all the basic functionality of the twelve-phase TSBS can be realized with only six phases, i.e. lift off, precision pointing and slewing, and conventional motoring. Figure 7.3(a) shows the rotor's response to a 15 degree angular step

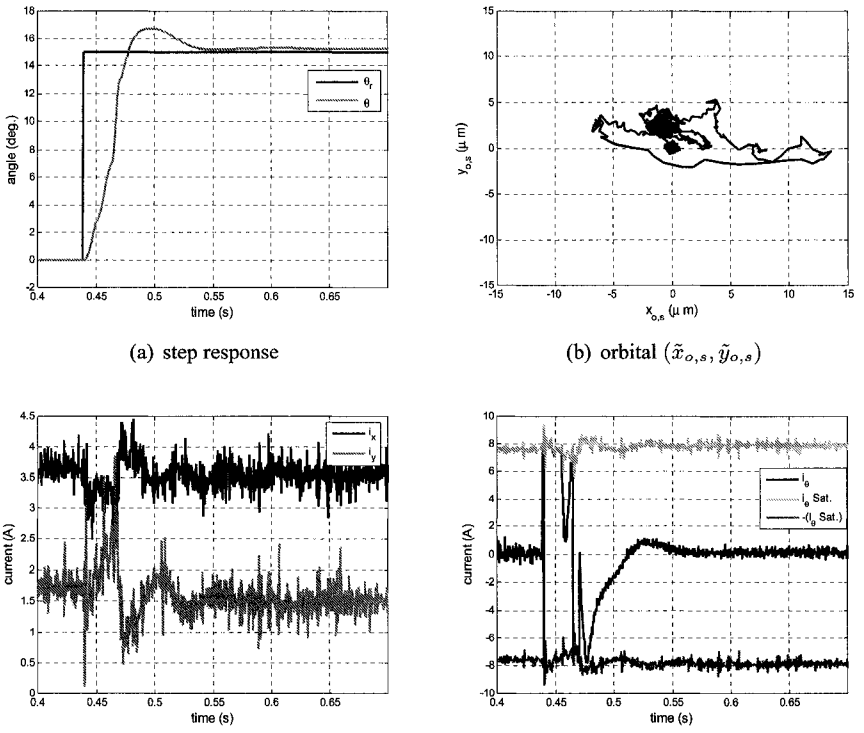

(a) step response

(b) orbital $(\tilde{x}_{o,s}, \tilde{y}_{o,s})$

(c) inputs to levitation subsystem

(d) input to rotational subsystem

Figure 7.3: 15 degree angular step response of a six-phase TSBS.

reference. Figures 7.3(c) and 7.3(d) show the effectiveness of the priority scheme since i_θ is bounded by a time-varying constraint which is dependent upon i_x, i_y. From the orbital plot in Figure 7.3(b) it is further evident that the levitation subsystem is unaffected by the current demands of the rotational subsystem.

7.6 Conclusion

The TSBS is redesigned so that its functionality can be realized with six phases instead of twelve. This is shown to be possible in principle through normal force generation on the rotor in addition to tangential force generation. A control scheme is synthesized which manipulates both the magnitude and phase angle of each segment's windings. In addition, we reformulate the priority scheme from Chapter 6 which gives precedence to levitation over torque generation. Experiments confirm the feasibility of the six-phase approach, and its advantages are in simplifying the physical design and hardware requirements of the TSBS.

Chapter 8

Conclusions

8.1 Summary of contributions

This thesis has described contributions to the modeling, control, and design of contactless electromagnetic actuators, namely active magnetic bearings (AMBs) and toothless self-bearing servomotors (TSBS). The contributions are listed below.

1. An experimental comparison of trajectory tracking control laws for a non-rotating shaft levitated by AMBs confirms the feasibility of applying nonlinear control theory subject to various actuating constraints. This experimental study demonstrates the dependence of dynamic performance on the AMBs' bias current level in a nonlinear context.

2. A nonlinear trajectory tracking control law is synthesized for a rotating shaft levitated by AMBs. The innovation lies in the hierarchical state observer design which estimates synchronous vibration. Experiments show that the proposed control design achieves synchronous vibration suppression as well as wide-air-gap motion tracking at high rotational speeds.

3. An alternative basis to state estimation using algebraic differentiation (AD) is numerically analyzed to assess its accuracy. The AD method is shown to be effective in a simulated application to an AMB as well as in a real-time application to the TSBS.

4. The nonlinear bearing force and torque characteristics of a TSBS are obtained from first principle analysis. Parameters are identified and the resulting model is validated by means of finite element analysis. Our model achieves comparable accuracy to more complex modeling approaches, and is more general than previous modeling approaches which always resulted in linearized expressions.

5. A dynamic model for the TSBS is derived which generalizes its actuating principle and incorporates the phase angle γ as a potential control variable.

6. A feedback controller for the TSBS is designed to mitigate the force-torque conflict inherent in its common-coil winding scheme and to extend its physical range of control authority. A priority scheme is devised which resolves the force-torque conflict, and phase-based control is shown to maximize the TSBS's force-generating capability for general operating conditions.

7. A six-phase design for a TSBS is presented. This design requires half of the phases, and hence half of the drive electronics, of the TSBS considered in this thesis. The principle of the six-phase TSBS is derived through vector control of each segment. An equivalent priority scheme is devised in the six-phase case, and the overall concept is experimentally confirmed.

8.2 Future work

The work in this thesis has opened up some potential avenues of future research. They are described in this section.

8.2.1 Adaptive vibration control for AMBs

The problem of vibration control of AMBs is a relatively mature topic of research but it remains an interesting and relevant case study for the application of adaptive control theory. Vibration in AMBs can arise either from mass unbalance, sensor runout, or resonance. Control systems which compensate these effects usually require knowledge of the discrete frequency or frequencies associated with these various forms of vibration. Typically this knowledge is obtained from measurement or by assumption.

Recent work in the field of adaptive control theory [77] has led to an observer which can globally estimate an arbitrary number of discrete sinusoids from a measured signal. This algorithm can be applied to determine the synchronous speed for an adaptive disturbance observer design, and to estimate resonances in real time as a basis for notch filter tuning.

8.2.2 Pointing and slewing characterization of the TSBS

The angular tracking performance of the TSBS deserves further consideration since it is a key performance specification. In particular, we are concerned with the actuator's ability

to track low frequency angular references as well as its pointing precision and accuracy. Reference [100] provides a number of benchmark tests for the TSBS.

Although toothless machines are theoretically devoid of detent, it is apparent from experimentation that the rotor "catches" at certain angular positions. This is demonstrated in Figure 8.1(a) where the rotor angle tracks a low frequency sinusoid reference. Figure 8.1(b) shows a close up where the tracking error significantly deviates at a discrete angle. Figure 8.1(c) shows how the tracking error gets worse with an increase of the frequency of the reference. Detent is a potentially severe detriment to meeting the stringent angular positioning requirements required for its intended applications. It would be worthwhile to study the root cause of this effect and devise compensation either through advanced feedback or commutation.

8.2.3 Conventional motor operation of the TSBS

The TSBS is fundamentally a servo-drive, but operating it as a conventional motor is potentially useful to further characterize it in terms of its power and efficiency. Constant speed operation is a challenge with a common coil winding scheme since the availability of torque is subject to the demands on the levitation subsystem. Fluctuations in speed also result from voltage saturation of the servoamplifiers, so the electrical dynamics of the TSBS must be considered as well.

8.2.4 All-Lorentz slice SBMs

In the field of SBMs, arguably the most industrially relevant route to pursue further study would have to do with the slice motor concept [109]. The self-bearing slice motor, as discussed in Chapter 1, Section 3, actively stabilizes three degrees of freedom like most other SBMs, but also passively stabilizes the remaining three degrees of freedom. Most self-bearing slice motors are of the hybrid type. Efforts to develop a slice SBM using the all-Lorentz approach are nascent [89] and warrant further investigation because of their potential advantages which are discussed in the introduction of Chapter 5.

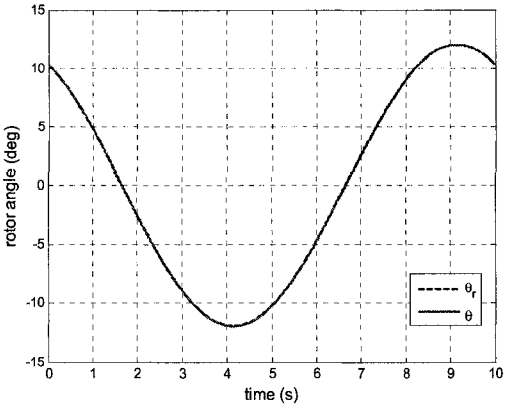

(a) tracking a 0.1 Hz sinusoid

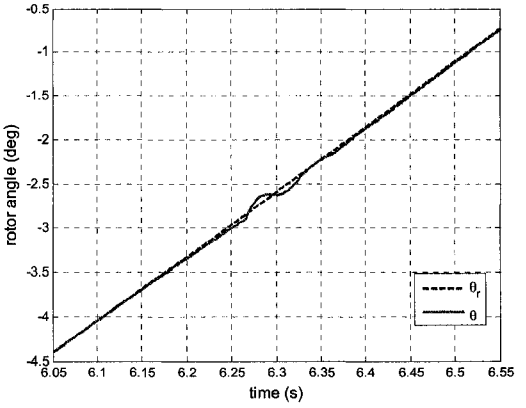

(b) detent

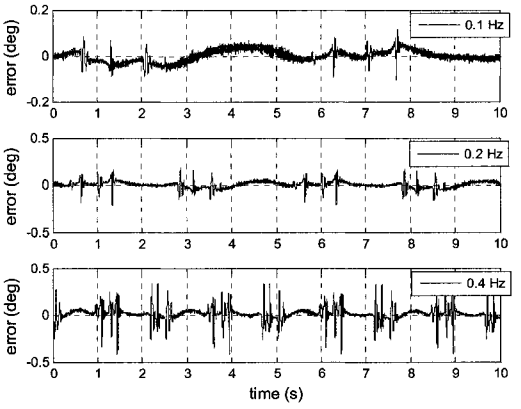

(c) tracking error for various reference frequencies

Figure 8.1: Slewing performance of the toothless self-bearing servomotor. As the rotor angle tracks a sinusoidal reference, the rotor "catches" at discrete angles, degrading the tracking error.

Bibliography

[1] International Symposium on Magnetic Bearings (ISMB) Paper titles and authors. Available at http://www.rotordynamics.org/ISMB.htm.

[2] SKF Magnetic Bearings. http://www.skfmagneticbearings.com.

[3] *IEEE Transactions on Control Systems Technology*, 4(5), Sep. 1996.

[4] *JSME International Journal, Series C*, 46(2), Sep. 2003.

[5] M. Ahrens, L. Kučera, and R. Larsonneur. Performance of a magnetically suspended flywheel energy storage device. *IEEE Transactions on Control Systems Technology*, 4(5):494–502, Sep. 1996.

[6] W. Amrhein, S. Silber, K. Nenninger, G. Trauner, M. Reisinger, and R. Schoeb. Developments on bearingless drive technology. *JSME International Journal, Series C*, 46(2):343–348, Sep. 2003.

[7] C. Barthod and G. Lemarquand. Design of an actuator being both a permanent magnet synchronous motor and a magnetic suspension. In *Proceedings of IEEE International Magnetics Conference*, pages BR–05, Apr. 1997.

[8] F. Betschon and C. R. Knospe. Reducing magnetic bearing currents via gain scheduled adaptive control. *IEEE/ASME Transactions on Mechatronics*, 6(4):437–443, Dec. 2001.

[9] J. Bichsel. The bearingless electrical machine. In *Proceedings of the International Symposium on Magnetic Suspension and Technology'91, NASA Publication 3152*, pages 561–573, Langley Research Center, Hampton, VA, 1991.

[10] H. Bleuler. A survey of magnetic levitation and magnetic bearing types. *JSME International Journal, Series C*, 35(3):335–342, 1992.

[11] H. Bleuler, C. Gähler, R. Herzog, R. Larsonneur, T. Mizuno, R. Siegwart, and S.-J. Woo. Application of digital signal processors for industrial magnetic bearings. *IEEE Transactions on Control Systems Technology*, 2(4):280–289, Dec. 1994.

[12] K. Bornstein. Dynamic load capabilities of active electromagnetic bearings. *Transactions of the ASME, Journal of Tribology*, 113:598–603, Jul. 1991.

[13] A. Charara, J. De Miras, and B. Caron. Nonlinear control of a magnetic levitation system without premagnetization. *IEEE Transactions on Control Systems Technology*, 4(5):513–523, Sep. 1996.

[14] B. Charlet, J. Lévine, and R. Marino. On dynamic feedback linearization. *Systems and Control Letters*, 13(2):143–151, 1989.

[15] A. Chiba, T. Deido, T. Fukao, and M. A. Rahman. An analysis of bearingless AC motors. *IEEE Transactions on Energy Conversion*, 9(1):61–68, Mar. 1994.

[16] A. Chiba, T. Fukao, O. Ichikawa, M. Oshima, M. Takemoto, and D. G. Dorell. *Magnetic Bearings and Bearingless Drives*. Newnes (Elsevier), Burlington, MA, 2005.

[17] A. Chiba, D. T. Power, and M. A. Rahman. Characteristics of a bearingless induction motor. *IEEE Transactions on Magnetics*, pages 5199–5201, Sep. 1991.

[18] A. Chiba, M. A. Rahman, and T. Fukao. Radial force in a bearingless reluctance motor. *IEEE Transactions on Magnetics*, 27(2):786–790, Mar. 1991.

[19] S. K. Chung, C. R. Koch, and A. F. Lynch. Flatness-based feedback control of an automotive solenoid valve. *IEEE Transactions on Control Systems Technology*, 15(2):394–401, Mar. 2007.

[20] C. Collon. Studienarbeit [internship] report. University of Alberta, Edmonton, AB, Canada, 2004.

[21] C. Collon. Estimating time derivatives by algebraic differentiation using a truncated Taylor series expansion. Technical report, University of Alberta, Edmonton, AB, Canada, 2005.

[22] C. Collon, S. Eckhardt, and J. Rudolph. A network approach to the modelling of active magnetic bearings. *Mathematical and Computer Modelling of Dynamical Systems*, 13:455–469, 2007.

[23] D. Carroll and J. Sedgewick. Integrated magnetic bearing, Patent 6707200, March 2004.

[24] M. S. de Queiroz and D. M. Dawson. Nonlinear control of active magnetic bearings: A backstepping approach. *IEEE Transactions on Control Systems Technology*, 4(5):545–552, Sep. 1996.

[25] S. Diop, J. W. Grizzle, and F. Chaplais. On numerical differentiation algorithms for nonlinear estimation. In *Proceedings of the 39th IEEE Conference on Decision and Control*, pages 1133–1138, Sydney, Australia, Dec. 2000.

[26] S. Diop, J. W. Grizzle, P. E. Moraal, and A. Stefanopoulou. Interpolation and numerical differentiation for observer design. In *Proceedings of the 1994 American Control Conference*, pages 1329–1333, Baltimore, MD, Jun. 1994.

[27] S. Eckhardt and J. Rudolph. High precision synchronous tool path tracking with an AMB machine tool spindle. In *Proceedings of the Ninth International Symposium on Magnetic Bearings*, Lexington, KY, Aug. 2004. paper no. 109.

[28] S. Eckhardt and J. Rudolph. Trajectory tracking for a magnetically levitated shaft with three-phase AMBs in Y-connection. In *Proceedings of the Tenth International Symposium on Magnetic Bearings*, Martigny, Switzerland, Aug. 2006. 6 pages.

[29] M. Fliess. Analyse non standard du bruit. *Comptes Rendus Mathematique*, 342:797–802, 2006.

[30] M. Fliess, C. Join, M. Mboup, and H. Sira-Ramírez. Compression différentielle de transitoires bruités. *Comptes Rendus Mathematique*, 339:821–826, 2004.

[31] M. Fliess, C. Join, M. Mboup, and H. Sira-Ramírez. Analyse et représentation de signaux transitoires: application à la compression, au débruitage et a la détection de ruptures. In *Actes 20e coll. GRETSI*, Louvain-la-Neuve, France, 2005. Available at http://hal.inria.fr/inria-00001115.

[32] M. Fliess, J. Lévine, P. Martin, and P. Rouchon. Flatness and defect of nonlinear systems: introductory theory and applications. *International Journal of Control*, 61(6):1327–1361, Jun. 1995.

[33] M. Fliess, J. Lévine, P. Martin, and P. Rouchon. A Lie-Bäcklund approach to equivalence and flatness of nonlinear systems. *IEEE Transactions on Automatic Control*, 44(5):922–937, May 1999.

[34] M. Fliess and H. Sira-Ramírez. Control via state estimations of some nonlinear systems. In *Proceedings of the Sixth IFAC NOLCOS Conference*, pages 66–73, Stuttgart, Germany, Sep. 2004.

[35] M. Fliess and H. Sira-Ramírez. Reconstructeurs d'états. *Comptes Rendus Mathematique*, 338:91–96, 2004.

[36] G. T. Flowers, G. Szász, V. S. Trent, and M. E. Greene. A study of integrally augmented state feedback control for an active magnetic bearing supported rotor system. *Transactions of the ASME, Journal of Engineering for Gas Turbines and Power*, 123:377–382, Apr. 2001.

[37] J. P. Gauthier, H. Hammouri, and I. Kupka. Observers for nonlinear systems. In *Proceedings of the 30th IEEE Conference on Decision and Control*, pages 1483–1489, Brighton, England, 1991.

[38] A. Gensior, O. Woywode, J. Rudolph, and H. Guldner. On differential flatness, trajectory planning, observers, and stabilization for DC-DC converters. *IEEE Transactions on Circuits and Systems I: Regular Papers*, 53(9):2000–2010, Sep. 2006.

[39] G. Genta, L. Mazzocchetti, and E. Rava. Magnetic suspension for a turbomolecular pump. In *Proceedings of the Second International Symposium on Magnetic Bearings*, Tokyo, Japan, Jul. 1990.

[40] H. Grabner, W. Amrhein, S. Silber, and K. Nenninger. Nonlinear feedback control of a bearingless brushless DC motor. In *Proceedings of the Sixth International Conference on Power Electronics and Drive Systems*, pages 366–371, Kuala Lumpur, Malaysia, Nov. 2005.

[41] T. R. Grochmal, C. P. Forbrich, and A. F. Lynch. Modeling and nonlinear control of a toothless self-bearing motor. In *Proceedings of the Fourth International Symposium on Stability Control of Rotating Machinery*, pages 259–271, Calgary, AB, Aug. 2007.

[42] T. R. Grochmal, C. P. Forbrich, and A. F. Lynch. Nonlinear bearing force and torque model for a toothless self-bearing servomotor. *IEEE Transactions on Magnetics*, 44(7):1805–1814, Jul. 2008.

[43] T. R. Grochmal and A. F. Lynch. Control of a contactless servomotor: active load balancing by Lorentz-force levitation. Submitted to *IEEE Control System Magazine*, May 2008.

[44] T. R. Grochmal and A. F. Lynch. Nonlinear control of an active magnetic bearing with bias currents: experimental study. In *Proceedings of the 2006 American Control Conference*, pages 4558–4563, Minneapolis, MN, Jun. 2006.

[45] T. R. Grochmal and A. F. Lynch. Vibration compensation and precision tracking of a rotating shaft by nonlinear state feedback. In *Proceedings of the Tenth International Symposium on Magnetic Bearings*, Martigny, Switzerland, Aug. 2006. 6 pages.

[46] T. R. Grochmal and A. F. Lynch. An experimental comparison of nonlinear tracking controllers for active magnetic bearings. *Control Engineering Practice*, 7(1):93–107, Jan. 2007.

[47] T. R. Grochmal and A. F. Lynch. A numerical analysis of the algebraic derivative method with application to magnetic bearings. In *Proceedings of the 46th IEEE Conference on Decision and Control*, pages 1021–1026, New Orleans, LA, Dec. 2007.

[48] T. R. Grochmal and A. F. Lynch. Precision tracking of a rotating shaft with magnetic bearings by nonlinear decoupled disturbance observers. *IEEE Transactions on Control Systems Technology*, 15(6):1112–1121, Nov. 2007.

[49] S. K. Agrawal H. Sira-Ramírez. *Differentially Flat Systems*. CRC Press, New York, NY, 2004.

[50] D. Hanselman. *Brushless Permanent Magnet Motor Design*. The Writers' Collective, Cranston, RI, 2nd edition, 2003.

[51] R. Herzog, P. Bühler, C. Gähler, and R. Larsonneur. Unbalance compensation using generalized notch filters in the multivariable feedback of magnetic bearings. *IEEE Transactions on Control Systems Technology*, 4(5):580–586, Sep. 1996.

[52] T. Higuchi, T. Mizuno, and M. Tsukamoto. Digital control system for magnetic bearings with automatic balancing. In *Proceedings of the Second International Symposium on Magnetic Bearings*, pages 27–32, Tokyo, Japan, Jul. 1990.

[53] T. Hu, Z. Lin, and P. E. Allaire. Reducing power loss in magnetic bearings by optimizing current allocation. *IEEE Transactions on Magnetics*, 40(3):1625–1635, May 2004.

[54] A. Isidori. *Nonlinear Control Systems*. Springer Verlag, New York, NY, 2nd edition, 1989.

[55] C. Join, H. Sira-Ramírez, and M. Fliess. Control of an uncertain three-tank system via on-line parameter identification and fault detection. In *Proc.* 16^{th} *IFAC World Congress*, Prague, Czech Republic, Jul. 2005. Paper Code We-A03-Tp/1.

[56] S. Joo and J. H. Seo. Design and analysis of the nonlinear feedback linearizing control for an electromagnetic suspension system. *IEEE Transactions on Control Systems Technology*, 5(1):135–144, Jan. 1997.

[57] H. Kanebako and Y. Okada. New design of hybrid-type self-bearing motor for small, high-speed spindle. *IEEE/ASME Transactions on Mechatronics*, 8(1):111–119, Mar. 2003.

[58] H. K. Khalil. *Nonlinear Systems*. Prentice Hall, New York, 3rd edition, 2002.

[59] A. Kharitonov and O. Sawodny. Optimal flatness based control for heating processes in the glass industry. In *Proceedings of the 43rd IEEE Conference on Decision and Control*, pages 2435–2440, Paradise Island, Bahamas, Dec. 2004.

[60] M. Kim, T. Higuchi, T. Mizuno, and H. Hara. Application of a magnetic bearing spindle to non-circular fine boring. In *Proceedings of the Sixth International Symposium on Magnetic Bearings*, pages 22–31, Cambridge, MA, Aug. 1998.

[61] S. J. Kim, K. Abe, H. Kanebako, Y. Okada, and C. W. Lee. A Lorentz force type self-bearing motor with new 4-pole winding configuration. In *Proceedings of the Eight International Symposium on Magnetic Bearings*, pages 35–40, Mito, Japan, Aug. 2002.

[62] W.-J. Kim, D. L. Trumper, and J. H. Lang. Modeling and vector control of a planar magnetic levitator. *IEEE Transactions on Industry Applications*, 34(6):1254–1262, Nov./Dec. 1998.

[63] C. R. Knospe. Active magnetic bearings for machining applications. *Control Engineering Practice*, 15(3):307–313, Mar. 2007.

[64] C. R. Knospe, W. Hope, S. J. Fedigan, and R. D. Williams. Experiments in the control of unbalance response using magnetic bearings. *Mechatronics*, 5(4):385–400, Jun. 1995.

[65] P. C. Krause, O. Wasynczuk, and S. D. Sudhoff. *Analysis of Electric Machinery and Drive Systems*. Wiley-Interscience, New Jersey, 2nd edition, 2002.

[66] A. J. Krener and W. Respondek. Nonlinear observers with linear error dynamics. *SIAM Journal on Control and Optimization*, 23(2):197–216, Mar. 1985.

[67] J. Lévine, J. Lottin, and J.-C. Ponsart. A nonlinear approach to the control of magnetic bearings. *IEEE Transactions on Control Systems Technology*, 4(5):524–544, Sep. 1996.

[68] L. Li. Linearizing magnetic bearing actuators by constant current sum, constant voltage sum, and constant flux sum. *IEEE Transactions on Magnetics*, 35(1):528–535, Jan. 1999.

[69] L. Li and J. Mao. Feedback linearisation of magnetic bearing actuators for a uniform upper bound of force slew rate. *IEE Proceedings-Electric Power Applications*, 146(4):378–382, Jul. 1999.

[70] M. Li, J. Chiasson, M. Bodson, and L. M. Tolbert. A differential-algebraic approach to speed estimation in an induction motor. *IEEE Transactions on Automatic Control*, 51(7):1172–1177, Jul. 2006.

[71] J. D. Lindlau and C. R. Knospe. Feedback linearization of an active magnetic bearing with voltage control. *IEEE Transactions on Control Systems Technology*, 10(1):21–31, Jan. 2002.

[72] L. Ljung. *System Identification: Theory for the user*. Prentice Hall, Upper Saddle River, NJ, 2nd edition, 1999.

[73] J. Lottin, P. Mouille, and J.-C. Ponsart. Nonlinear control of active magnetic bearings. In *Proceedings of the Fourth International Symposium on Magnetic Bearings*, pages 101–106, Zürich, Switzerland, Aug. 1994.

[74] K.-Y. Lum, V. T. Coppola, and D. S. Bernstein. Adaptive autocentering control for an active magnetic bearing supporting a rotor with unknown mass imbalance. *IEEE Transactions on Control Systems Technology*, 4(5):587–597, Sep. 1996.

[75] P. Mai and C. Hillermeier. New insights into derivative estimation via least squares approximation - theory and application. In *Proceedings of the 2008 American Control Conference*, pages 2427–2434, Seattle, WA, Jun. 2008.

[76] R. Marino and P. Tomei. *Nonlinear Control Design: Geometric, Adaptive and Robust*. Prentice Hall Europe, Hertfordshire, UK, 1995.

[77] R. Marino and P. Tomei. Global estimation of n unknown frequencies. *IEEE Transactions on Automatic Control*, 47(8):1324–1328, Aug. 2002.

[78] P. Martin, R. M. Murray, and P. Rouchon. Flat systems, equivalence and trajectory generation. Technical Report CaltechCDSTR:2003.008, Caltech, Pasadena, CA, 2003.

[79] E. H. Maslen, P. Hermann, M. A. Scott, and R. R. Humpris. Practical limits to the performance of magnetic bearings: Peak force, slew rate, and displacement sensitivity. *Transactions of the ASME, Journal of Tribology*, 111(2):331–336, Apr. 1989.

[80] F. Matsumura, M. Fujita, and K. Okawa. Modeling and control of magnetic bearing systems achieving a rotation around the axis of inertia. In *Proceedings of the Second International Symposium on Magnetic Bearings*, Tokyo, Japan, Jul. 1990.

[81] F. Matsumura and T. Yoshimoto. System modeling and control design of a horizontal-shaft magnetic-bearing system. *IEEE Transactions on Magnetics*, 22(3):196–203, May 1986.

[82] D. C. Meeker. *Optimal Solutions to the Inverse Problem in Quadratic Magnetic Actuators*. PhD thesis, University of Virginia, Charlottesville, VA, 1996.

[83] B. Möller. Using high-speed electrospindles with active magnetic bearings for boring of non-circular shapes. In *Proceedings of the Second International Symposium on Magnetic Bearings*, pages 189–196, Tokyo, Japan, 1990.

[84] T. Nakamura, M. Hirata, and K. Nonami. Zero bias H_∞ control of active magnetic bearings for energy storage flywheel systems. In *Proceedings of the Ninth International Symposium on Magnetic Bearings*, Lexington, KY, Aug. 2004. paper No. 134.

[85] M. Neff, N. Barletta, and R. Schöb. Bearingless centrifugal pump for highly pure chemicals. In *Proceedings of the Eight International Symposium on Magnetic Bearings*, pages 283–287, Mito, Japan, Aug. 2002.

[86] S. B. Nichols, S. Jagannathan, K. Leary, D. Eisenhaure, W. Stanton, R. Hockney, J. Downer, and V. Gondhalekar. Integrated magnetic levitation and rotation system, Patent 5818137, October 1998.

[87] Y. Okada. Self-bearing motor- key technology to implantable artificial heart pump. In *Proceedings of the Ninth International Symposium on Magnetic Bearings*, Lexington, KY, Aug. 2004.

[88] Y. Okada, K. Dejima, and T. Ohishi. Analysis and comparison of PM synchronous motor and induction motor type magnetic bearings. *IEEE Transactions on Industry Applications*, 31(4):1047–1053, Sep./Oct. 1995.

[89] Y. Okada, T. Jinbu, N. Yamashiro, and K. Sagawa. Lorentz-type self bearing motor using halback magnets. In *Proceedings of the Tenth International Symposium on Magnetic Bearings*, Martigny, Switzerland, Aug. 2006.

[90] Y. Okada, H. Konishi, H. Kanebako, and C.-W. Lee. Lorentz force type self-bearing motor. In *Proceedings of the Seventh International Symposium on Magnetic Bearings*, pages 353–358, ETH Zurich, Switzerland, Aug. 2000.

[91] Y. Okada, S. Miyamoto, and T. Ohishi. Levitation and torque control of internal permanent magnet type bearingless motor. *IEEE Transactions on Control Systems Technology*, 4(5):565–571, Sep. 1996.

[92] M. Ooshima, A. Chiba, T. Fukao, and M. A. Rahman. Design and analysis of permanent magnet-type bearingless motors. *IEEE Transactions on Industrial Electronics*, 43(2):292–299, Apr. 1996.

[93] M. Ooshima, S. Miyazawa, A. Chiba, F. Nakamura, and T. Fukao. Performance evaluation and test results of a 11,000 r/min, 4 kW surface-mounted permanent magnet-type bearingless motor. In *Proceedings of the Seventh International Symposium on Magnetic Bearings*, pages 377–382, ETH Zürich, Switzerland, Aug. 2000.

[94] R. B. Owen, M. Maggiore, and J. Apkarian. A high-precision, magnetically levitated positioning stage: Toward contactless actuation for industrial manufacturing. *IEEE Control Systems Magazine*, 26(3):82–95, Jun. 2006.

[95] S.-H. Park and C.-W. Lee. Lorentz-force type integrated motor-bearing system in dual rotor disk configuration. *IEEE/ASME Transactions on Mechatronics*, 10(6):618–625, 2005.

[96] Philips Applied Technologies. Magnetic levitation planar technology backgrounder, 2006. Available at http://www.apptech.philips.com/html/press_center/.

[97] C. Redemann, P. Meuter, A. Ramella, and T. Gempp. 30 kW Bearingless canned motor pump on the test bed. In *Proceedings of the Seventh International Symposium on Magnetic Bearings*, pages 189–194, ETH Zürich, Switzerland, Aug. 2000.

[98] J. Reger, P. Mai, and H. Sira-Ramírez. Robust algebraic state estimation of chaotic systems. In *Proceedings of the 2006 Conference on Control Applications*, pages 326–331, Munich, Germany, Oct. 2006.

[99] J. Reger, H. Sira-Ramírez, and M. Fliess. On non-asymptotic observation of nonlinear systems. In *Proceedings of the 44th IEEE Conference on Decision and Control*, pages 4219–4224, Seville, Spain, Dec. 2005.

[100] Z. Ren. *Model, Control and Performance of a Six Degree-of-Freedom Precision Pointing and Tracking System*. PhD thesis, University of Kentucky, Lexington, KY, 2005.

[101] Z. Ren and L. S. Stephens. Closed-loop performance of a six degree-of-freedom precision magnetic actuator. *IEEE/ASME Transactions on Mechatronics*, 10(6):666–674, Dec. 2005.

[102] Z. Ren and L. S. Stephens. Force characteristics and gain determination for a slotless self-bearing motor. *IEEE Transactions on Magnetics*, 42(7):1849–1860, Jul. 2006.

[103] Z. Ren, L. S. Stephens, and A. V. Radun. Improvements on winding flux models for a slotless self-bearing motor. *IEEE Transactions on Magnetics*, 42(7):1838–1848, Jul. 2006.

[104] A. E. Rundell, S. V. Drakunov, and R. A. DeCarlo. A sliding mode observer and controller for stabilization of rotational motion of a vertical shaft magnetic bearing. *IEEE Transactions on Control Systems Technology*, 4(5):598–608, Sep. 1996.

[105] N. K. Rutland, P. S. Keogh, and C. R. Burrows. Comparison of controller designs for attenuation of vibration in a rotor-bearing system under synchronous and transient conditions. In *Proceedings of the Fourth International Symposium on Magnetic Bearings*, pages 107–112, Zürich, Switzerland, Aug. 1994.

[106] M. N. Sahinkaya and A. E. Hartavi. Variable bias current in magnetic bearings for energy optimization. *IEEE Transactions on Magnetics*, 43(3):1052–1060, Mar. 2007.

[107] A. O. Salazar, A. Chiba, and T. Fukao. A review of developments in bearingless motors. In *Proceedings of the Seventh International Symposium on Magnetic Bearings*, pages 335–340, ETH Zürich, Switzerland, Aug. 2000.

[108] C. Samiappan, N. Mirnateghi, B. E. Paden, and J. F. Antaki. Maglev apparatus for power minimization and control of artificial hearts. *IEEE Transactions on Control Systems Technology*, 16(1):13–18, Jan. 2008.

[109] R. Schöb. Centrifugal pump without bearings or seals. *World Pumps*, pages 2–5, Jul. 2002.

[110] R. Schöb, N. Barletta, A. Fleischli, G. Foiera, T. Gempp, V. L. Poirier, D. B.Gernes, K. Bourque, H. M. Loree, and J. S. Richardson. A bearingless motor for a left ventricular assist device (LVAD). In *Proceedings of the Seventh International Symposium on Magnetic Bearings*, pages 383–388, ETH Zürich, Switzerland, Aug. 2000.

[111] G. Schweitzer, H. Bleuler, and A. Traxler. *Active Magnetic Bearings*. vdf Hochschulverlag AG an der ETH Zurich, Switzerland, 1994.

[112] B. Shafai, S. Beale, P. LaRocca, and E. Cusson. Magnetic bearing control systems and adaptive forced balancing. *IEEE Control Systems Magazine*, 14(2):4–13, Apr. 1994.

[113] S. Silber, W. Amrhein, P. Bosch, R. Schöb, and B. Barletta. Design aspects of a bearingless slice motor. In *Proceedings of the Ninth International Symposium on Magnetic Bearings*, Lexington, KY, Aug. 2004.

[114] S. Silber, W. Amrhein, P. Bosch, R. Schoeb, and N. Barletta. Design aspects of bearingless slice motors. *IEEE/ASME Transactions on Mechatronics*, 10(6):611–617, 2005.

[115] H. Sira-Ramírez and M. Fliess. On the output feedback of a synchronous generator. In *Proceedings of the 43rd IEEE Conference on Decision and Control*, pages 4459–4464, Atlantis, Paradise Island, Bahamas, Dec. 2004.

[116] S. Sivrioglu and K. Nonami. Adaptive output backstepping control of a flywheel zero-bias AMB system with parameter uncertainty. In *Proceedings of the 42nd IEEE Conference on Decision and Control*, pages 3942–3947, Maui, HI, Dec. 2003.

[117] S. Sivrioglu, K. Nonami, and M. Saigo. Low power consumption nonlinear control with H_∞ compensator for a zero-bias flywheel AMB system. *Journal of Vibration and Control*, 10(8):1151–1166, 2004.

[118] R. D. Smith and W. F. Weldon. Nonlinear control of a rigid rotor magnetic bearng system: Modeling and simulation with full state feedback. *IEEE Transactions on Magnetics*, 31(2):973–980, Mar. 1995.

[119] L. S. Stephens and D.-G. Kim. Analysis and simulation of a Lorentz-type slotless, self-bearing motor. *Control Engineering Practice*, 10(2002):899–905, Jul. 2002.

[120] L. S. Stephens and D.-G. Kim. Force and torque characteristics for a slotless Lorentz self-bearing servomotor. *IEEE Transactions on Magnetics*, 38(4):1764–1773, Jul. 2002.

[121] L. S. Stephens and D.-G. Kim. Dynamic modeling and validation of a Lorentz, self-bearing motor test rig. *Transactions of the ASME, Journal of Engineering for Gas Turbines and Power*, 125(1):156–166, Jan. 2003.

[122] K. T. Sundset, T. Harris, S. Gibson, C. R. Rose, R. O. Nelson, and R. J. McQueeney. Magnetic bearing control system for use in phase control of high-speed neutron choppers. In *Proceedings of the Eight International Symposium on Magnetic Bearings*, Mito, Japan, Aug. 2002.

[123] T. Tokumoto, D. Timms, H. Kanebako, K. Matsuda, and Y. Okada. Development of Lorentz force type self-bearing motor. In *Proceedings of the Eight International Symposium on Magnetic Bearings*, pages 59–64, Mito, Japan, Aug. 2002.

[124] D. L. Trumper, W.-J. Kim, and M. E. Williams. Design and analysis framework for linear permanent-magnet machines. *IEEE Transactions on Industry Applications*, 32(2):371–379, Mar./Apr. 1996.

[125] D. L. Trumper, S. M. Olson, and P. K. Subrahmanyan. Linearizing control of magnetic suspension systems. *IEEE Transactions on Control Systems Technology*, 5(4):427–438, Jul. 1997.

[126] P. Tsiotras and B. C. Wilson. Zero and low-bias control designs for active magnetic bearings. *IEEE Transactions on Control Systems Technology*, 11(6):889–904, Nov. 2003.

[127] M. J. Van Nieuwstadt and R. M. Murray. Real-time trajectory generation for differentially flat systems. *International Journal of Robust and Nonlinear Control*, 8(11):995–1020, 1998.

[128] L. K. Vasiljevic and H. K. Khalil. Differentiation with high-gain observers the presence of measurement noise. In *Proceedings of the 45th IEEE Conference on Decision and Control*, pages 4717–4722, San Diego, CA, Dec. 2006.

[129] J. Villagra, B. d'Andrea-Novel, H. Mounier, and M. Pengov. Flatness-based vehicle steering control strategy with SDRE feedback gains tuned via a sensitivity approach. *IEEE Transactions on Control Systems Technology*, 15(3):554–565, May 2007.

[130] J. von Löwis. *Flachheitsbasierte Trajektorienfolgeregelung elektromechanischer Systeme [Flatness-based trajectory tracking control of electromechanical systems].* PhD thesis, TU Dresden, Germany, 2001.

[131] J. von Löwis, J. Rudolph, J. Thiele, and F. Urban. Flatness-based trajectory tracking control of a rotating shaft. In *Proceedings of the Seventh International Symposium on Magnetic Bearings*, pages 299–304, ETH Zürich, Switzerland, Aug. 2000.

[132] H. H. Woodson and J. R. Melcher. *Electromechanical Dynamics Part I: Discrete Systems.* Wiley, New York, 1968.

[133] Y. Wu, P. E. Allaire, G. Tao, and D. Olsen. Modeling, estimation, and control of human circulatory system with a left ventricular assist device. *IEEE Transactions on Control Systems Technology*, 15(4):754–767, Jul. 2007.

[134] S. Zhou and J. Shi. Active balancing and vibration control of rotating machinery: a survey. *The Shock and Vibration Digest*, 33(4):361–371, Dec. 2001.

[135] S. Zhou and J. Shi. Imbalance estimation for speed-varying rigid rotors using time-varying observer. *Transactions of the ASME, Journal of Dynamic Systems, Measurement and Control*, 123:637–644, Dec. 2001.